Order Number 9121906

A study of the magnetosphere-ionosphere coupling processes

Zhu, Lie, Ph.D.

University of Alaska Fairbanks, 1990

U·M·I
300 N. Zeeb Rd.
Ann Arbor, MI 48106

A STUDY OF THE MAGNETOSPHERE-IONOSPHERE

COUPLING PROCESSES

By

Lie Zhu

RECOMMENDED:

Chairman, Advisory Committee

Head, Physics Department

APPROVED:

Dean, College of Natural Sciences

Dean of the Graduate School

9/12/90

Date

A Study of the Magnetosphere-Ionosphere Coupling Processes

A

THESIS

Presented to the Faculty of the University of Alaska

in Partial Fulfillment of the Requirements

for the Degree of

DOCTOR OF PHILOSOPHY

By

Lie Zhu, B.S., M.S.

Fairbanks, Alaska

December 1990

Abstract

Magnetosphere-ionosphere (M-I) coupling processes are studied by using numerical modeling. An M-I coupling model of substorms on the ionospheric recombination time scale (tens of seconds) is developed. The model is two-dimensional (2-D) and time-dependent from which several signatures of substorms can be obtained and understood. The model is then extended to northward interplanetary magnetic field (IMF) conditions to study the effects of the M-I coupling on the high-latitude convection. Based on the model results, a mechanism for the origin of distorted two-cell ionospheric convection is proposed. The ionospheric and ground signatures of multiple field-aligned current sheets originating from dayside flux transfer events have been modeled. The interaction between Alfvén waves and field-aligned potential drops is studied by using a local model.

Table of Contents

List of Figures

Acknowledgments

The completion of the research work containing in this thesis would not have been possible without the steady advice and encouragement of the chairman of my advisory committee, Prof. J. R. Kan. He introduced me to the research of magnetospheric physics and provided a constant guidance while I was struggling in the maze of the thesis project. He always reminded me to pay attention to creativity and originality of research work, and these words will benefit my whole professional life. Not only did he help me in scientific aspects, but also he helped me to cultivate my social and language abilities which are also essential for succeeding in the world of research. He is the person who deserves my deepest appreciation.

Many thanks are extended to the members of my advisory committee, Profs. M. H. Rees, R. W. Smith, B. J. Watkins, and J. G. Hawkins, for their helpful discussions, suggestions and words of encouragement. Special thanks is also given to Prof. S.-I. Akasofu for his support and encouragement on this thesis project.

I also want to thank my fellow graduate students in the Geophysical Institute and many friends, J. Baldridge, F. Cao, J. Chen, D. Ding, Y. Lou, D. Lummerzheim, L. Lyu, M. Mandt, C. Price, and M. Yamauchi, for their help in countless discussions and presentation rehearsals, and for their help directly or indirectly related with the completion of the thesis. I would like to thank R. P. Million and C. M. Rohwer for assisting me in solving computer and numerical problems.

I am extremely grateful to my wife, Yuqi Zhao, for her encouragement, help and understanding during my graduate studies.

The study was financially supported by NSF grant ATM-85-21194 and by Air Force Geophysics Laboratory under contract F 19628-88-K-0008.

Chapter 1. Introduction

Particles and fields originating from the Sun can gain entry into the terrestrial magnetosphere and deposit their energy in the ionosphere and atmosphere. This solar-terrestrial chain starts from the solar atmosphere, goes through the solar wind and magnetosphere, finally ends at the ionosphere and atmosphere. The final link of this chain is generically referred to as magnetosphere-ionosphere (M-I) coupling. Because of its key position in the physics of the near-Earth space environment, the M-I coupling has been a major focus of space research.

The M-I coupling encompasses a complicated set of interacting phenomena occurring on vastly different temporal and spatial scales rather than a set of isolated processes. The driving force of the M-I coupling system is the energy and momentum transferred from the interaction between the magnetosphere and the solar wind at the magnetospheric boundary. The energy flow in the M-I system is primarily from the magnetosphere to the ionosphere, and finally dissipates in the ionosphere and atmosphere. However, it is now clear that the ionosphere is not a passive element in this system. The ionospheric dynamics and the spatial distribution of ionospheric conductivity can significantly affect the magnetospheric plasma transport and the configuration of the magnetospheric current system. Furthermore, a substantial portion of the plasma population of the magnetosphere originates in the ionosphere.

Depending on the characteristic scale length, the various coupling processes between the magnetosphere and the ionosphere can be roughly categorized into (1) global scale coupling processes; (2) intermediate scale coupling processes; and

(3) microscopic scale coupling processes. The global scale coupling processes include the global electrical coupling, which simply maps the magnetospheric electric field onto the ionosphere and leads to the $\mathbf{E} \times \mathbf{B}$ convection pattern of the ionospheric plasma; and the global electrodynamic coupling, which consists of large scale Alfvén waves and large scale field-aligned currents. Figure 1.1 [from *Chiu et al.*, 1984] shows average patterns of field-aligned current, ionospheric electric field, horizontal ionospheric current, and $\mathbf{E} \times \mathbf{B}$ drift velocity, which result directly from the global scale coupling processes. Examples of intermediate scale coupling processes are the field-aligned potential drop structure and the westward traveling surge. The microscopic scale coupling processes are mainly the interaction processes between particles and different types of plasma waves, including whistlers, electrostatic ion cyclotron waves, ion acoustic waves, lower hybrid waves, and Langmuir waves. The scope of this thesis will cover only the global scale coupling and the intermediate scale coupling processes in the magnetosphere-ionosphere system and focus on the numerical modeling of the M-I coupling processes.

The basic idea of the magnetosphere-ionosphere coupling model can be traced back to the classic work of *Axford and Hines* [1961]. The concepts and elements of the M-I coupling model were further discussed by *Axford* [1969], *Kennel* [1969], and *Coroniti and Kennel* [1973]. *Vasyliunas* [1970] suggested a computational scheme for treating the M-I coupling in a self-consistent way. This scheme has been developed both in analytic calculations [e.g., *Siscoe*, 1982] and in computer models [e.g., *Spiro et al.*, 1981]. Recent quantitative developments of the M-I coupling model include the Rice convection model on the substorm time scale of 30 minutes [*Harel et al.*, 1981; *Spiro et al.*, 1981; *Wolf et al.*, 1982], the local

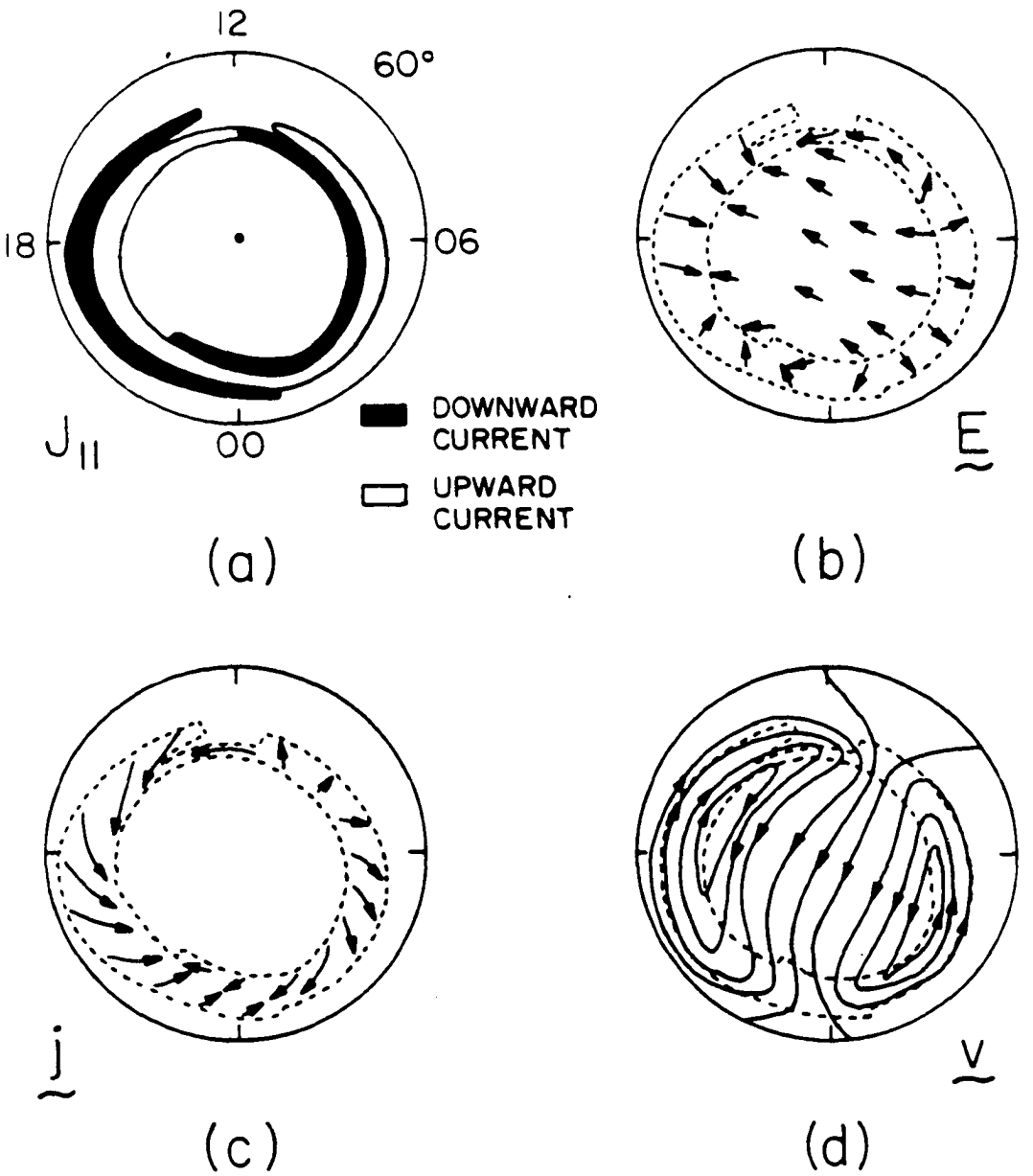

Fig. 1.1. Sketch of the typical patterns of (a) field-aligned current, (b) ionospheric electric field, (c) horizontal ionospheric current, (d) $\mathbf{E} \times \mathbf{B}$ drift velocity [*Chiu et al.*, 1984].

westward traveling surge (WTS) model [*Rothwell et al*, 1984], the MHD simulation model [*Watanabe et al.*, 1986], and the transient response model on the Alfvén wave traveling time scale of a few minutes [*Kan and Sun*, 1985; *Kan et al.*, 1988].

Due to the complexity of the magnetosphere-ionosphere system, each proposed model can only emphasize certain aspects of the M-I coupling system and display part of the global features of the M-I coupling processes. The Rice convection model [*Spiro et al.*, 1981] simulates the M-I coupling in the inner-magnetosphere/ionosphere system ($L < 10$). The ring current and the region 2 current are satisfactorily reproduced in the model, but the model region 1 current varies greatly from the observations. The local westward traveling surge model [*Rothwell et al.*, 1984] studies the propagation features of the WTS in a local frame. The active role of the ionospheric conductance in the M-I coupling receives certain attention in the model. Due to an oversimplified treatment of the current closure at the boundaries, the resulting features of the motion of the WTS in the model are not consistent with observations. The MHD simulation model [*Watanabe et al.*, 1986] is a 3-D model with a pseudo-dimension along magnetic field lines. One-fluid MHD equations are used to model the magnetosphere while a current density continuity equation is used for the ionosphere. Since the ionospheric density is constant in time, there is no actual involvement of the ionospheric dynamics in the model. The features of the region 1 current can be seen in the model results, but the features of the region 2 current are totally lost. The transient response model on the Alfvén wave traveling time scale [*Kan and Sun*, 1985; *Kan et al.*, 1988] can display somewhat more of the observed features of the M-I coupling processes. The transient period is characterized by the successive bouncing of an Alfvén

wave between the magnetosphere and the ionosphere. Alfvén waves are responsible for transmitting information about the enhanced magnetospheric convection to the ionosphere and for sending the ionospheric feedback to the magnetosphere during the transient period when the ionospheric convection, the field-aligned current, and the ionospheric conductance are increasing with time. A number of the observed features of the M-I coupling processes are displayed in the model, which include the distribution of both region 1 and region 2 currents with the correct sense, the enhanced westward and eastward electrojets, the intensified upward field-aligned current band at the poleward edge of the diffuse aurora, and a sudden break-up of the discrete aurora.

The M-I coupling system is like a big puzzle, which can only be built up one piece at a time in a self-consistent way. The strategy guiding the research in this thesis is as follows. First of all, we develop a preliminary global coupling model which should be as simple as possible, but which contains the most basic physical processes. Then we choose an additional important physical process for the M-I coupling and study it in a local frame. After the physics of that specific process is understood in a local sense, the process is built into the global model to see the role of the new process in the whole coupled system and to study the interactions between the specific process and the original basic model. Such a procedure continues until a clear understanding of the role played by every important physical process in the M-I coupling system is achieved. It is believed that this strategy is a practical way to help us to solve the big puzzle of the M-I coupling system. The objective of this thesis is to gain a better understanding of the M-I coupling processes through numerical modeling. The guideline of the thesis can be

summarized as follows. In the coupled M-I system, the ionosphere plays the role of an active key element. The ionospheric dynamics can significantly affect the dynamics in the magnetosphere. Many high-latitude phenomena, including substorm, can only be understood through the M-I coupling processes. The key links between the ionosphere and the magnetosphere are field-aligned current and its carrier Alfvén waves which are initiated by the change of the magnetospheric convection. Under such a guideline, several important results were obtained. First, highly localized discrete auroral structures aligning along the poleward boundary of the diffuse aurora are found to be produced by the positive feedback interactions between the field-aligned currents and the nonuniform and anisotropic ionospheric conductance associated with local recombination time scales. Secondly, four-cell convection patterns imposed on the magnetosphere by the solar wind during a northward IMF can be distorted into wrapped two-cell convection patterns which are similar to the empirical two-cell convection patterns deduced by *Heppner and Maynard* [1987]. The convection distortions are caused by the anisotropic reflections of Alfvén waves due to anisotropic and nonuniform ionospheric conductance. These results have improved our understanding of the coupled M-I system and the high-latitude phenomena.

In chapter 2, a global M-I coupling model of substorms on the ionospheric recombination time scale is presented, which characterizes our modeling of the M-I coupling under the southward interplanetary magnetic field (IMF) conditions. In contrast to most other substorm models, we try to understand the substorm phenomena in terms of the M-I coupling processes. The model is essentially a 2-D time-dependent global model in which the ionospheric recombination time

scale is included and many global signatures of substorms can be displayed and reasonably explained.

In chapter 3, the M-I coupling model presented in chapter 2 is extended to the northward IMF conditions to study the effects of the M-I coupling on the high-latitude convection. Based on the model results, a mechanism for the origination of the distorted two-cell ionospheric convection is proposed, and the associated global features are discussed in the chapter.

The role of dayside dynamics in the global M-I coupling has not been well explored. One of the possible dynamic processes for transferring the energy and momentum of the solar wind to the magnetosphere through the dayside magnetopause is flux transfer events (FTEs). In chapter 4, the ionospheric and ground signatures of the multiple field-aligned current sheets originating from dayside FTEs are modeled in a local frame. The ground features of various FTE theories are also compared and discussed in the chapter.

One of the most important physical processes in the M-I coupling system is the interaction between Alfvén waves and field-aligned potential drops. In chapter 5, the interactions between Alfvén waves and a localized double layer potential drop are studied in isolation (e.g. with the exclusion of the magnetosphere and the ionosphere). The work can be used as a basis for building the interaction between Alfvén waves and field-aligned potential drop into a global M-I coupling model.

Finally, chapter 6 summarizes the major results and conclusions of the thesis, and discusses the possible further work in terms of the developed M-I coupling model.

Chapter 2. Global Magnetosphere-Ionosphere Coupling Model of Substorms

2.1. Introduction

The magnetospheric substorm is a transient process in which a significant amount of energy derived from the solar wind-magnetosphere interaction is deposited in the auroral ionosphere and in the magnetosphere. A substorm is a global manifestation of the solar wind-magnetosphere-ionosphere interaction, which could not be seen as a phenomenon exclusively due to the plasma-sheet dynamics, or exclusively due to the ionospheric dynamics.

Akasofu [1964] first proposed the concept of auroral substorms, and subsequently [*Akasofu*, 1968] assembled the high-latitude processes associated with the auroral substorms in a framework that was called magnetospheric substorm. Since that time a vast amount of research has been carried out that has greatly enhanced our understanding of the substorm phenomena. An operational definition of a magnetospheric substorm was derived by a working group [*Rostoker et al.*, 1980], which is as follows: the term magnetospheric substorm described an interval of increased energy dissipation confined, for the most part, to the region of the auroral oval. The onset of this process is signaled by explosive increases in auroral luminosity in the midnight sector, and the entire process encompasses an interval during which the strength of the auroral electrojet current increases from and returns back to the background level. During this interval there may

be a sequence of intensifications of the westward electrojet, each associated with a Pi 2 micropulsation burst and a westward traveling surge. As the substorm develops, the region of discrete aurora in the midnight sector expands poleward and westward (the poleward bulge). Eventually, the region of disturbed aurora reaches a maximum latitude and begins to recover toward its presubstorm location. The interval of time between the first Pi 2 burst and the time the aurora reaches a maximum latitude has been called the expansion phase. The interval during which the aurora in the midnight sector returns to lower latitudes is called the recovery phase.

The object of substorm studies is a huge assembly consisting of many coupled physical processes occurring in the magnetosphere and the ionosphere. The purpose of substorm studies is not only to understand each physical process in the substorm, but also to understand the role played by an individual process in the whole substorm system and to examine the interrelationships between different physical processes. The substorm is indeed a set of global phenomena caused by the coupling of a number of coupled nonlinear physical processes.

This chapter presents a global magnetosphere-ionosphere coupling model of substorms on the ionospheric recombinaton time scale. The purpose of the model is to understand the substorm phenomena in terms of the coupling processes between the magnetosphere and the ionosphere, which is different from most other global substorm models. The major contribution of the model is the inclusion of the finite ionospheric recombination time scale in the M-I coupling processes. Many global signatures of substorms can be displayed and reasonably explained by the modeling results. It is believed that the present substorm model contains

a certain portion of the essential links in the substorm system and can be used as a basis for more comprehensive global substorm models.

The chapter is organized in the following way. Section 2.2 describes the global magnetospheric and ionospheric signatures of substorms, and introduces the progress in global modeling of substorms. Section 2.3 introduces the basic idea and the main results of the M-I coupling model of substorms on the Alfvén wave traveling time scale. Section 2.4 presents an M-I coupling model of substorms on the ionospheric recombination time scale, including the mathematical and numerical formulations of the model, the global features of substorms displayed by the numerical results, and the corresponding physical explanations of those features. Section 2.5 summarizes the major results of the model, and discusses the applicability and the further improvement of the model.

2.2. Global Signatures and Modeling of Substorms

Morphological features of substorms have been studied extensively by observations. The global ionospheric and magnetospheric signatures of substorms summarized by *Kan* [1989] are listed below.

(1) Substorms develop most typically when the equatorward auroral arc (near the poleward edge of the diffuse aurora) suddenly brightens and subsequently undergoes both poleward and westward expansion [*Akasofu*, 1964].

(2) Bright auroral arcs are at locations where intense ($> 10^{-6}\mathrm{A/m^2}$) upward field-aligned currents flow [*Kamide and Rostoker*, 1977].

(3) The auroral oval expands during the growth phase of a substorm. The

polar cap potential drop increases as the interplanetary magnetic field turns southward [*Reiff and Luhmann*, 1986; *Doyle and Burke*, 1983].

(4) The region 1 and 2 field-aligned currents intensify asymmetrically [*Iijima and Potemra*, 1976], leading to intense upward field-aligned currents near the westward head of the substorm surge [*Baumjohann*, 1988; *Opgenoorth et al.*, 1983] located near the Harang discontinuity [*Heppner*, 1977].

(5) Auroral electrojet currents intensify as measured by the AE index which correlates with the polar cap potential drop [*Ahn et al.*, 1984].

(6) A tail-like magnetic field configuration develops at 6.6 R_E prior to the substorm onset. Thinning of the plasma sheet starts at $\sim$ 15 R_E about 30 minutes prior to the onset of substorms [*Hones*, 1984].

(7) Closure of the intense substorm field-aligned currents in the plasma sheet results in the substorm current wedge [*Atkinson*, 1967; *McPherron et al.*, 1973], although the cause which leads to the formation of the substorm current wedge is still subject to different interpretations.

(8) A near-Earth X-line may form earthward of the pre-existing X-line in the distant tail, leading to the formation of a plasmoid streaming tailward [e.g., *Hones*, 1979]. The radial distance of the near-Earth X-line is probably greater than 20 R_E.

(9) Plasma injections occur near 6.6 R_E [*Deforest and McIlwain*, 1971; *McIlwain*, 1974] when the tail field become more dipolar [*Cummings and Coleman*, 1968].

(10) High-speed bursty earthward plasma flow occurs in the inner central plasma sheet inside 20 R_E [*Baumjohann et al.*, 1989]. High-speed plasma flow

occurs in the plasma sheet boundary layer (PSBL) when the plasma sheet recovers during the recovery phase of substorms [*Lui et al.*, 1977]. Ion temperature increases strongly with AE in the central plasma sheet, while it increases slowly with AE in the PSBL under disturbed conditions [*Huang and Frank*, 1986; *Baumjohann et al.*, 1989].

The global modeling of substorms has a much shorter history than the observations of substorms. In terms of mechanisms, the substorm models can be categorized as: (1) near-Earth X-line models [*McPherron et al.*, 1973; *Schindler*, 1974; *Nishida and Hones*, 1974; *Hones*, 1980; *Baker et al.*, 1987; *Lyons and Nishida*, 1988; *Baumjohann*, 1988], (2) low-latitude boundary layer models [*Rostoker*, 1987; *Rostoker and Eastman*, 1987], (3) magnetosphere-ionosphere coupling models [*Spiro et al.*, 1981; *Rothwell et al.*, 1986; *Kan and Sun*, 1985; *Kan et al.*, 1988], and (4) thermal catastrophe models [*Smith et al.*, 1986; *Goertz and Smith*, 1989].

The main idea of the near-Earth X-line model is to show that substorm onset is a result of the formation of a new X-line in the near-Earth central plasma sheet. The typical configuration change in the central plasma sheet associated with the formation of a new X-line is schematically shown by Figure 2.1 [from *Hones*, 1980]. Panel 1 depicts the quiescent plasma sheet as it may exist some considerable time before a substorm. Panel 2 depicts conditions at the instant of onset of the substorm's expansive phase. Panels 3, 4, and 5 depict a continuation of the process of severing plasma sheet field lines at N' as lines labeled 3, 4, and 5 successively reach N'. The Earth-free tailward-flowing portion of the plasma sheet, threaded with closed magnetic loops, is called a "plasmoid". In panels

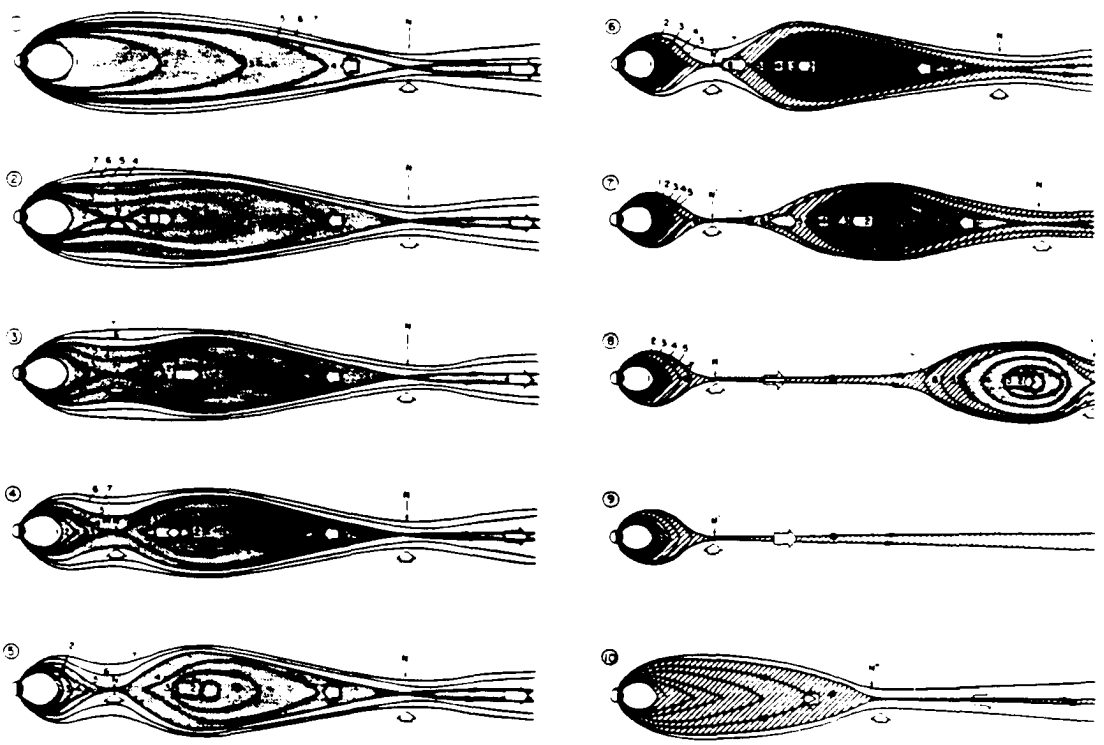

Fig. 2.1. Typical configuration change in the central plasma sheet associated with the formation of a new X-line [*Hones*, 1980]. White arrows depict plasma flow.

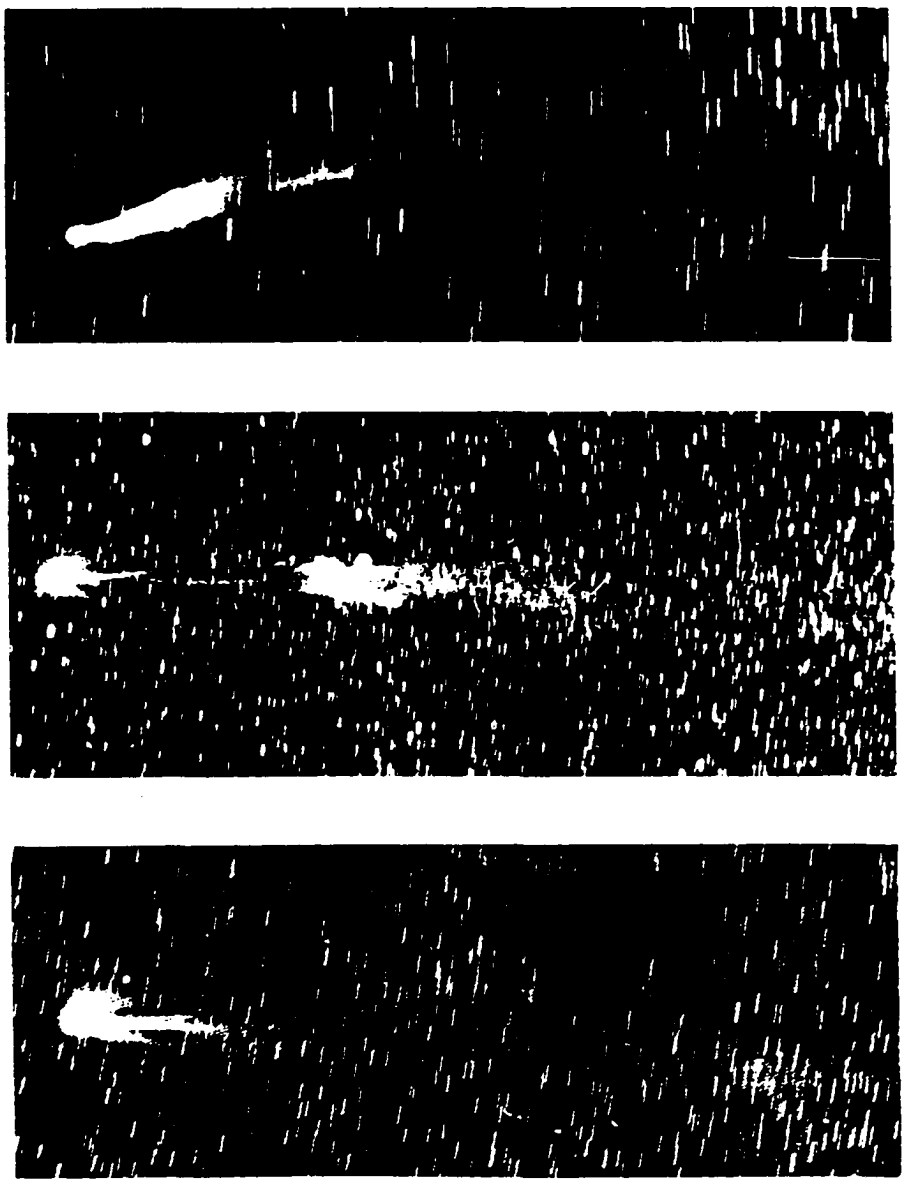

Fig. 2.2. Comet Morehouse (1908 III) on September 30, October 1, and October 2, top to bottom, respectively. This sequence shows the disconnection and drifting away of the plasma tail [*Baker et al.*, 1984].

6-9, lobe field lines are reconnecting at N', and in the meantime the plasmoid is moving tailward rapidly. Panel 10 depicts the recovery of the plasma sheet. The above sequence is similar to the rapid loss of plasma at comet tails, which is shown by the subsequent photographs in Figure 2.2 [from *Baker et al.*, 1984]. There are two important issues associated with the near-Earth X-line model that are presently unresolved [*Kan*, 1989]. First, where does the near-Earth X-line form in the plasma sheet, and second, what is the timing of the near-Earth X-line formation in the substorm time frame? In addition, the near-Earth X-line model does not refer much to the ionospheric signatures of substorms.

The low-latitude boundary layer model proposes that the substorm onset is caused by the Kelvin-Helmholtz instability in the low-latitude boundary layer from which the substorm current wedge originates. Figure 2.3 [from *Rostoker*, 1987] shows a schematic diagram of the mapping between the magnetosphere and the ionosphere, which helps to understand the mechanism of the low-latitude boundary layer model. According to the model, a substorm starts with an increase in energy input from the solar wind, normally achieved through a more southward orientation of the IMF. This leads to an increased circulation in the closed CPS (central plasma sheet)/LLBL (low-latitude boundary layer) cells, either through an enhanced merging process in the magnetospheric tail or through an enhanced viscous interaction. The increased momentum shear between the CPS and the LLBL then leads to the growth of the Kelvin-Helmholtz instability which drives the enhanced Birkland current system and triggers the onset of a substorm. Currently, the low-latitude boundary layer model of substorms is still in its early qualitative stage, and has not yet included the ionospheric effects, which probably stabilize

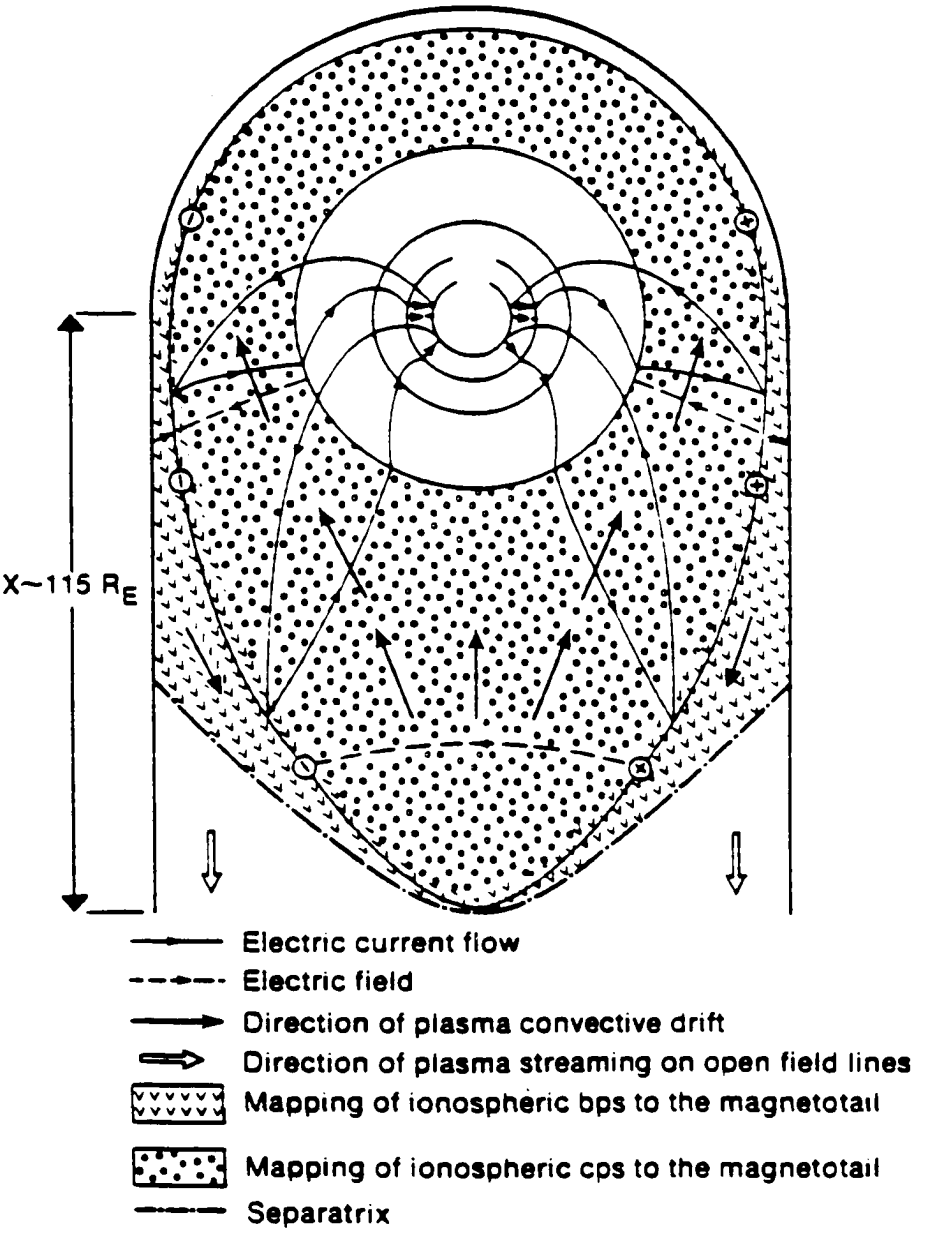

Fig. 2.3. Mapping of plasma convection flows on the geomagnetic equatorial plane/plane of the neutral sheet [*Rostoker*, 1987].

the Kelvin-Helmholtz instability.

The magnetosphere-ionosphere coupling model pays more attention to the ionospheric side of the substorm system, and treats the ionosphere as a dynamic region, rather than as a passive load as in the other two models. Recent quantitative developments of the M-I coupling model of the substorms include the Rice convection model on the substorm time scale of 30 minutes [*Spiro et al.*, 1981], the local westward-traveling surge model [*Rothwell et al.*, 1984], and the transient response model on the Alfvén wave traveling time scale of a few minutes [*Kan et al.*, 1988]. A more detailed description of the main physical ideas of the M-I coupling model of substorms is given in section 2.3, in which the M-I coupling model of substorms on the Alfvén wave traveling time scale is specifically introduced.

The basic idea of the thermal catastrophe model of substorms is that the substorm onset is caused by ion heating in the plasma sheet boundary layer due to the resonant absorption of Alfvén waves generated by the solar wind-magnetosphere interaction. The resonant absorption process requires a nonuniform density, which exists at the boundary between the tail lobe and the plasma sheet boundary layer. The surface Alfvén waves in the model are assumed to be excited by the Kelvin-Helmhotz instability at the magnetopause.

2.3. Brief Review of the M-I Coupling Model of Substorm on the Alfvén Wave Traveling Time Scale

2.3.1. Framework of the Model

The framework of the M-I coupling model of substorms on the Alfvén wave traveling time scale proposed by *Kan et al.* [1988] is briefly introduced, laying the basis for the substorm model to be presented in section 2.4. The model proposes that the substorm onset is directly caused by the ionospheric response to an enhanced magnetospheric convection following a southward turning of the IMF. First of all, the model defines a transient stage of an enhanced M-I coupling, which is the period between the southward turning of a steady IMF and the maximum epoch of the resulting substorm. The transient stage of an enhanced M-I coupling consists of the presubstorm phase and the substorm expansive phase. The substorm onset occurs at the end of the presubstorm phase, and the maximum epoch of a substorm occurs at the end of the expansive phase. The presubstorm phase lasts for 30 to 40 min. It consists of two steps: the first step takes only a few minutes, during which the magnetospheric convection is enhanced after a southward turning of the IMF. The second step takes approximately 30 min before the brightening of an auroral arc, marking the onset of a substorm.

Figure 2.4 is a block diagram summarizing the cause and effect of the proposed substorm onset process. Following a southward turning of the IMF, the reconnection on the dayside magnetopause will be enhanced. The enhanced reconnection launches enhanced antisunward convection of open field lines out from

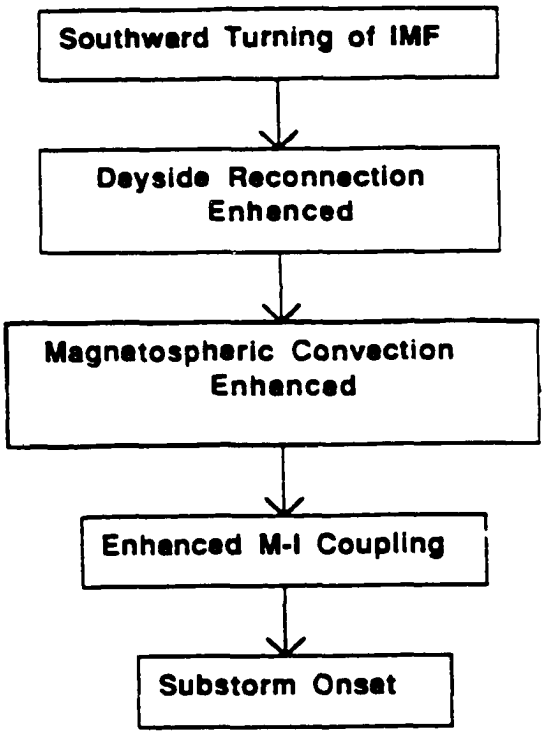

Fig. 2.4. A block diagram summarizing the cause and effect of the proposed substorm onset process [*Kan et al.*, 1988].

the reconnection sites and, at the same time, launches enhanced sunward convection of closed field lines into the reconnection sites. The time scale for establishing an enhanced magnetospheric convection from dayside to nightside is only a few minutes after a southward turning of the IMF.

An enhanced magnetospheric convection then forces the ionospheric convection to speed up. About 30 min are needed for the ionosphere to respond fully

to the enhanced magnetospheric convection. Alfvén waves, which are initiated by the enhanced magnetospheric convection, are responsible for transmitting the information of the enhanced magnetospheric convection to the ionosphere during the transient period when the ionospheric convection, the field-aligned currents, and the ionospheric conductance are increasing with time. Eventually, at the end of the transient period, the enhanced M-I coupling leads to the onset of the substorm, which is characterized by a sudden brightening of the auroral arc near the poleward edge of the diffuse aurora in the evening-midnight sector.

Note that the starting point of the proposed substorm theory is the enhanced global magnetospheric convection, which can occur following a southward turning of the IMF with or without the formation of the near-Earth X-line in the plasma sheet. Therefore, the proposed substorm mechanism neither depends on nor excludes the formation of a near-Earth X-line.

2.3.2. Main Results

The magnetosphere is assumed uniform and the ionosphere is allowed to be highly nonuniform and fully anisotropic in the M-I coupling model of substorms [*Kan et al.*, 1988]. A reflection coefficient is used to describe the reflection of the outward traveling Alfvén waves at magnetospheric boundaries.

Figure 2.5 shows an example of how an enhanced magnetospheric convection can lead to the onset and the expansive phase of a substorm. Figure 2.5a shows the input magnetospheric convection which is turned on at t=0. Figures 2.5b–2.5f show the asymptotic steady state of the M-I coupling which is reached after 10

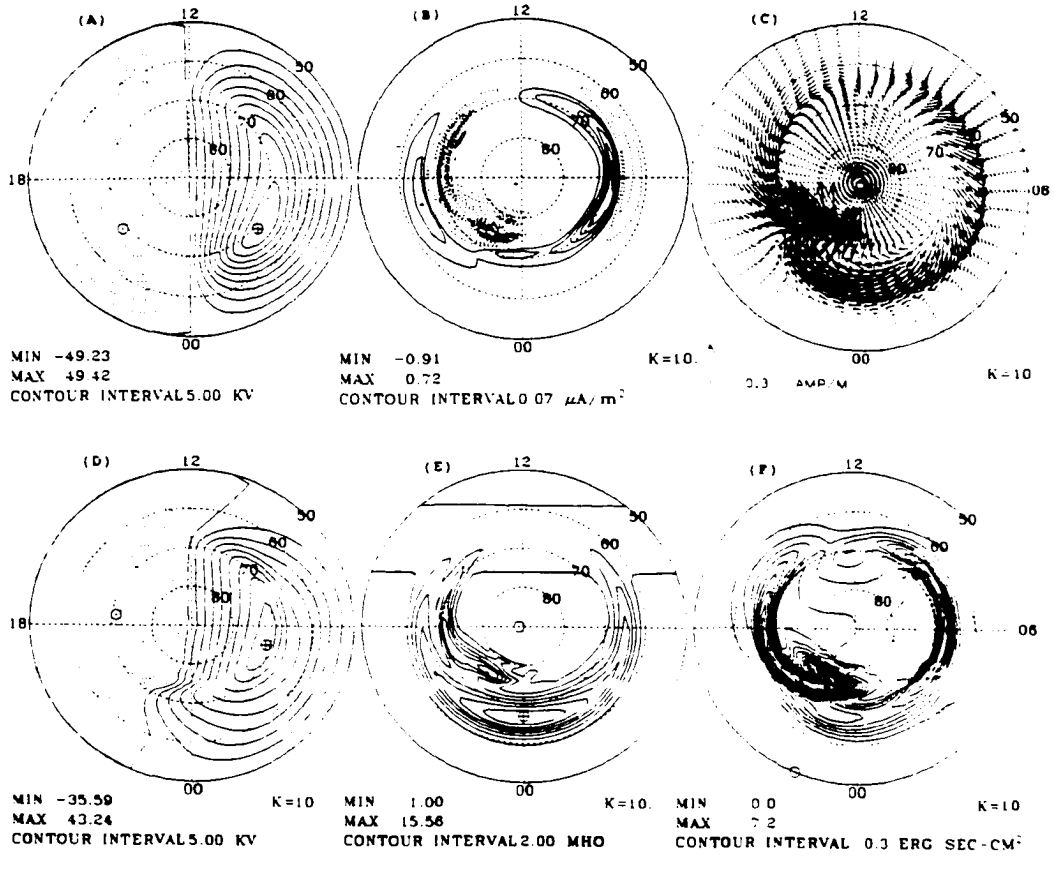

Fig. 2.5. The radial dimension measures the latitude and the azimuthal dimension measures the magnetic local time. (A) Enhanced magnetospheric convection pattern projected on the ionosphere. (B) Field-aligned currents. Dashed contours are constant current density contours of upward currents, solid contours are for downward currents. (C) Ionospheric current vector (including both the Pedersen and the Hall currents). (D) Convection pattern distorted by the nonuniform ionospheric conductance. (E) Hall conductance enhanced by the discrete auroral precipitation. (F) Joule dissipation (all from *Kan et al.*, 1988).

bounces (K=10) of the Alfvén waves launched by the enhanced magnetospheric convection. Each bounce takes 3 to 4 minutes. The asymptotic state should correspond to the maximum epoch of a substorm. Figure 2.5b shows the distribution of the region 1 and 2 field-aligned currents. The maximum upward field-aligned current is located around 22 MLT and accompanied by an intense downward current on the equatorward side. It is important to note that the maximum upward current occurs where the divergence of the Pederson current and the divergence of the Hall current reinforce each other. Figure 2.5c shows the auroral electrojets. Figure 2.5d shows the distorted convection pattern and the formation of the Harang discontinuity [*Heppner*, 1977]. Figure 2.5e shows the distribution of the Hall conductance enhanced by the discrete auroral precipitation. Figure 2.5f shows the distribution of the Joule dissipation rate.

Figure 2.6 shows the relationship between the divergence of the Pederson current and the divergence of the Hall current for the case considered in Figure 2.5. The dots indicate the locations where the divergence of the Hall current is antiparallel to the divergence of the Pederson current; the net field-aligned currents at those locations are due to the divergence of the Pederson current. At the locations of circles, the divergence of the Hall current is parallel to the divergence of the Pederson current; the net field-aligned currents at those locations are no longer due to the divergence of the Pederson current alone. From these results, *Kan et al.* [1988] concluded that the field-aligned currents outside the westward traveling surge region are predominantly due to the divergence of the Pederson current. Inside the westward traveling surge and the substorm onset auroral arc, the divergence of the Hall current contributes significantly to the upward field-

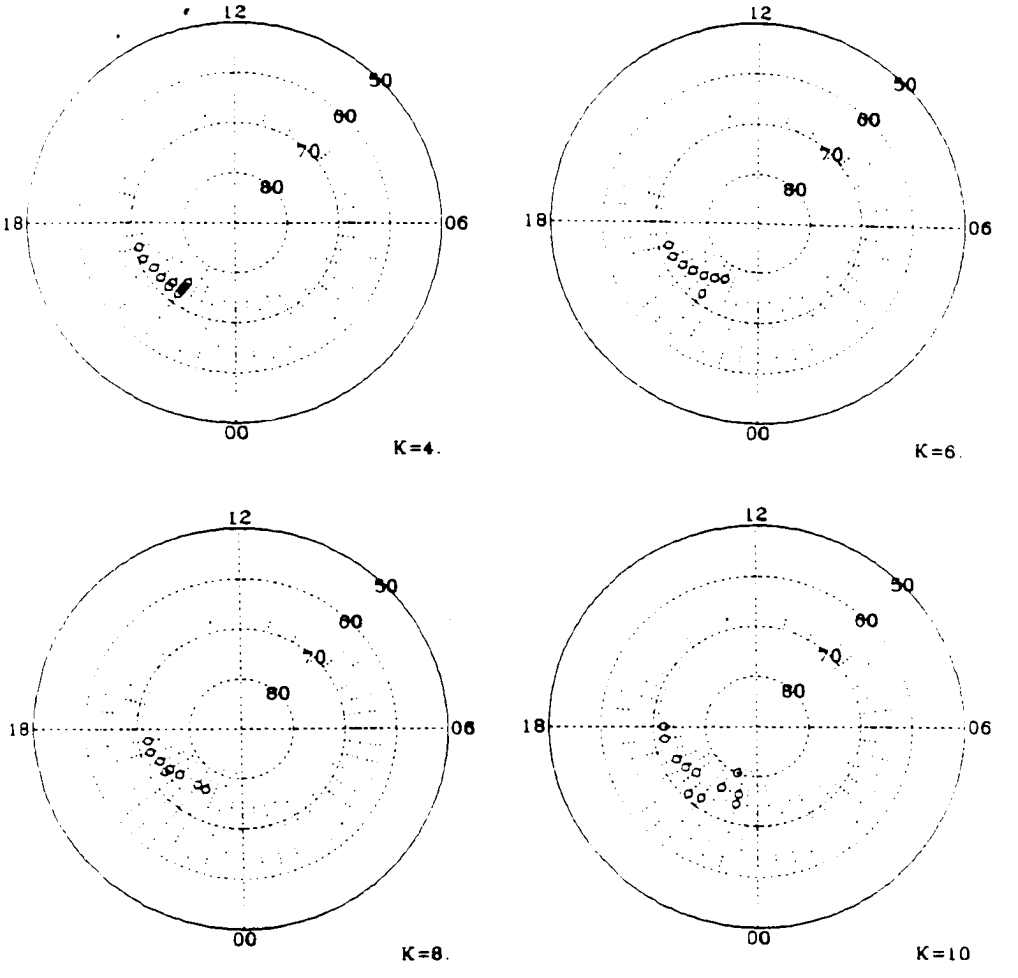

Fig. 2.6. Relationship between the divergence of the Hall current and the divergence of the Pedersen current for the case shown in Fig. 2.5. The dots indicate the locations where the divergence of the Hall current is antiparallel to the divergence of the Pedersen current. At the locations of circles, the divergence of the Hall current is parallel to the divergence of the Pedersen current [*Kan et al.*, 1988].

aligned current.

The main results of the M-I coupling model of substorms on the Alfvén wave traveling time scale [*Kan et al.*, 1988] can be summarized as follows: (1) The model shows quantitatively that an enhanced magnetospheric convection with or without the formation of the near-Earth X-line in the plasma sheet can lead to auroral substorm onset about 40 min after a southward turning of the IMF. (2) Two necessary conditions for the substorm onset are found from the modeling results: (a) the polar cap potential must exceed a certain value (about 70 kV in the model), depending on the convection pattern and the distribution of the ionospheric conductance; and (b) the convection reversal region must overlap with the poleward gradient of the diffuse auroral conductance in the midnight sector ionosphere. The matching ensures that the divergence of the Pederson current is coincident with the divergence of the Hall current to maximize the upward field-aligned current near the poleward boundary of the diffuse aurora in the midnight sector for substorm onset.

2.4. An M-I Coupling Model of Substorms on the Ionospheric Recombination Time Scale

2.4.1. Basic Model

When the interplanetary magnetic field turns southward, the reconnection on the dayside magnetopause will be enhanced. The enhanced dayside reconnection can lead to enhanced magnetospheric convection, launching Alfvén waves toward

the ionosphere. The propagating Alfvén waves can carry both field-aligned currents and transverse polarization currents. The relationship between the wave electric field and the currents can be derived from MHD equations.

The ideal MHD equations are

$$\begin{aligned}
&\rho\frac{\partial \mathbf{V}}{\partial t} + \rho(\mathbf{V}\cdot\nabla)\mathbf{V} = \mathbf{J}\times\mathbf{B} - \nabla P \\
&\frac{\partial \rho}{\partial t} + \nabla\cdot(\rho\mathbf{V}) = 0 \\
&\mathbf{E} + \mathbf{V}\times\mathbf{B} = 0 \\
&P\rho^{-\gamma} = \text{constant} \\
&\nabla\times\mathbf{E} = -\frac{\partial \mathbf{B}}{\partial t} \\
&\nabla\times\mathbf{B} = \mu_o\mathbf{J}
\end{aligned} \tag{2.1}$$

where ρ is the mass density, $\mathbf{V}$ is the fluid velocity, $\mathbf{J}$ is the current density, B is the magnetic field, P is the pressure, $\mathbf{E}$ is the electric field, γ is the ratio of specific heats, and μ_o is the free space permeability. The relationship between the fluid velocity $\mathbf{V}$ and the perturbed magnetic field $\mathbf{b}$ of a nonlinear Alfvén wave is

$$\mathbf{V} = \pm\frac{\mathbf{b}}{(\mu_o\rho_o)^{1/2}} \tag{2.2}$$

where ρ_o is the background mass density, the plus (minus) sign is for the propagation antiparallel (parallel) to background magnetic field $\mathbf{B}_o$. The corresponding phase velocities are $\mathbf{V}_\phi = \mp\mathbf{V}_A$, where $\mathbf{V}_A = \mathbf{B}_o/(\mu_o\rho_o)^{1/2}$. Since $\mathbf{b}$ and $\mathbf{V}$ are coplanar, the electric field of an Alfvén wave is

$$\mathbf{E} = -\mathbf{V}\times\mathbf{B}_o \tag{2.3}$$

Inserting equations (2.2) and (2.3) into the last equation in (2.1), we obtain the relationship between the electric field of an Alfvén wave and the currents carried

by the Alfvén wave,

$$\mathbf{J}_A = \pm\Sigma_A[-\mathbf{b}_o(\nabla\cdot\mathbf{E}) + (\mathbf{b}_o\cdot\nabla)\mathbf{E}] \tag{2.4}$$

where $\mathbf{b}_o = \mathbf{B}_o/B_o$, $\Sigma_A = (\mu_o V_A)^{-1}$ is the characteristic conductance of the plasma carrying the Alfvén wave. The first term in equation (2.4) is the field-aligned current carried by Alfvén wave, and the second term is the polarization current flowing across field lines along the wavefront.

When the Alfvén wave launched by the enhancement of the magnetospheric convection arrives at the ionosphere, the wave field can be partially reflected from the ionosphere because of finite ionospheric conductance. From equation (2.4), the field-aligned currents carried by the incident and the reflected Alfvén waves can be written as

$$\mathbf{J}_{\parallel A} = \mathbf{b}_o\Sigma_A\nabla\cdot(\mathbf{E}^i - \mathbf{E}^r) \tag{2.5}$$

where $\mathbf{E}^i$ and $\mathbf{E}^r$ are the incident and the reflected Alfvén wave fields respectively. The current continuity in the ionosphere can be expressed as

$$\mathbf{J}_{\parallel i} = \nabla\cdot(\Sigma_P\mathbf{E}_i + \Sigma_H\mathbf{b}_o\times\mathbf{E}_i) \tag{2.6}$$

and

$$\mathbf{E}_i = \mathbf{E}^i + \mathbf{E}^r + \mathbf{E}_{iP}$$

where $\mathbf{E}_i$ is the total ionospheric electric field at that moment, and $\mathbf{E}_{iP}$ is the ionospheric electric field which excludes the incident and the reflected wave fields, and Σ_P and Σ_H are the ionospheric Pedersen conductance and Hall conductance respectively.

By matching, the field-aligned currents carried by the incident and the reflected waves and the field-aligned currents which exists in front of the wave-front of the Alfvén waves ($J_{\|D}$) with the divergence of the ionospheric currents, we obtain a time-dependent equation which describes the reflection of an Alfvén wave from the ionosphere.

$$\Sigma_A \nabla \cdot \left[\mathbf{E}^i(t) - \mathbf{E}^r(t)\right] + J_{\|D}(t) = \nabla \cdot \left[\Sigma_P(t)\mathbf{E}_i(t) + \Sigma_H(t)\mathbf{b}_o \times \mathbf{E}_i(t)\right] \tag{2.7}$$

and

$$\mathbf{E}_i(t) = \mathbf{E}^i(t) + \mathbf{E}^r(t) + \mathbf{E}_{iP}(t)$$

Inspection of equation (2.7) shows that the reflected Alfvén waves $\mathbf{E}^r$, more precisely referred to as upward propagating Alfvén waves, not only originate from the reflection of the downward propagating Alfvén waves, but can also originate from a temporal change of the ionospheric conductance. The latter can be seen clearly if the components of $J_{\|D}$ are written down explicitly, i.e.

$$J_{\|D}(t) = \nabla \cdot \left[\Sigma_P(t - \Delta t)\mathbf{E}_{iP}(t) + \Sigma_H(t - \Delta t)\mathbf{b}_o \times \mathbf{E}_{iP}(t)\right] \tag{2.8}$$

The mechanism of a temporal change of the ionospheric conductance producing an upward propagating Alfvén wave can be elucidated as follows. The temporal change of the ionospheric conductance can lead to an electric field perturbation superposed on the background ionospheric electric field. The perturbed electric field then leads to the perturbation of magnetic field lines, producing the upward propagating Alfvén waves. The significance of the upward propagating Alfvén waves due to the temporal change of the ionospheric conductance in equation

(2.7) is that it shows that the ionosphere plays an active role in the M-I coupling system. The upward propagating Alfvén waves continuously send updated information about changes in the ionosphere to the magnetosphere, thereby modifying the dynamics in the magnetosphere and keeping the interaction between the magnetosphere and the ionosphere internally consistent. This is an important feature of this new model which is different from most of the other M-I coupling models.

On the magnetospheric side, a reflection coefficient is used to describe the reflection of the outward traveling Alfvén waves at the magnetospheric boundaries, which can be expressed as

$$R_m = -1 \quad \text{on open field lines} \tag{2.9a}$$

$$-1 < R_m < 1 \quad \text{on closed field lines} \tag{2.9b}$$

It may be noted that $R_m = -1$ corresponds to an idealized constant voltage source while $R_m = 1$ corresponds to a constant current source. The value of R_m on closed field lines can be expected to increase from slightly greater than -1 towards $+1$ as one moves from the distant tail or the low-latitude boundary layer toward the inner edge of the plasma sheet.

The physics governing the reflection of outward traveling Alfvén waves at the magnetospheric boundary has been briefly summarized by *Kan et al.* [1988]. On open field lines the solar wind inertia is sufficiently large so that the $\mathbf{E} \times \mathbf{B}$ flow of the solar wind is more or less unaffected by the loading of the incident Alfvén wave at the magnetopause. This means that the electric field on open field lines at the magnetopause is kept more or less constant by the solar wind, which can be translated into the condition that the electric field of the reflected wave must

more or less cancel the incident wave field, i.e., the reflection coefficient on open field lines at magnetopause is given by $R_m = -1$. The situation on closed field lines is quite different. The inertia of the $\mathbf{E} \times \mathbf{B}$ convection in the plasma sheet is very limited, therefore the incident Alfvén wave can be expected to modify the electric field in the plasma sheet on closed field lines. If the inertia in the plasma sheet is sufficiently small, an Alfvén wave incident on the plasma sheet will be transmitted almost without reflection. Consider a pair of identical but oppositely propagating Alfvén waves incident on the plasma sheet simultaneously. They will be fully transmitted in this case. By regarding the transmitted waves as if they were reflected, we find the equivalent reflection coefficient $R_m = +1$. On the other hand, if the inertia in the plasma sheet is sufficiently large, such as in the low-latitude boundary layer, R_m may be somewhat less than +1, but larger than −1. For a more detailed discussion of the physics governing the reflection coefficient R_m, the reader is referred to *Kan and Sun* [1985].

The finite ionospheric recombination time scale is included by using a time-dependent continuity equation to describe the ionization in the ionosphere. This is different from *Kan et al.'s* [1988] model in which the ionospheric recombination time is set to zero, since they are mainly concerned with the auroral development on the Alfvén wave traveling time scale which is much larger than the ionospheric recombination time. Under the assumption that the discrete aurora is produced exclusively by the upward field-aligned currents which are carried by energetic precipitating electrons, the electron continuity equation in the ionosphere can be written as

$$\frac{\partial N}{\partial t} + \nabla \cdot (N\mathbf{V}) = \frac{Q|J_\parallel|}{e} + \frac{|J_\parallel|}{eH} + S_o - \beta N^2 \qquad (2.10)$$

where N is the electron number density in the ionosphere, Q is the ionization coefficient which is defined later in this section, H is the effective height of the conducting ionosphere, β is the recombination coefficient, and S_o is the source term during quiet time which can be determined by the quiet-time convection and the quiet-time ionospheric conductance, i.e.,

$$S_o = \nabla \cdot (N_o \mathbf{V}_o) + \beta N_o^2 \tag{2.11}$$

Note that as long as the auroral electron energy is 1 keV or more, the magnitude of the first term on the right side of equation (2.10) is at least one order greater than that of the second term on the right side. Therefore, the second term on the right side of equation (2.10) will be dropped for simplicity.

From the definition of the Hall conductivity, the height-integrated Hall conductivity in the E layer of the ionosphere can be approximated by

$$\Sigma_H = \frac{NeH}{B_o} \tag{2.12}$$

By using equation (2.12), and assuming that the ratio $R = \Sigma_H/\Sigma_P$ is independent of the energy of the precipitating electrons, equation (2.10) can be rewritten as

$$\begin{aligned} \frac{\partial \Sigma_H}{\partial t} &= \frac{QH}{B_o} \nabla \cdot (\Sigma_P \mathbf{E}_i + \Sigma_H \mathbf{b}_o \times \mathbf{E}_i) \\ &\quad + \frac{eH}{B_o} S_o - \frac{\beta B_o}{eH} \Sigma_H^2 + \nabla \Sigma_H \cdot \frac{\mathbf{b}_o \times \mathbf{E}_i}{B_o} \end{aligned} \tag{2.13}$$

The ionization coefficient Q is defined as

$$\begin{aligned} &Q = 0 \qquad J_\parallel \text{ downward or } |J_\parallel| < J_o \\ &Q = Q_o \qquad J_\parallel \text{ upward and } \nabla \cdot \mathbf{E}_i \geq 0 \text{ and } |J_\parallel| > J_o \\ &Q = \gamma'(|J_\parallel| - J_o) \qquad J_\parallel \text{ upward and } \nabla \cdot \mathbf{E}_i < 0 \text{ and } J_o < |J_\parallel| < J_c \\ &Q = \gamma'(J_c - J_o) \qquad J_\parallel \text{ upward and } \nabla \cdot \mathbf{E}_i < 0 \text{ and } |J_\parallel| \geq J_c \end{aligned} \tag{2.14}$$

where Q_o is a constant which depends on the energy of diffuse auroral precipitation, γ' is a parameter which depends on the $J_{||} - \phi_{||}$ relationship [*Fridman and Lemaire*, 1980], J_o is the thermal electron current in the loss cone, and J_c is an equivalent saturation current for the upper limit of available electron energy flux. The ionization coefficient Q is defined as the average number of ions produced by an incident electron per meter, which is proportional to the energy of the precipitating electrons. Since the enhancement of ionospheric conductance during a substorm is assumed to be caused exclusively by the precipitating electrons, Q should be zero in the regions where the field-aligned currents are downward. In the regions where $J_{||}$ is upward, and $\nabla \cdot \mathbf{E}_i > 0$, the potential drop structures do not exist along magnetic field lines [*Lyons*, 1980]. Therefore the precipitation in these regions is the diffuse auroral precipitation, and we assume Q to be constant, depending on the electron energy in the plasma sheet. In the region of discrete auroral precipitation, *Knight* [1973] and *Fridman and Lemaire* [1980] showed that the upward field-aligned current density $J_{||}$ depends linearly on the potential drop $\phi_{||}$ along magnetic field lines. Therefore the energy of precipitating electrons can be assumed to be linearly proportional to the upward field-aligned current density in the discrete aurora regions as shown in equation (2.14).

The equations (2.7), (2.9), (2.11), (2.13), and (2.14) form the basic equations of the present M-I coupling model of substorms. The temporal evolution of Alfvén waves, of the field-aligned currents, of the ionospheric convection, and of the ionospheric conductance can be obtained by solving these equations numerically.

2.4.2. Numerical Scheme

The basic assumptions of the model can be summarized as follows. (1) The ionospheric conductance is assumed to be height-integrated, nonuniform, and anisotropic (including both Hall and Pedersen conductances). (2) The magnetospheric plasma is assumed to be uniform, and the Alfvén wave traveling time between the magnetospheric source regions and the ionosphere is assumed to be constant. (3) The magnetospheric dynamics are treated by the reflection coefficient R_m which is a function of latitude and longitude, depending on whether the field lines are open or closed. (4) The discrete aurora is mainly produced by the upward field-aligned current carried by energetic precipitating electrons. (5) The ratio between the Hall conductance and the Pedersen conductance is assumed independent of the energy of the precipitating electrons.

The ionosphere in our simulation is modeled by computational grids on a polar coordinate system or, equivalently, the cylindrical coordinate system sliced at $z = 0$. The radial dimension measures the latitude from 50° to 90°. The azimuthal dimension measures the longitude. The grid size is 1° in latitude and 7.5° in longitude. The third dimension along the magnetic field lines is a pseudo-dimension which merely serves to provide the time scale. The magnetosphere is also simplified as a plane which is the source region of the initial enhanced magnetospheric convection and is used only for treating the reflection of the Alfvén waves on the magnetospheric side.

The numerical procedure of the model is as follows. (1) First, the initial enhanced magnetospheric convection, the quiet-time ionospheric convection, the

ionospheric conductance prior to the substorm and the reflection coefficient are given. (2) The ionization source term in the ionosphere during quiet-time is determined by equation (2.11). (3) The upward propagating wave field from the ionosphere is determined by the numerical solution of equation (2.7). (4) Next we calculate the total ionospheric electric field, the field-aligned current and the horizontal ionospheric current at that moment. (5) The reflected wave from the magnetosphere can be determined by equation (2.9), which contains a time delay depending on the Alfvén wave traveling time. The reflected wave from the magnetosphere will be used as the incident wave for the ionosphere in the late time steps. (6) At the same time, the conductance in the ionosphere grows because of the enhanced upward field-aligned currents carried by the previous Alfvén waves. The time scale of this ionization process is on the order of the recombination time scale. The enhancement of the ionospheric conductance is determined by equation (2.13). (7) Next we go back to equation (2.7) to determine the upward propagating Alfvén waves of the next time step. Note that even though there is no incident wave from the magnetosphere, the upward propagating waves are not necessarily equal to zero, because the ionospheric conductance keeps changing and so can launch upward propagating Alfvén waves. Because of finite conductance in the ionosphere, the Alfvén waves which bounce between the ionosphere and the magnetosphere eventually will be damped and the whole M-I system will approach a steady state. Repetition of steps (3) to (7) gives the time variation of the ionospheric convection, the field-aligned current, the ionospheric conductance, the integrated horizontal current, and the Joule heating rate.

Figure 2.7 shows the input parameters of the present model. Figure 2.7*a*

shows the input enhanced magnetospheric convection projected on the ionosphere, which is driven by an enhanced reconnection at the dayside magnetopause. Figure 2.7*b* shows the distribution of ionospheric conductance prior to the substorm, consisting of the solar conductance and the diffuse auroral conductance. Figure 2.7*c* shows contours of the magnetospheric reflection coefficient, and Figure 2.7*d* shows the distribution of the magnetospheric reflection coefficient along the noon-midnight meridian. In contrast to the assumption of zero quiet-time convection in the previous M-I coupling model of substorms [*Kan et al.*, 1988], the quiet-time ionospheric convection in the present model is assumed to have the same pattern as the enhanced magnetospheric convection shown in Figure 1*a*, except for a smaller polar cap potential drop (20 kV). Other model parameters are as follows: thermal electron current $J_o = 0.08$ μA m^{-2}, equivalent saturation current $J_c = 0.8$ μA m^{-2}, constant ionization coefficient $Q_o = 7\times10^{-3}$ ions per electron per meter, coefficient $\gamma' = 1\times10^{4}$ (ions m)/(electron A) [*Rees*, 1963; *Fridman and Lemaire*, 1980], and recombination coefficient $\beta = 0.9 \times 10^{-13}$ m^3 s^{-1} [*Walls and Dunn*, 1974]. The ratio between the Hall conductance and the Perderson conductance $R = 1.5$. In reality, the value of R varies with the energy of the precipitating electrons, therefore the adoption of a constant R in the present model is a first approximation and can be removed in futher improvement of the model. The time step is 5 s and the Alfvén wave traveling time between magnetosphere and ionosphere is assumed to be 4 min. We set $t = 0$ when the enhanced convection carried by Alfvén waves first arrives in the ionosphere. The input parameters are kept constant unless otherwise noted.

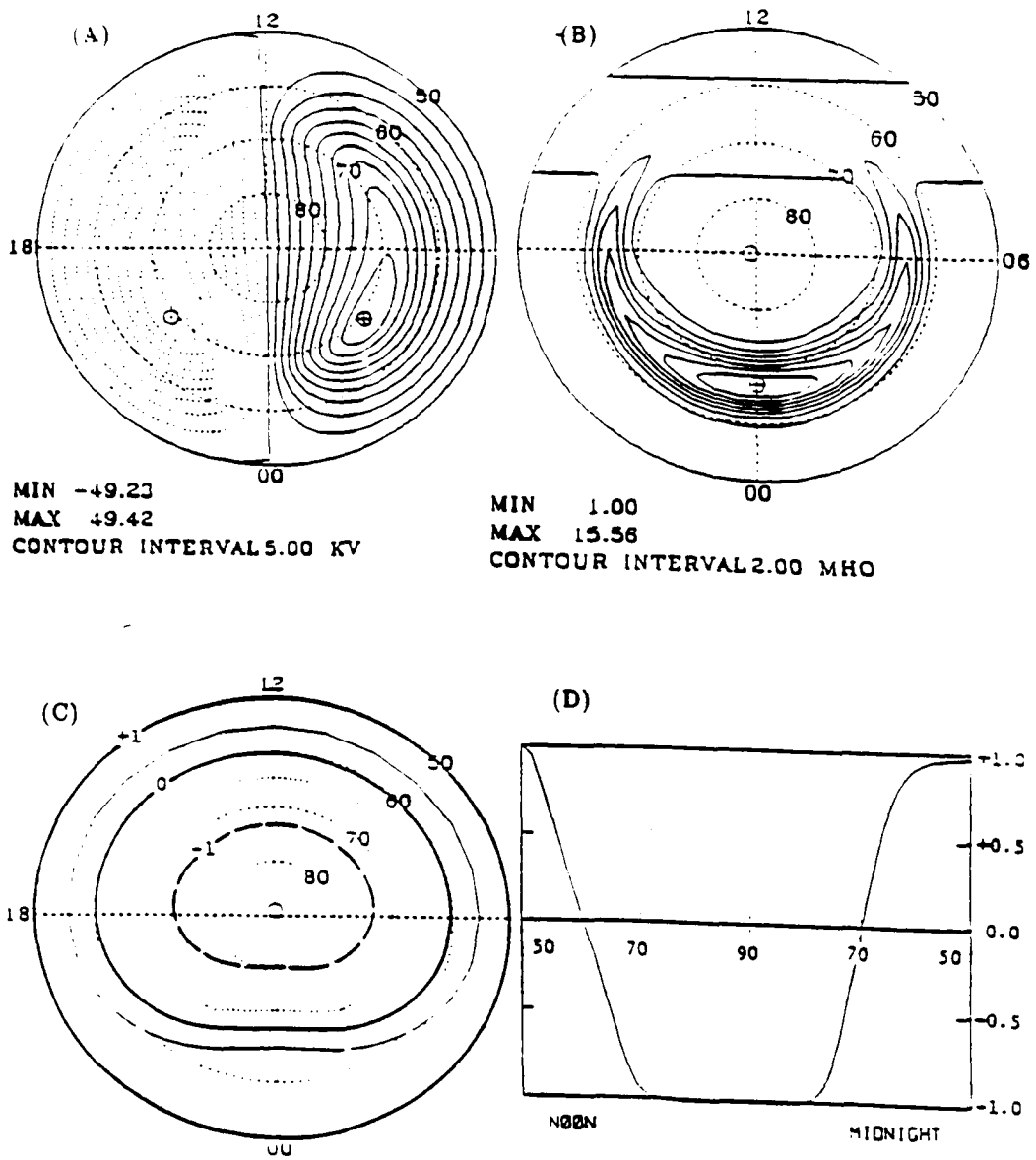

Fig. 2.7. Input parameters for the model. (A) Input enhanced magnetospheric convection. (B) Background ionospheric Hall conductance prior to the enhancement of magnetospheric convection. (C) Contours of magnetospheric reflection coefficient. (D) Distribution of the reflection coefficient along the noon-midnight meridian.

2.4.3. Global Features of Substorms from the Modeling

The global features of substorms resulting from the present M-I coupling model are presented in this section. Figure 2.8 shows the output of the present model at $t = 36$ min. Figure 2.8*a* shows the distorted ionospheric convection pattern. Note the Harang discontinuity [*Heppner*, 1977] which has formed in the evening-midnight sector. Figure 2.8*b* shows the distribution of the ionospheric Hall conductance enhanced by the discrete auroral precipitation. Figure 2.8*c* shows the ionospheric horizontal currents in which the westward electrojet and the eastward electrojet can be easily identified. Figure 2.8*d* shows the distribution of the Joule dissipation rate.

Figure 2.9 shows snapshots of the temporal evolution of the field-aligned currents. The dashed lines represent the upward field-aligned currents, and the solid lines represent downward field-aligned currents. The intense upward field-aligned current is known to cause a potential drop in the kilovolt range along magnetic field lines [*Knight*, 1973; *Lyons et al.*, 1979]. The precipitating electrons are accelerated through the potential drop, and cause the ionization and auroral brightening in the E region of the ionosphere. In this connection, the brightening of the discrete aurora is equivalent to the intensification of upward field-aligned currents when the intensity of the upward field-aligned current exceeds a certain value. In the following, our analysis and discussion will exploit this conceptual equivalence.

The temporal evolution of the discrete aurora shown in Figure 2.9 can be summarized as follows. At $t = 4$ min (i.e., 6 min after the enhanced magnetospheric

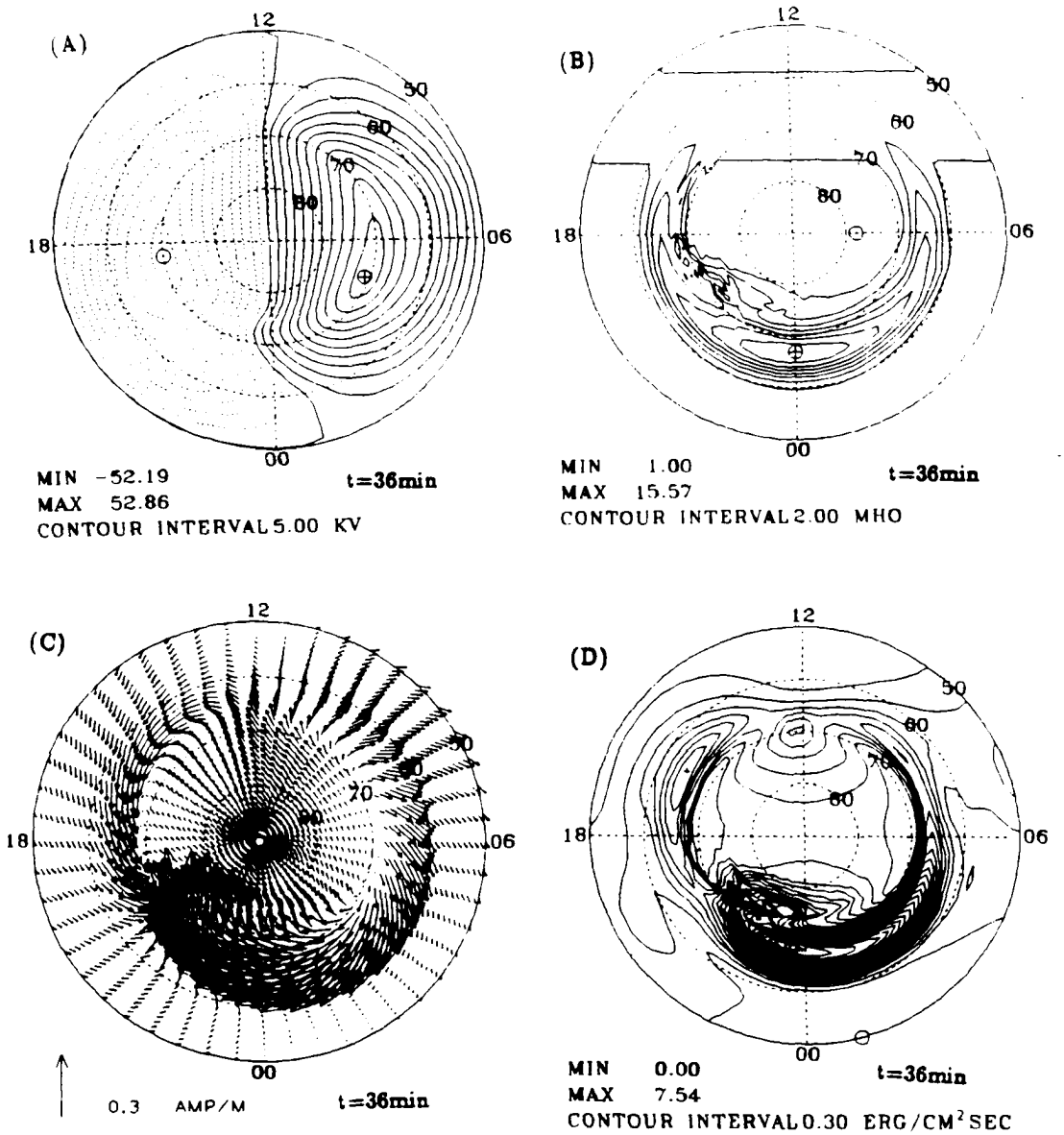

Fig. 2.8. Output of the model at t = 36 min. (A) Ionospheric convection pattern. (B) Distribution of the enhanced ionospheric conductance. (C) Ionospheric horizontal currents. (D) Distribution of the Joule dissipation rate.

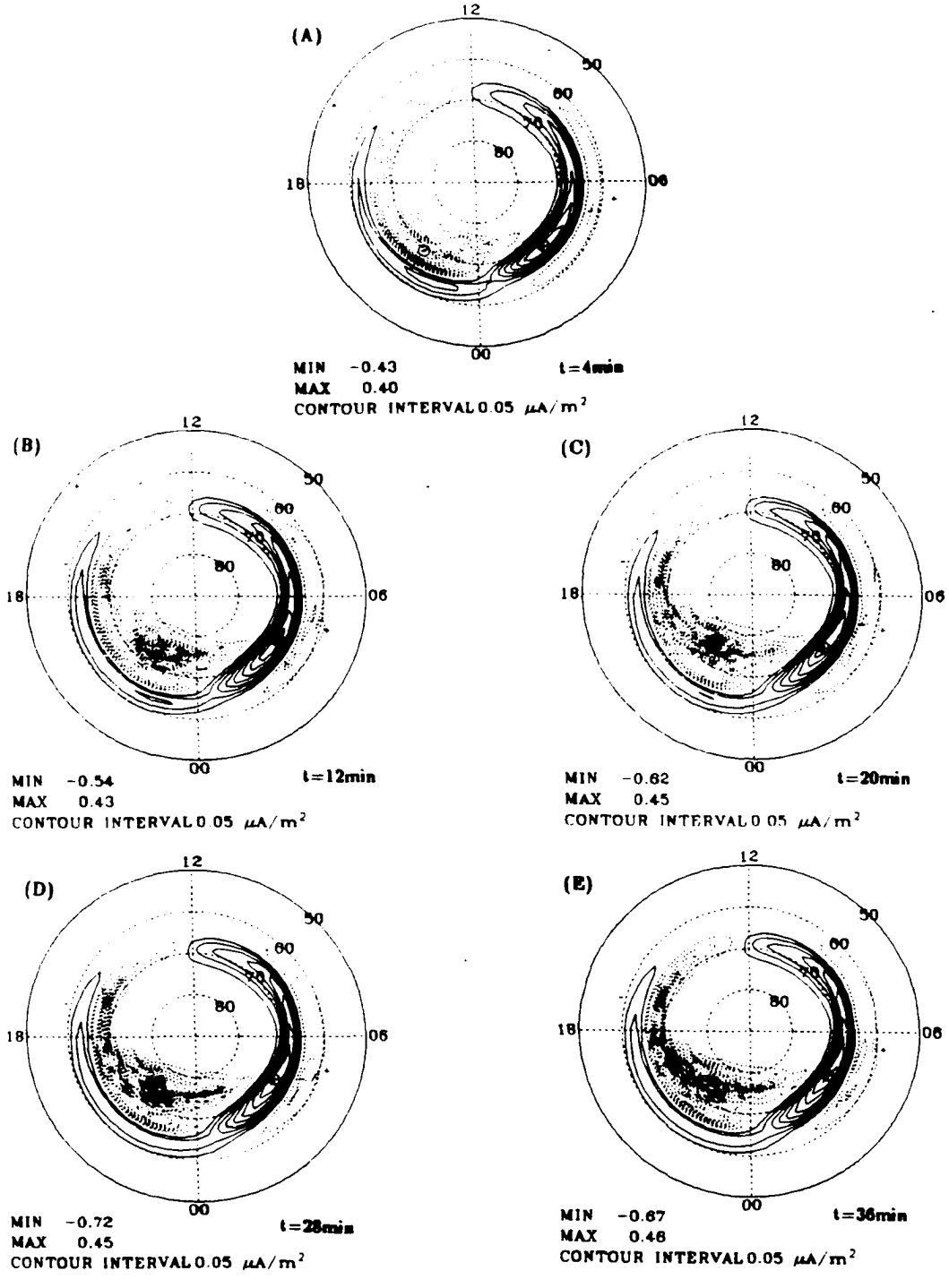

Fig. 2.9. Snapshots of the temporal evolution of the field-aligned currents.

convection is turned on), there is no substantial development of the discrete aurora. However, during the period from 4 to 12 min, there is a noticeable increase in the intensity of the discrete aurora in the evening-midnight sector. Note that at the same time, the region of discrete aurora expands not only poleward and westward, but also eastward. This feature has been observed by the Viking UV imager [*Anger et al.*, 1987; *Shepherd et al.*, 1987] and has aroused strong interest [*Rostoker et al.*, 1987]. During the period from 12 to 20 min, a further intensification of the discrete aurora can be seen, and local structures of the discrete aurora begin to appear. Finally, the substorm onset occurs during the period from 20 to 28 min, which is characterized by a sudden brightening of the discrete aurora near the poleward boundary of the diffuse aurora in the premidnight sector. Note that in Figure 2.9*d*, there is a small scale downward field-aligned current embedded in the intensified large scale upward field-aligned currents. This feature is also found in the previous model [*Kan et al.*, 1988]. An apparent westward motion of the discrete aurora can be seen from Figure 2.9*e* after the onset of the substorm. This kind of westward motion of the intensified discrete aurora can be interpreted as the westward traveling surge. The westward traveling surge moves with an initial velocity around 2 km s^{-1} which is consistent with the observations [*Akasofu*, 1968], and then gradually slows down and becomes dimmer. Following passage of the surge, several localized auroral arcs remain along the auroral oval, and the most active auroral region shifts from premidnight towards the evening sector. Observational results from the DE-1 satellite for the westward traveling surge [*Craven et al.*, 1989] confirm the predicted features of the westward traveling surge in our model. Another feature which we can see from Figure 2.9 is the highly localized

structures of the discrete aurora along the auroral oval in the evening-midnight sector. This feature has been observed in Viking imager data [*Anger et al.*, 1987; *Marklund et al.*, 1987]. Furthermore, it is found that the location of the substorm onset and the transient time prior to the substorm onset in the present model are almost the same as those in the previous M-I coupling model of substorms [*Kan et al.*, 1988]. This indicates that the ionospheric recombination scale does not significantly influence the onset of the substorm, but it does influence the auroral signatures of the substorm as shown in the above.

Figure 2.10 shows the snapshots of the enhancement of the ionospheric conductance. At t = 4min, there is no substantial enhancement of the ionospheric conductance. Later, we can see that the conductance along the poleward boundary of the diffuse aurora in the premidnight sector is gradually enhanced and that many structures develop.

2.4.4. Highly Localized Structures of Discrete Aurora

One of the interesting features in Figure 2.9 is the appearance of the highly localized structures of the discrete aurora. In this section, a physical explanation for this feature is provided, and comparison is made to the results of the M-I coupling model of substorms on the Alfvén wave traveling time scale [*Kan et al.*, 1988].

In the previous substorm model [*Kan et al.*, 1988], the ionization at different locations in the ionosphere is intensified with a single characteristic time scale, i.e., the Alfvén wave traveling time scale. In the present model, since we have included

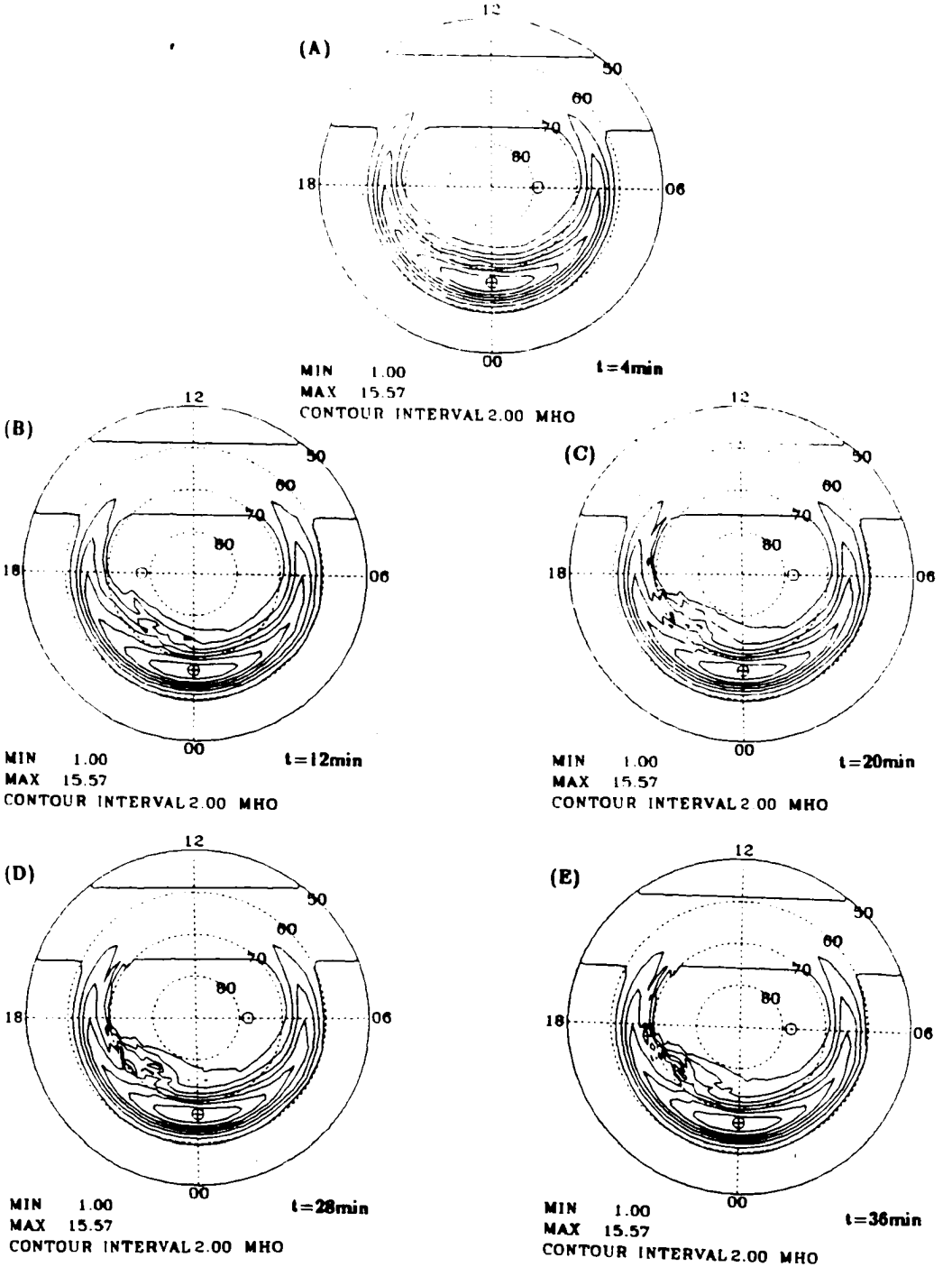

Fig. 2.10. Snapshots of the temporal evolution of the ionospheric Hall conductance.

the ionospheric recombination time scale by using the time-dependent continuity equation, the ionization in the ionosphere is intensified with two characteristic time scales, i.e., the Alfvén wave traveling time scale and the recombination time scale. Note that the latter depends on the fluxes and energies of precipitating electron populations and therefore is related to the intensity of the field-aligned currents. A field-aligned current which is associated with precipitating electrons of higher energy leads to a shorter recombination time. In other words, the ionospheric conductance in a region with a stronger field-aligned current is enhanced more rapidly and becomes saturated in a shorter time compared to the conductance in a region with a weaker field-aligned current. Because the intensity of local field-aligned current changes continuously with time, the local conductance enhancement is not a simple ionization process associated with a steady precipitating electron flux. Before the conductance becomes saturated, which takes 15 to 30 s, the enhancement of the conductance can be accelerated by a newly arrived wave front which increases the total precipitating electron flux. In this way, the total enhancement of the ionospheric conductance associated with a stronger field-aligned current during an Alfvén wave traveling time period should be much greater than that associated with a weaker field-aligned current during the same period, since the slope of the former is always larger than that of the latter. The greatly enhanced conductance then allows more field-aligned current to flow into the ionosphere (such a message is sent to the magnetosphere by the upward propagating Alfvén waves caused by the change of the conductance), leading to a further enhancement of the ionospheric conductance in that region.

Based on the above argument, it is proposed that the highly localized struc-

tures of the discrete aurora are produced by positive feedback interactions between field-aligned currents and the nonuniform, anisotropic ionospheric conductance associated with local recombination time scales. The process can be summarized as follows. The nonuniformity of field-aligned currents leads to different recombination time scales at different locations in the ionosphere. The varying rates of ionization then increase the nonuniformity of the ionospheric conductance, which in turn leads to a further nonuniformity of field-aligned currents. Eventually, this highly nonuniform pattern of field-aligned current leads to the highly localized brightness structures of the discrete aurora.

2.4.5. Motion of the Westward Traveling Surge

Another interesting feature in the model results shown in subsection 2.4.3 is an apparent westward motion of the discrete aurora, which can be interpreted as the westward traveling surge. In this subsection, we propose a mechanism for the motion of the westward traveling surge based on the results of the present model and the previous M-I coupling model [*Kan et al.*, 1988].

One of the necessary conditions for substorm onset shown in the previous substorm model [*Kan et al.*, 1988] is that the convection reversal region must overlap with the conductance gradient at the poleward edge of the diffuse aurora. This matching ensures that the divergence of the Pederson current is coincident with the divergence of the Hall current, in order to maximize the upward field-aligned current. In fact, this physical argument will now be extended to explain the motion of the westward traveling surge. Figure 2.11 is a schematic diagram in

which the dotted area represents the convection reversal region, and the shaded area represents the conductance gradient at the poleward edge of the diffuse aurora. According to the previous argument, the upward field-aligned currents can be intensified in the overlapping area, which in turn leads to the enhancement of the ionospheric conductance. The enhanced conductance in this area expands the conductance gradient boundary westward, poleward, and eastward, as shown by the dashed line labelled A in Figure 2.11. Obviously, on the eastern edge of the expanded conductance region, the overlapping condition is no longer satisfied. Therefore, there will be no further intensification of the upward field-aligned current around that region, and the discrete aurora cannot go further eastward. But on the western edge of the expanded conductance region, the conductance gradient still overlaps with the convection reversal region. Therefore a further intensification of the upward field-aligned current can be expected. The intensified upward field-aligned current leads to a further enhancement of conductance, which in turn will push the conductance gradient boundary further westward as shown by the dashed line labelled B. In this way, the intensified discrete aurora moves westward one step at a time, forming the westward traveling surge. Since the spatial separation between the convection reversal region and the poleward gradient of the diffuse aurora increases and the diffuse auroral conductance becomes weaker as the westward traveling surge is moving toward the evening sector, the surge will slow down and gradually dim.

According to this picture, the appearance of the feature of the westward traveling surge in the present model can be explained as follows. In the previous model, the quiet-time convection is assumed to be zero. The anisotropic reflection

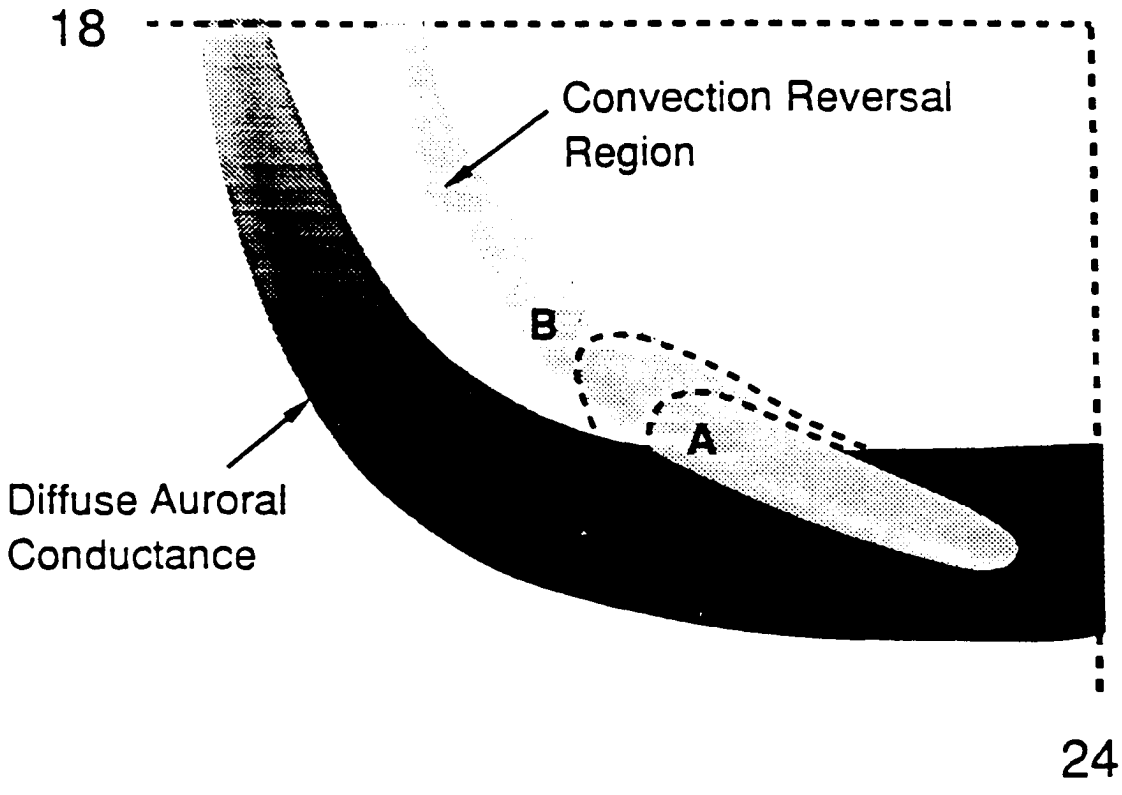

Fig. 2.11. Schematic diagram for explaining the motion of the westward traveling surge. The numbers in the figure represent the magnetic local times.

of Alfvén waves leads to the distortion of the convection pattern in the evening-midnight sector. The distorted convection confines a relatively small region near midnight in which the overlapping condition can be satisfied. For this reason, the previous model showed substorm onset, but did not show an apparent motion of the westward traveling surge. In the present model, the quiet-time convection is not zero, and the quiet-time convection reversal region is coincident with the conductance gradient at the poleward edge of the diffuse aurora. Since the quiet-time convection is not associated with the Alfvén waves launched by the enhanced magnetospheric convection and will not be distorted by the anisotropic reflection of Alfvén waves, the total ionospheric convection in the present model is, therefore, less distorted than that in the previous model [*Kan et al.*, 1988]. The less distorted ionospheric convection leads to an elongated region along the auroral oval in the evening-midnight sector in which the overlapping condition can be satisfied during substorms. A bright discrete aurora can occur and move westward in this elongated region, which forms the westward traveling surge as shown in Figure 2.9. *Kan and Sun* [1985] conducted a numerical modeling of the westward traveling surge based on the M-I coupling process. Because their model used an oversimplified input and excluded the quiet-time convection, discrete aurora is enhanced in the evening sector instead of the midnight sector. The features of the westward traveling surge in their results are not satisfactorily consistent with the observed ones. *Rothwell et al.* [1984] proposed a local westward traveling surge model to study the propagation of the westward traveling surge. By using the assumptions of uniform conductance between poleward and equatorward boundaries and of horizontal currents being closed by field-aligned currents only at the

boundaries, they found that the motion of the westward traveling surge was a constant motion associated with precipitating electrons on the same energy level. This is in contrast to our results in which the motion of the westward traveling surge is a motion with a decreasing speed and is associated with precipitating electrons over a wide energy range.

Figure 2.12 shows the case in which the polar cap potential drop of the quiet-time convection is 6 kV instead of 20 kV (the case shown in Figure 2.8 and Figure 2.9). In this case, the westward traveling surge does not move as far west as in the previous case, and also the speed is slower. This result, combining with the previous argument, suggests that if the reversal region of the quiet-time convection is coincident with the conductance gradient at the poleward edge of the diffuse aurora, a larger quiet-time polar cap potential drop leads to a higher speed of the westward traveling surge.

Based on Viking imager data, *Anger et al.* [1987] found that auroral brightening does not exclusively occur in the premidnight sector and *Rostoker et al.* [1987] found that the discrete aurora also expands eastward. According to the physical argument for the necessary conditions for the substorm onset presented by *Kan et al.* [1988] and the physical explanations of the motion of the westward traveling surge discussed in this subsection, these auroral features can be expected in modeling by shifting the relative positions of the reversal region of the convection pattern and the conductance gradient at the poleward edge of the diffuse aurora.

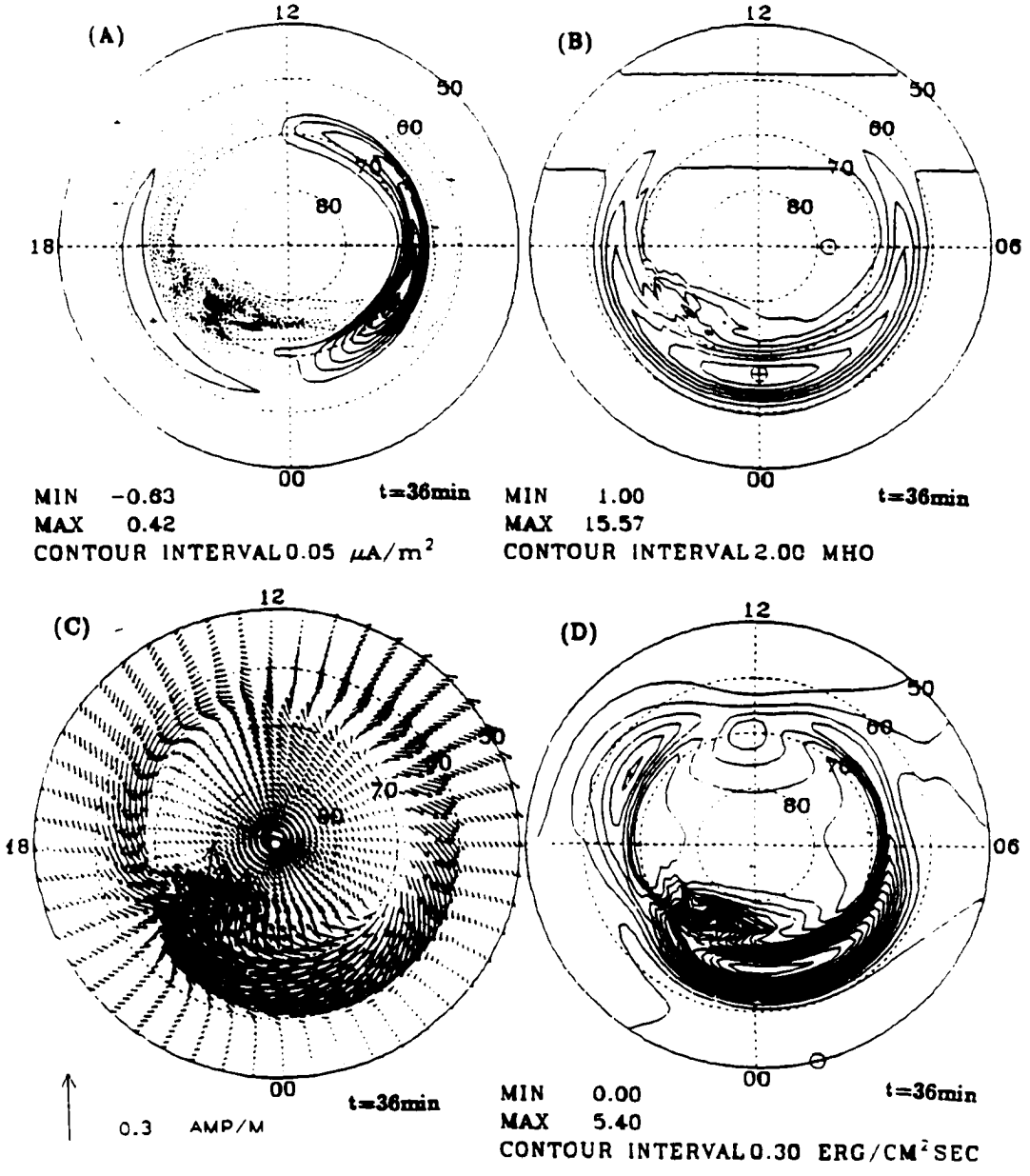

Fig. 2.12. Output of the case in which the polar cap potential drop of the quiet-time convection is 6 kV.

2.4.6. Saturation of the Polar Cap Potential

Weimer et al. [1990] examined the dependence of the auroral electrojet index AE on the large north-south component (B_z) of the IMF, and found that the AE index tends to saturate for large southward IMF, namely, $B_z < -15$ nT. They suggested that the saturation of the AE index is directly related to the saturation of the polar cap potential which originates from the nonlinearity of the magnetosphere-ionosphere coupling processes.

As an integral part of that work [*Weimer et al.*, 1990], the possibility of the saturation of the polar cap potential in a M-I coupling system was examined by using the M-I coupling model of substorms on the Alfvén wave time scale [*Kan et al.*, 1988]. Figure 2.13 shows the results of the M-I coupling model in which the polar cap potential Φ_{pc} is calculated as a function of the input magnetospheric potential Φ_{mR}. The pattern of the magnetospheric potential Φ_{mR} is identical with the initial enhanced magnetospheric convection Φ_o in Section 2.3, and the polar cap potential Φ_{pc} is the asymptotic potential drop across the polar cap after the M-I coupling process approaches a steady state. Each curve is obtained for a given distribution of the diffuse auroral conductance characterized by its peak value Σ_{max}. As the input potential Φ_{mR} increases, the polar cap potential Φ_{pc} tends to saturate. The higher the diffuse auroral conductance (as indicated by its maximum value Σ_{max}), the lower the saturation level of the polar cap potential, as can be seen in Figure 2.13. There is a clear indication of the nonlinear saturation above $\Phi_{mR} = 70$ kV.

These results show that the polar cap potential Φ_{pc}, in response to the input

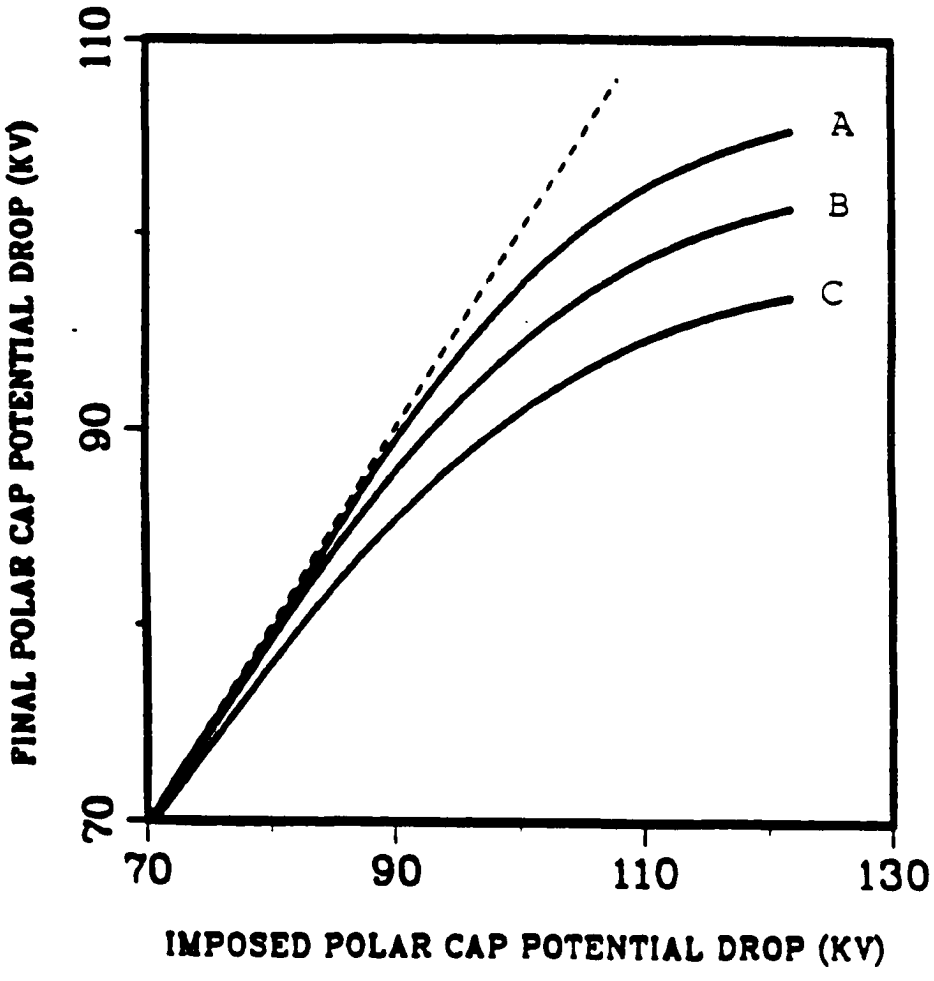

Fig. 2.13. Dependence of the polar cap potential drop Φ_{pc} on the input magnetospheric potential Φ_{mR} imposed by reconnection on the dayside magnetopause. Each curve is for a given Gaussian distribution of the diffuse auroral conductance characterized by its maximum value Σ_{max}. The maximum diffuse auroral conductance for the three curves are (A) Σ_{max} = 7.5 mho, (B) Σ_{max} = 15 mho, (C) Σ_{max} = 22.5 mho.

potential Φ_{mR} imposed by reconnection on the dayside magnetopause, tends to saturate for large values of Φ_{mR}. This is equivalent to overloading a dynamo, causing the dynamo output voltage to fall below its rated value. The overloading in the M-I coupling system can occur if the conductance in the ionosphere increases with increasing input potential.

2.5. Summary

This chapter presents a magnetosphere-ionosphere coupling model of substorms on the ionospheric recombination time scale. This is an extension of the M-I coupling model of substorms on the Alfvén wave traveling time scale [*Kan et al.*, 1988]. The major contribution of the present model is the inclusion of the finite ionospheric recombination time scale in the M-I coupling processes. The global features of magnetospheric substorms obtained from the present model have been shown in the previous sections. The main results are summarized as follows.

1. Highly localized discrete auroral structures align along the poleward boundary of the diffuse aurora in the evening-midnight sector. Such localized features were observed in the Viking imager data. In our model, the localized bright features of discrete aurora are produced by the positive feedback interactions between the field-aligned currents and the nonuniform and anisotropic ionospheric conductance associated with local recombination time scales.

2. The bright discrete auroral arc near midnight suddenly starts moving westward when the auroral brightness increases to a certain level. The moving discrete aurora has an initial velocity of around 2 km s^{-1} but gradually slows

down and dims. This feature can be interpreted as the westward traveling surge. Following passage of the surge, several localized auroral arcs remain along the auroral oval, and the most active auroral region shifts from premidnight toward the evening sector.

3. If the reversal region of the quiet-time convection pattern overlaps with the conductance gradient at the poleward edge of the diffuse aurora, a stronger quiet-time convection leads to a higher speed westward traveling surge during substorms.

4. The physical argument for one of the necessary conditions for substorm onset (i.e., when the convection reversal region overlaps with the conductance gradient at the poleward edge of the diffuse aurora, the upward field-aligned current is maximized) presented by *Kan et al.* [1988] is extended to explain the motion of the westward traveling surge.

5. The polar cap potential Φ_{pc}, in response to the enhanced magnetospheric potential Φ_{mR} imposed by reconnection on the dayside magnetopause, tends to saturate for large values of Φ_{mR}. The higher the diffuse auroral conductance, the lower the saturation level of the polar cap potential.

Chapter 3 Effects of M-I Coupling on the High-Latitude Convections During Northward IMF

3.1. Introduction

In comparison to the physical processes in the magnetosphere-ionosphere system during southward IMF, the situation during northward IMF has received less study and is less well understood. There still exists a great amount of uncertainty on many basic topics associated with northward IMF, and one of them is the high-latitude convection pattern.

Since *Heppner and Maynard* [1987] published the wrapped two-cell convection patterns based on DE-2 electric field data, the four-cell versus wrapped two-cell convection patterns during a northward IMF has become a controversial issue. Reconnection between northward IMF and the open field lines poleward of the cusp region can produce sunward convection between the two convection cells in the polar cap [*Russell*, 1972; *Maezawa*, 1976; *Burch et al.*, 1985; *Kan and Burke*, 1985]. Combining the two cells inside the polar cap due to the reconnection with the two cells outside the polar cap due to the viscous interaction in the low latitude boundary layer, one obtains the four-cell convection pattern imposed on the magnetosphere by the solar wind. Observational support for the four-cell convection pattern is principally the sunward convection across the central polar cap observed by the S3-2, as shown in Figure 3.1 [from *Burke et al*, 1979], and MAGSAT satellites [*Iijima et al*, 1984], and by ground magnetometers [*Maezawa*, 1976]. It has been shown in the previous chapter that the ionosphere can significantly distort

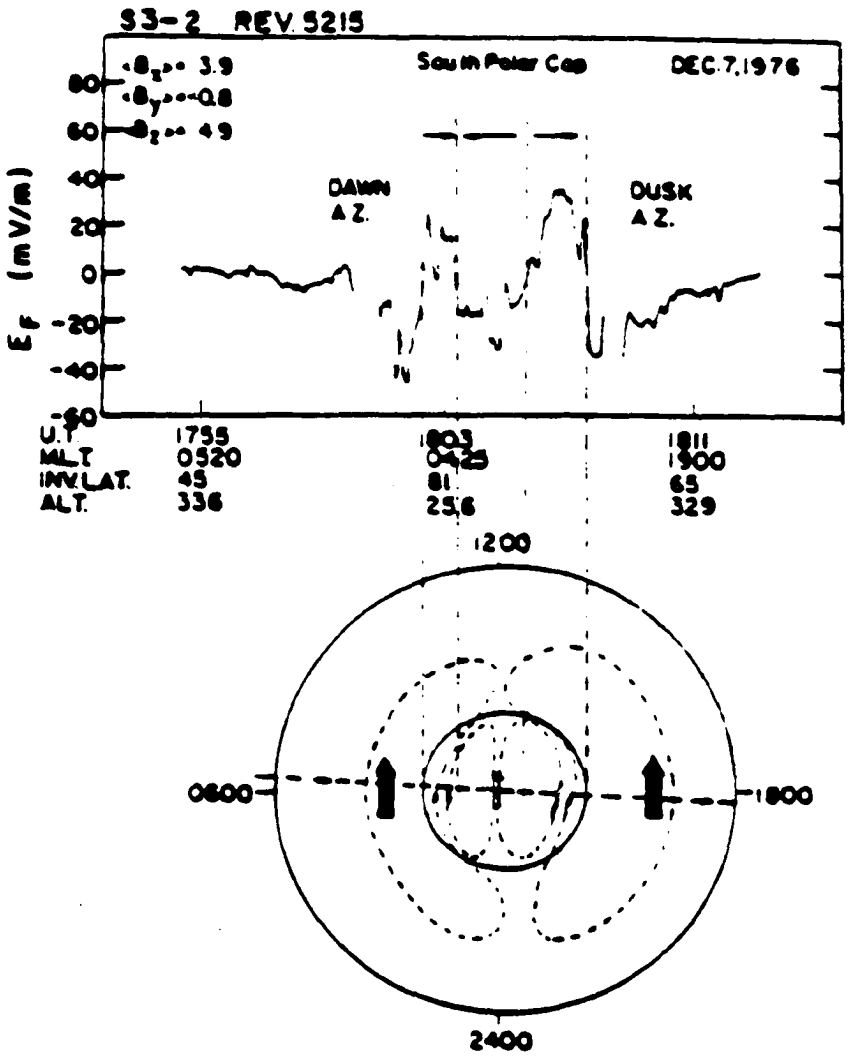

Fig. 3.1. Dawn-dusk component of the convective electric field measured over southern polar cap by S3-2. The bottom picture extrapolates convection to all local time [*Burke et al.*, 1979].

the imposed magnetospheric convection pattern. The resulting convection pattern can be very different from the pattern imposed by the solar wind.

The orbits of the DE-2 satellite cover a much wider range of magnetic local time than either the S3-2 or MAGSAT satellites, and its data are more suited to study the flow pattern in the dayside region. From DE-2 electric field data, strong east-west flows were found in the dayside region, as shown in Figure 3.2 [from *Heppner and Maynard*, 1987], which is in contrast with the observed features in four-cell convection patterns. *Crooker* [1988] made the first attempt to give a theoretical explanation for the empirical two-cell model and found that during periods of northward IMF, magnetic merging between the IMF and the closed field lines on the dayside magnetopause can produce a pair of merging cells confined to the polar cap, which feature is similar to the empirical distorted two-cell patterns. But *Crooker* [1988] also found that while trying to add the convection cells due to the viscous interactions in the low-latitude boundary layer to the model, questions remain about how the viscous cells would separate from the merging cells in the polar cap. *Heelis* (private communication, 1987) pointed out that the wrapped two-cell convection pattern probably comes from the distortion of the four-cell convection pattern.

In this chapter, the M-I coupling model introduced in chapter 2 is extended to northward IMF conditions, and high-latitude convection during northward IMF is studied in terms of the M-I coupling processes. It will be quantitatively shown that although the reconnection processes during northward IMF can impose a four-cell convection pattern on the magnetosphere, the M-I coupling processes can distort the four-cell convection pattern [*Russell*, 1972; *Maezawa*, 1976; *Kan and Burke*,

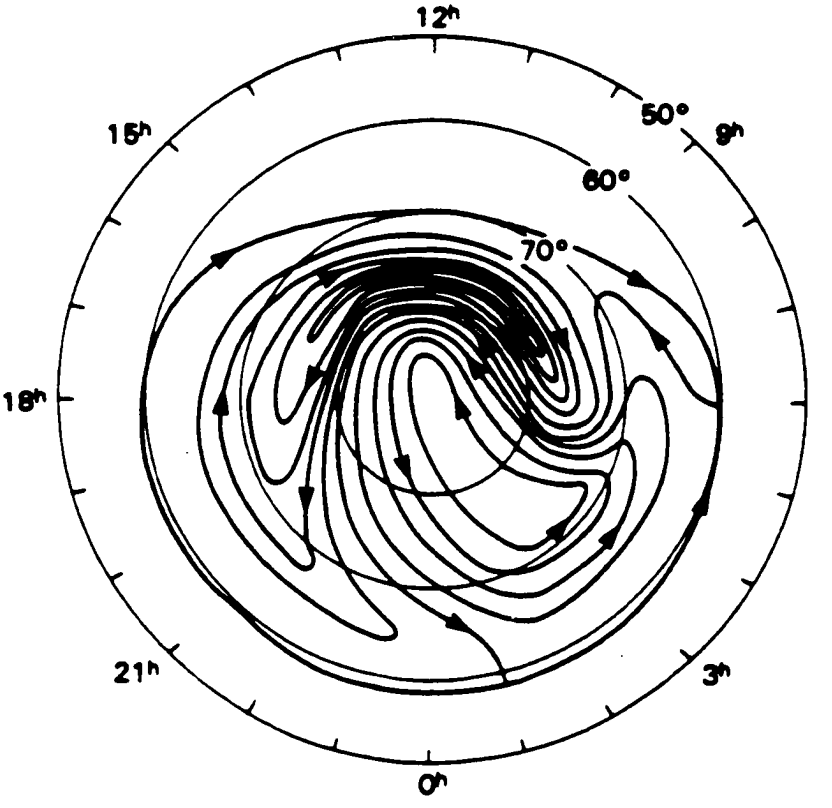

Fig. 3.2. Characteristic convection pattern observed when IMF B_z is strongly positive and B_y is negative [*Heppner and Maynard*, 1987].

1985] into a wrapped two-cell convection pattern [*Heppner and Maynard*, 1987].

In the following, section 3.2 gives a brief description of the physical considerations and the modification of the mathematical formulation for the M-I coupling model during northward IMF. The model inputs and the resulting global convection patterns and distribution of field-aligned current are also given in section 3.2.

Section 3.3 summarizes the main results and discusses the predictions and the applicability of the model.

3.2. Relationship Between Four-Cell and Distorted Two-Cell Convection Patterns During Northward IMF

3.2.1. M-I Coupling Model During Northward IMF

The M-I coupling model in chapter 2 is extended to northward IMF conditions in order to study the relationship between four-cell and wrapped two-cell convection patterns. The initial magnetospheric convection imposed by the solar wind in the present model is four-celled, which may or may not include the effect due to a y-component of the IMF. Note that the emphasis of this research is to study the M-I coupling effects on the high-latitude convection patterns during northward IMF and not to address the details of the origin of the magnetospheric convection imposed by the solar wind. Therefore, the initial magnetospheric convection used in the model are chosen to be as simple as realistically possible.

The extension of the M-I coupling model to northward IMF conditions can be briefly explained as follows. When IMF turns northward, the solar wind imposes a four-cell convection pattern on the magnetosphere [*Kan and Burke*, 1985], which is characteristically different from the two-cell convection pattern during southward IMF. Alfvén waves initiated by the change of the magnetospheric convection are responsible for transmitting the information of the changed magnetospheric convection to the ionosphere. The anisotropic and nonuniform conductance in the ionosphere can lead to the anisotropic reflection of Alfvén waves. Therefore, af-

ter the Alfvén waves bounce between the magnetosphere and the ionosphere, the steady state high-latitude ionospheric convection pattern can be different from the initial magnetospheric convection pattern. This motivates our current studies. How significant the difference between the two convection patterns can be is the question which will be quantitatively answered in the present research.

The basic equations used in the present M-I coupling model for northward IMF conditions are summarized as follows. Note that some equations are modifications of the equations shown in chapter 2, while the other equations are the same as those in chapter 2, which are simply rewritten for the integrity of the current section. For more detailed information about the following equations, refer to chapter 2.

From the current continuity equation, the equation governing the reflection of Alfvén waves from the ionosphere can be written as

$$\begin{aligned} &\Sigma_A \nabla \cdot \left[\mathbf{E}^i(t) - \mathbf{E}^r(t)\right] + J_{\parallel D}(t) \\ &\quad = \nabla \cdot \left[\Sigma_P(t)\mathbf{E}_i(t) + \Sigma_H(t)\mathbf{b}_o \times \mathbf{E}_i(t)\right] \end{aligned} \tag{3.1}$$

and

$$\mathbf{E}_i(t) = \mathbf{E}^i(t) + \mathbf{E}^r(t) + \mathbf{E}_{iP}(t)$$

where $\mathbf{E}^i$ and $\mathbf{E}^r$ are the incident and the reflected Alfvén waves respectively, $J_{\parallel D}$ is the field-aligned current which exists in front of the wave-front of Alfvén waves, and $\mathbf{E}_{iP}$ is the ionospheric electric field excluding the incident and reflected waves. $\Sigma_A = 1/(\mu_o V_A)$ is the equivalent conductance of Alfvén waves. Σ_H and Σ_P are the anisotropic ionospheric Hall conductance and Pedersen conductance respectively,

A reflection coefficient is used in the model to describe the reflection of the outward traveling Alfvén waves at the magnetospheric boundaries, which can be expressed as

$$R_m = -1 \quad \text{on open field lines} \tag{3.2a}$$

$$-1 < R_m < +1 \quad \text{on closed field lines} \tag{3.2b}$$

It may be noted that $R_m = -1$ corresponds to an idealized constant voltage source while $R_m = 1$ corresponds to a constant current source. For a detailed discussion of the physics governing the reflection coefficient R_m, the reader is referred to *Kan et al.* [1988].

Under the assumption that the precipitating electrons are the main external ionization source in addition to solar UV contributions, the time-dependent electron continuity equation can be used to describe the ionization in the E-region of the ionosphere. We have

$$\frac{\partial N}{\partial t} + \nabla \cdot (N\mathbf{V}) = \frac{Q|J_\parallel|}{e} + \frac{|J_\parallel|}{eH} + S_o - \beta N^2 \tag{3.3}$$

where N is the electron number density in the ionosphere, Q is the ionization coefficient which will be defined later in this section, H is the effective height of the conducting ionosphere, β is the recombination coefficient, and S_o is the background source term which can be determined by the input ionospheric conductance. In contrast to the treatment in chapter 2, the second term on the right side in equation (3.3) will be kept in the following derivations. This term could be important in some regions of the ionosphere during northward IMF.

Equation (3.3) can be rewritten, in terms of Σ_H, as

$$\begin{aligned}\frac{\partial \Sigma_H}{\partial t} &= \frac{(QH+1)}{B_o}\nabla\cdot(\Sigma_P \mathbf{E}_i + \Sigma_H \mathbf{b}_o \times \mathbf{E}_i) \\ &+ \frac{eH}{B_o}S_o - \frac{\beta B_o}{eH}\Sigma_H^2 + \nabla\Sigma_H \cdot \frac{\mathbf{b}_o \times \mathbf{E}_i}{B_o}\end{aligned} \tag{3.4}$$

The expression of the ionization coefficient Q is the same as in the chapter 2, namely

$$\begin{aligned}&Q = 0 \quad J_{\|} \text{ downward or } |J_{\|}| < J_o \\ &Q = Q_o \quad J_{\|} \text{ upward and } \nabla\cdot\mathbf{E}_i \geq 0,\ |J_{\|}| > J_o \\ &Q = \gamma'(|J_{\|}| - J_o) \quad J_{\|} \text{ upward and } \nabla\cdot\mathbf{E}_i < 0,\ \ J_o < |J_{\|}| < J_c \\ &Q = \gamma'(J_c - J_o) \quad J_{\|} \text{ upward and } \nabla\cdot\mathbf{E}_i < 0,\ \ |J_{\|}| \geq J_c\end{aligned} \tag{3.5}$$

where Q_o is a constant which depends on the energy of the diffuse auroral precipitation, γ' is a parameter which depends on the $J_{\|} - \phi_{\|}$ relationship [*Fridman and Lemaire*, 1980], J_o is the thermal electron current in the loss cone, and J_c is an equivalent saturation current for the upper limit of available electron energy flux. The ionization coefficient Q is defined as the average number of ions produced by an incident electron per meter, which is proportional to the energy of the precipitating electrons.

Figure 3.3 shows part of the input parameters adopted in the present model. Figure 3.3a shows the initial distribution of the ionospheric Hall conductance and Figure 3.3b shows the contours of the magnetospheric reflection coefficient. To be consistent with the condition of northward IMF, some of the model inputs are modified from those given in chapter 2. These modifications include (1) the ionospheric conductance band has a smaller size and is less intense; and (2) the open field line region, which corresponds to the region where $R_m = -1$, is much

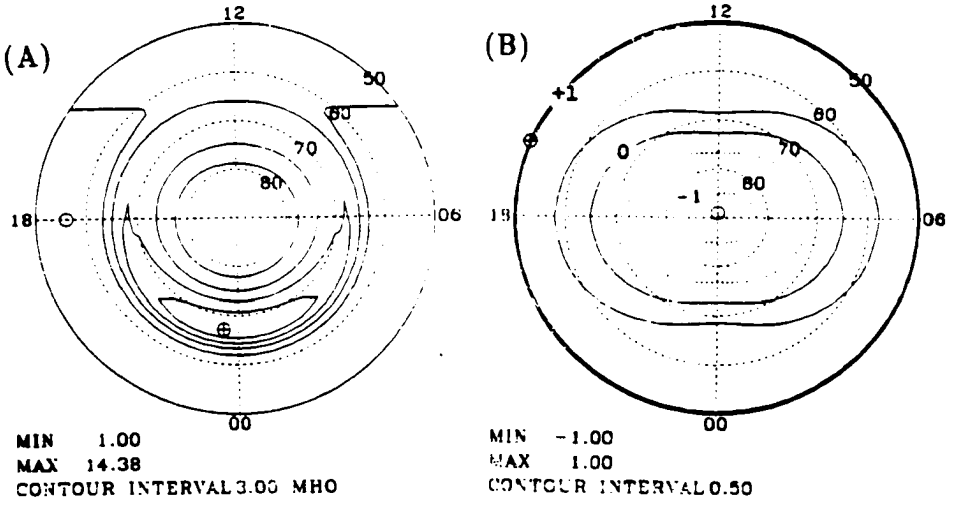

Fig.3.3. Input parameters for the model. (A) Distribution of the ionospheric Hall conductance. (B) Contours of the magnetospheric reflection coefficient.

smaller than that in the previous southward IMF model. Other parameters are specified as follows. The thermal electron current $J_o = 0.08\mu A/m^2$, the equivalent saturation current $J_c = 0.8\mu A/m^2$, the constant ionization coefficient $Q_o = 7 \times 10^{-3}$ ions/e-m, coefficient $\gamma' = 1 \times 10^4$ ions-m/e-ampere [*Rees*, 1963; *Fridman and Lemaire*, 1980], and the recombination coefficient $\beta = 0.9 \times 10^{-13}\mathrm{m}^3/\mathrm{sec}$ [*Walls et al.*, 1974]. The time step is 5 sec and the Alfvén wave traveling time between

time between magnetosphere and ionosphere is assumed to be 4 min. We set t=0 sec when the Alfvén waves launched by the changed magnetospheric convection first arrive in the ionosphere. The input parameters will be kept constant in the following numerical calculations unless specifically mentioned. The equatorward boundary of the convection flow pattern in the numerical calculation has been adjusted to 58° instead of 50° in the previous model for better agreement between the modeling results and the observed ones.

3.2.2. Modeling Results

Figure 3.4 shows the case of strong positive B_z with positive B_y. According to the four-cell theories, when the IMF has a significant y-component, one of the polar cap cells could be dominant over the other one. When B_y is positive, the morning cell in the northern polar cap is dominant, and vice versa. As we can see from Figure 3.4a, these theoretical predictions have been incorporated into the initial magnetospheric convection pattern used in our model. Figures 3.4b and 3.4c show the field-aligned current distribution and the convection pattern in the ionosphere when the M-I coupling process approaches an asymptotic state after about 25 minutes. In Figure 3.4b, the dashed lines mean upward field-aligned currents and the solid lines mean downward field-aligned currents. In the plot, the region 1, region 2 and NBZ currents can be easily identified, with features which are consistent with the observations [*Iijima et al.*,1984]. Furthermore, the field-aligned current distribution shown in Figure 3.4b predicts the features of the currents in the transition region between the region 1 and the NBZ currents in

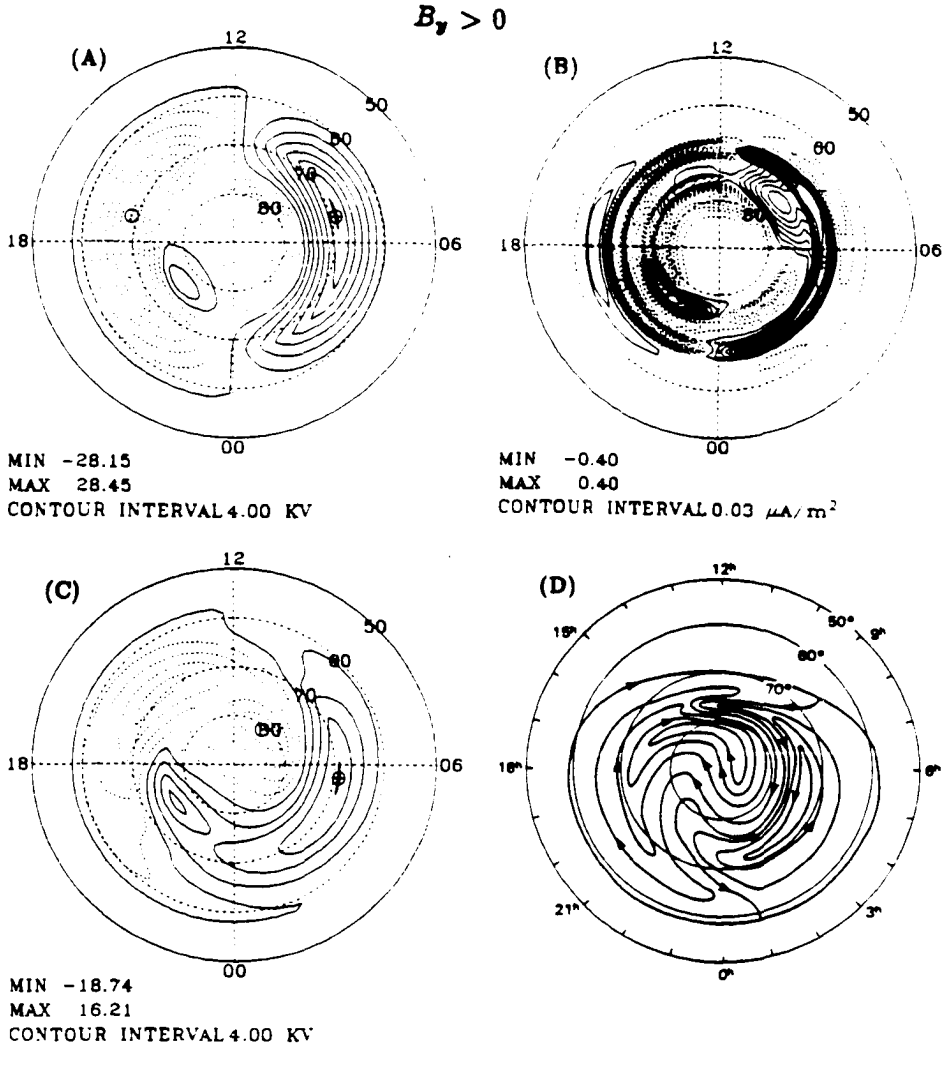

Fig. 3.4. The case of strong positive B_z with a positive B_y. (A) Initial magnetospheric convection. (B) Asymptotic distribution of the field-aligned currents. (C) Asymptotic ionospheric convection pattern. (D) *Heppner-Maynard* convection pattern.

the dayside ionosphere, which could not be observed by the MAGSAT satellite [*Iijima et al.*, 1984] because of its orbit limitations. The most important thing is the asymptotic high-latitude convection pattern shown in Figure 3.4c. Comparing the asymptotic convection pattern with the convection pattern shown in Figure 3.4d, which was observationally deduced by *Heppner and Maynard* [1987], we can see that two convection patterns are characteristically similar with each other and that both have the east-west flow in the dayside regions. A natural conclusion is that four-cell magnetospheric convection patterns, while propagating to the ionosphere, can be distorted and thus lead to the features of wrapped two-cell convection patterns. The convection distortions are caused by the anisotropic reflections of Alfvén waves due to the existence of the anisotropic and nonuniform ionospheric conductance.

Figure 3.5 shows the case of strong positive B_z with negative B_y. Figures 3.5a shows the initial magnetospheric convection pattern. Figure 3.5b and 3.5c show the field-aligned current distribution and the convection pattern in the ionosphere in the asymptotic state. Figure 3.5d shows the observationally deduced convection pattern [*Heppner and Maynard*, 1987]. Again, we can see that the convection patterns shown in Figures 3.5c and 3.5d are quite similar, which supports the conclusion deduced in the previous paragraph. Comparing the field-aligned current distributions shown in Figure 3.4b and Figure 3.5b, another feature which we can see is that when B_y is positive, the downward region 1 current has an expansion towards the polar cap in the prenoon sector, and when B_y is negative, the upward region 1 current has an expansion towards the polar cap in the premidnight sector. This is a predicted feature of the field-aligned currents during conditions of

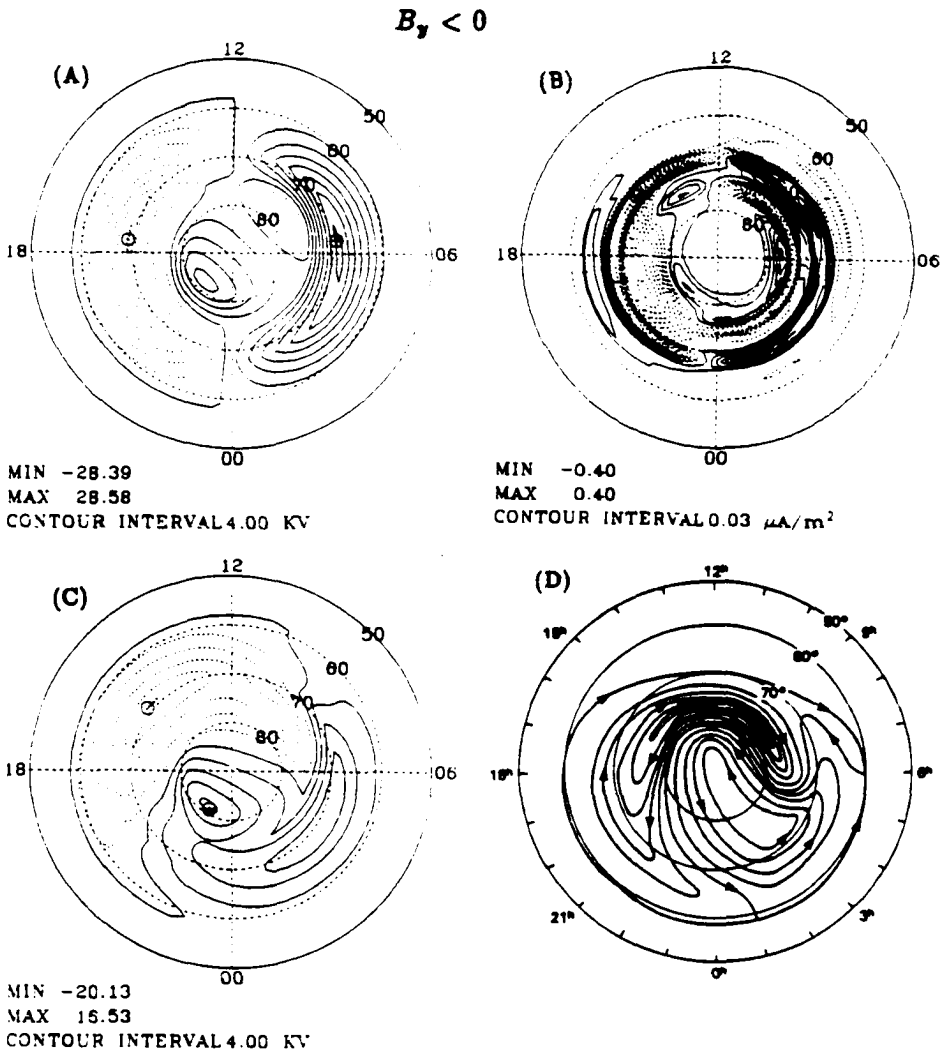

Fig. 3.5. The case of strong positive B_z with a negative B_y. (A) Initial magnetospheric convection. (B) Asymptotic distribution of the field-aligned currents. (C) Asymptotic ionospheric convection pattern. (D) *Heppner-Maynard* convection pattern.

northward IMF in our model.

The situation of $B_y = 0$ is hardly ever observed, but it can be easily achieved in numerical modeling. It can be viewed as an approximation of the case in which the direction of IMF is very close to due north. Figure 3.6a shows a symmetric four-cell magnetospheric convection pattern which is chosen as the initial condition of our model for the case with $B_y = 0$. Figures 3.6b and 3.6c show the outputs in the asymptotic state. The east-west flow features in the dayside regions can still be seen in Figure 3.6b, but not as strongly as those in the cases with a B_y component. The pattern shown in Figure 3.6b can be seen as a natural bridge between the patterns shown in Figure 3.4c and Figure 3.5c if one analyses the morphologies of those patterns carefully. Unfortunately, there is no convection pattern with $B_y = 0$ available in *Heppner and Maynard* paper [1987] against which we can make a direct comparison. Therefore the convection pattern shown in Figure 3.6b can be seen as a theoretical prediction for northward IMF with $B_y = 0$ and an extreme case of the convection patterns for northward IMF shown in *Heppner and Maynard* [1987]. An interesting feature shown in Figure 3.6c is the upward field-aligned currents crossing the polar cap, which might be related to features of the theta aurora.

3.3. Summary

Based on the results of the present modeling, we propose the following relationship between four-cell and distorted two-cell convection patterns during northward IMF. Four-cell convection patterns imposed on the magnetosphere by the

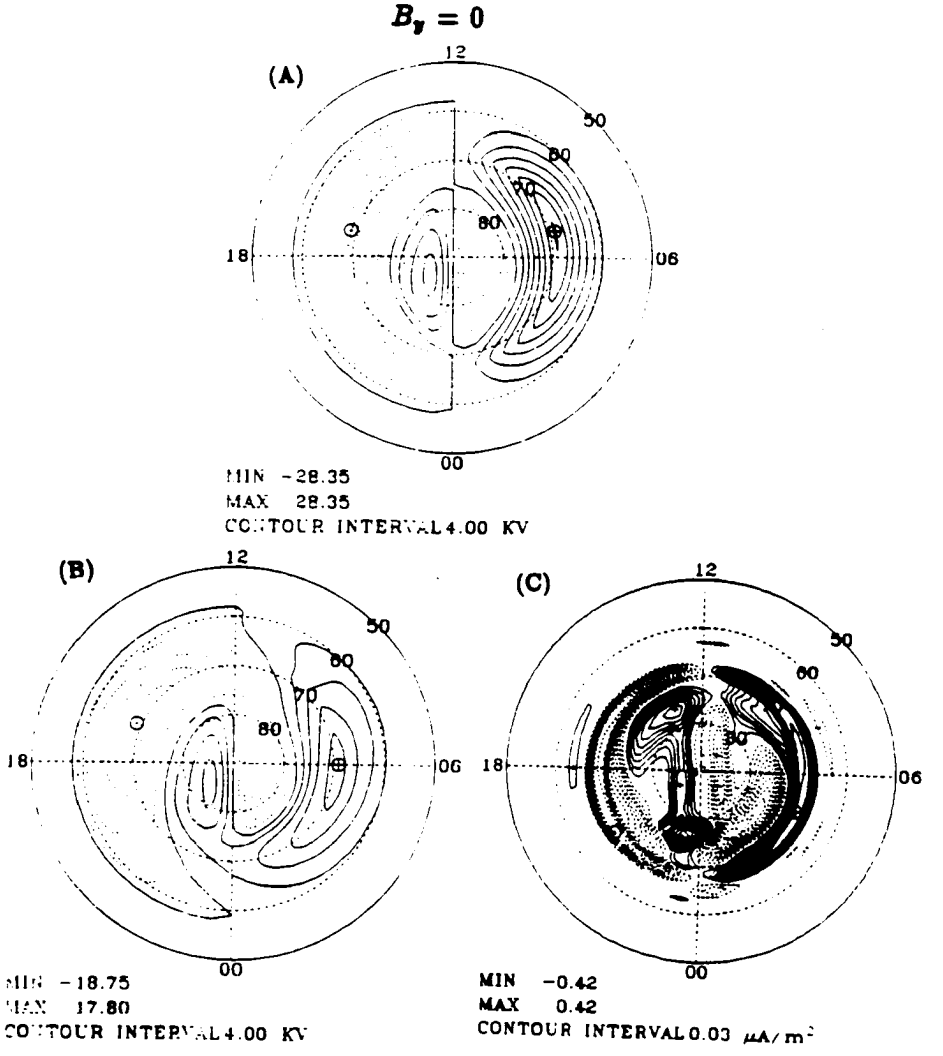

Fig. 3.6. The case of positive B_z with $B_y = 0$. (A) Initial magnetospheric convection. (B) Asymptotic distribution of the field-aligned currents. (C) Asymptotic ionospheric convection pattern.

solar wind during a northward IMF can be distorted into wrapped two-cell convection patterns which are similar to the empirical distorted two-cell convection patterns deduced by Heppner and Maynard [1987]. The convection distortions are caused by the anisotropic reflections of Alfvén waves due to anisotropic and nonuniform ionospheric conductance.

Other results in our modeling can be summarized as follows. First, the model predicts the current features in the transition region between the region 1 and the NBZ currents in the dayside ionosphere. Also, the model predicts that when B_y is positive, the downward region 1 current has an expansion towards the polar cap in the prenoon sector, and when B_y is negative, the upward region 1 current has an expansion towards the polar cap in the premidnight sector. The features of the theta aurora can be seen in the results of the model when the IMF is nearly northward. Additionally, the model predicts a convection pattern for $B_y = 0$ case which can be seen as an extreme case to the convection patterns for northward IMF deduced by *Heppner and Maynard* [1987]. Finally, the distributions of the resulting field-aligned currents in the model are characteristically consistent with observed current distributions, including the NBZ currents, during northward IMF.

Chapter 4. , A Study of the Multiple Field-Aligned Current Sheets in the M-I System

4.1. Introduction

In global modeling of the magnetosphere-ionosphere coupling processes, most attention has been paid to the nightside magnetospheric and ionospheric dynamics. The inclusion of the dayside dynamics in a global M-I coupling model is still in the early stages. One of the possible dynamic processes for transferring the energy and momentum of the solar wind to the magnetosphere through dayside magnetopause is the flux transfer event (FTE) [*Russell and Elphic*, 1978; *Sonnerup et al.*, 1981]. FTEs are characterized by a bipolar oscillation in the normal field component B_n, i.e., positive B_n followed by negative B_n when observed in northern latitudes [*Rijnbeek et al.*, 1982; *Paschmann et al.*, 1982]. Several models of FTEs [*Russell and Elphic*, 1978, 1979; *Saunders et al.*, 1984; *Lee*, 1986; *Sato et al.*, 1986; *Southwood*, 1985, 1987; *Kan*, 1988] have been proposed. According to the FTE theories, the stress applied to the reconnected flux tube as it is pulled tailward must be transmitted to the ionosphere. This must be accomplished by closing the field-aligned currents associated with the flux tube through the ionosphere. It is believed that the field-aligned current in the FTE flux tube plays a key role in coupling the FTE to the ionosphere.

Before we can include dayside FTEs into the global modeling of the magnetosphere-ionosphere coupling, we need to verify the validity of different interpretations of FTEs. One applicable way is a search for the FTEs signatures in

the ionosphere [*Goertz et al.*, 1985; *Lanzerotti et al.*, 1986] and on the ground [*McHenry and Clauer*, 1987]. Such independent observations would provide considerable strength to the arguments supporting the interpretations of FTEs, and would also provide another source of observational information regarding dayside magnetopause reconnection. Ground magnetic signatures produced by the coaxial cylindrical FTE current systems proposed by *Saunders et al.* [1984] and *Lee* [1986], and by the split cylindrical FTE current system proposed by *Southwood* [1985, 1987] have been examined by *McHenry and Clauer* [1987]. In this chapter, we examine the ground magnetic signatures and the ionospheric signatures produced by the multiple FTE field-aligned current sheets proposed by *Kan* [1988]. The results show that the ground magnetic signature of the FTE model proposed by *Kan* [1988] is characteristically different from the magnetic signatures of previously proposed FTE models [*Saunders et al.*, 1984; *Lee*, 1986; *Southwood*, 1985, 1987] as calculated by *McHenry and Clauer* [1987]. The results also suggest that ground magnetometer chains could be a potential tool to test the predictions of the various FTEs models.

This chapter is organized in the following way. Section 4.2 briefly introduces the FTE multiple field-aligned current sheet system proposed by *Kan* [1988], and the characteristic features of the coaxial cylindrical and split cylindrical FTE current systems. Section 4.3 gives the mathematical formulation of the present work. Section 4.4 shows the resulting ground magnetic signatures and ionospheric signatures of the multiple field-aligned current sheets, and makes a comparison of the magnetic signatures predicted by various FTE models. Finally, in section 4.5, we summarize the major results and make a brief conclusion.

4.2. Current Systems Associated With the FTE Flux Tube

Kan [1988] proposed a theory of the elbow-shaped flux transfer events [*Russell and Elphic*, 1978; 1979]. The FTE theory proposed by *Kan* [1988] can produce multiple field-aligned current sheets, accompanied by spiky electric fields along enhanced convection channels. Figure 4.1 is a sketch of a convection channel driven by an intermittently enhanced elbow-shaped FTE centered around a given longitude on the dayside magnetopause. The convection along a channel is nonuniform due to the intermittency of elbow-shaped FTEs. A pair of oppositely directed field-aligned currents is produced by the FTE along a convection channel due to the ionospheric line-tying effect [e.g., *Southwood*, 1985, 1987]. The intensity of the upward current need not be equal to that of the downward current in each FTE enhanced convection channel [*Kan*, 1988], so that a net field-aligned current can exist to produce helical field lines along an elbow-shaped FTE flux tube. The longitudinal dimension of an FTE flux tube is determined by the width of the localized FTE reconnection site. The latitudinal dimension of an FTE flux tube depends on the convection speed and the duration of the intermittent reconnection on the dayside magnetopause. Thus, an elbow-shaped FTE flux tube can be highly elongated in the direction of the convection if the patchy reconnection is sustained for a long time. In that case, the FTE field-aligned current sheets can be highly extended along a convection channel [*Kan*, 1988]. Multiple pairs of field-aligned current sheets are produced by multiple FTEs at different longitudes on the dayside magnetopause. Multiple field-aligned current sheets imbedded in the region I current system [*Iijima and Potemra*, 1976] can be inferred from

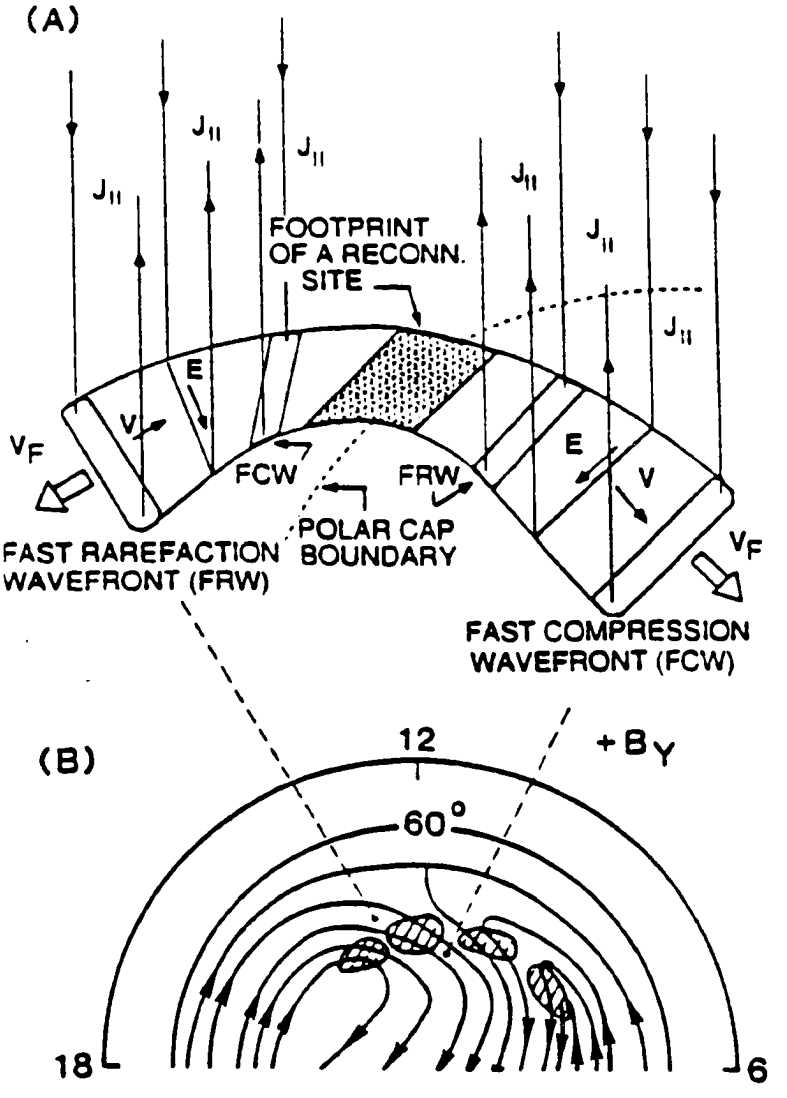

Fig. 4.1. (A) Sketch of an isolated convection channel projected on the ionosphere driven by the intermittently enhanced elbow-shaped FTEs on the dayside magnetopause. The cross-shaded region is the footprint of a 3DT reconnection site on the magnetopause. The open arrows indicate the velocity fast-mode waves. The solid arrows indicate the convection velocity along the channel. Field-aligned currents are indicated by vertical lines with arrows. (B) The dayside ionospheric convection pattern driven by the intermittently enhanced elbow-shaped FTEs on the dayside magnetopause. The curves with arrows are convection streamlines.

magnetic field data measured by polar orbiting satellites. Examples of multiple field-aligned current sheets have been deduced from DE 2 magnetometer data [e.g., *Sugiura*, 1984].

The other two proposed current systems associated with an FTE flux tube are the coaxial cylindrical and the split cylindrical FTE current systems. The first consists of a central core of field-aligned current which spreads radially in the ionosphere. The current closes with field-aligned return currents in a diffuse shell around the central core current or through distant return currents [*Saunders et al.*, 1984; *Lee*, 1986]. The second consists as a first approximation of two oppositely directed field-aligned currents on opposing edges of the FTE flux tube [*Southwood*, 1985, 1987]. A refined version distributes the currents over the circumference of the flux tube. Figure 4.2 is a sketch to show the characteristic difference of the multiple field-aligned current sheets, the coaxial cylindrical current system, and the split cylindrical current system.

4.3. Mathematical Formulation

The steady state magnetic signature of the multiple current sheets in the FTE model proposed by *Kan* [1988] will be calculated under the following assumptions. (1) The ionosphere is assumed to be a slab with uniform height-integrated Hall and Pederson conductances. Using the data from the Sondrestrom radar and the NOAA 7 and TRIAD satellites, *Robinson et al.* [1984] showed that in the dayside ionosphere, the height-integrated ionospheric conductance is almost uniform in a region around a small-scale current system. Therefore, a uniform height-integrated

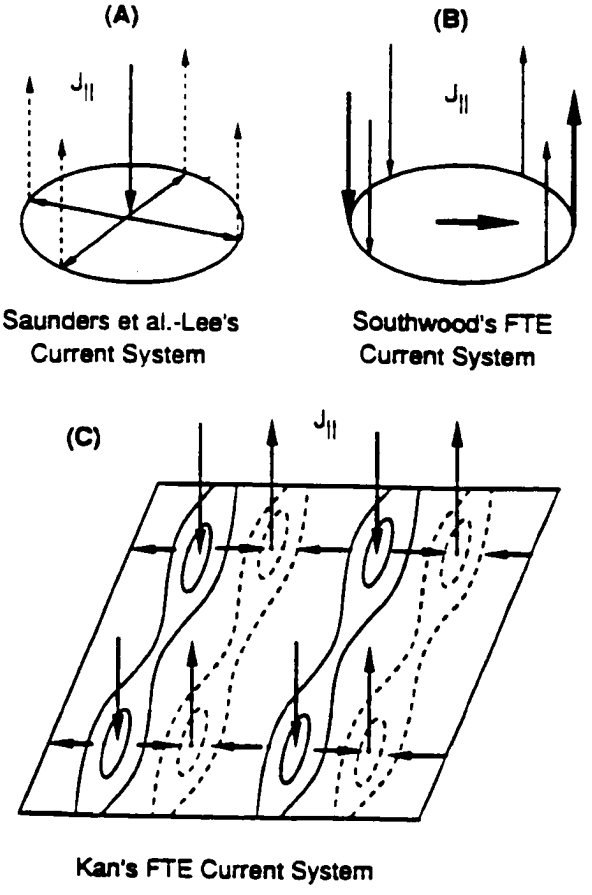

Fig. 4.2. The sketch of three FTE current systems presented in various FTE models. (A) The Coaxial cylindrical FTE current system [*Saunders et al.*, 1984; *Lee*, 1986]. (B) The split cylindrical FTE current system [*Southwood*, 1985; 1987]. (C) The multiple FTE field-aligned current sheets [*Kan* , 1988]. The dashed arrows indicate the upward field-aligned current.

conductance is a good assumption for the dayside ionosphere. (2) The Earth's magnetic field is assumed to be perpendicular to the ionosphere. In the high latitude, this is a commonly accepted assumption. (3) The Earth's induction currents are assumed negligible. Assuming a uniform Earth conductivity, the Earth can be simplified as an infinitely conducting sphere covered by a perfect insulating layer which is at least 250 km in thickness [*Chapman*, 1919; *Kisabeth and Rostoker*, 1977; *Campbell*, 1987]. The effect of the Earth induction currents can be estimated by adding image currents below the surface of the conducting sphere at the same distance as the ionospheric currents are above that surface. That means the image currents are about 600 km below the Earth's surface. It will be shown later that the magnetic perturbations produced by the current system in our model decrease rapidly with distance. Therefore, the Earth induction currents can be assumed negligible.

A cartesian coordinate system is adopted in which the X axis points to the north, the Y axis points to the east and the Z axis is downward. The ionosphere is in the X-Y plane. The ionospheric current, flowing in X-Y plane, can be expressed as

$$\mathbf{I} = \Sigma_P \mathbf{E} + \Sigma_H \mathbf{b}_o \times \mathbf{E} \tag{4.1}$$

where $\mathbf{b}_o$ is the unit vector of magnetic field assumed to be in the Z direction, $\mathbf{E}$ is the ionospheric electric field assumed to be in X-Y plane, and Σ_P and Σ_H are integrated Pederson and Hall conductances, respectively. From the current continuity equation, one obtains

$$\nabla \cdot \mathbf{I} = J_{\parallel}(x, y) \tag{4.2}$$

where $J_{\|}(x,y)$ is the field-aligned current density. From equations (4.1) and (4.2), one can derive the relation

$$\nabla \cdot (\Sigma_P \mathbf{E} + \Sigma_H \mathbf{b}_o \times \mathbf{E}) = J_{\|} \tag{4.3}$$

Under the assumptions of uniform ionospheric conductance and of a curl-free electric field

$$\mathbf{E} = -\nabla \Phi \tag{4.4}$$

equation (4.3) can be simplified as

$$\nabla^2 \Phi = \frac{-J_{\|}(x,y)}{\Sigma_P} \tag{4.5}$$

where Φ is the electric potential.

By solving equation (4.5), we obtain Φ for a given Σ_P and $J_{\|}$ under a specified boundary condition on Φ. We then calculate the distribution of the ionospheric electric field $\mathbf{E}$ from equation (4.4) and the ionospheric current from equation (4.1). To get the ground magnetic perturbation, we use the Biot-Savart law,

$$d\mathbf{B} = \frac{\mu_o}{4\pi r^3}(\mathbf{J} \times \mathbf{r})dV \tag{4.6}$$

According to *Fukushima*'s theorem [1969], if the conductance is uniform and the field-aligned current is perpendicular to the ionosphere, the ground magnetic perturbation is produced exclusively by the Hall current. The magnetic perturbations produced by the Pederson current and the field-aligned current cancel each other. Therefore, in our model, equation (4.6) can be rewritten as

$$d\mathbf{B}(\mathbf{r}_o) = \frac{\mu_o}{4\pi r'^2}(\mathbf{I}_H(\mathbf{r}) \times \hat{\mathbf{r}}')dxdy \tag{4.7}$$

where $\mathbf{I}_H$ is the ionospheric Hall current, $\mathbf{r}_o$ is the observation point on the ground, $\mathbf{r}$ is the source point in the ionosphere, r' is the magnitude of $\mathbf{r}' = \mathbf{r}_o - \mathbf{r}$, and $\hat{\mathbf{r}}'$ is the unit vector in the direction of $\mathbf{r}'$. Then the integrated ground magnetic perturbation can be expressed as

$$\mathbf{B}(x_o, y_o) = \int\int \frac{\mu_o}{4\pi r'^2}(\mathbf{I}_H \times \hat{\mathbf{r}}')dxdy \tag{4.8}$$

where the area of integration is the entire ionosphere, and x_o and y_o are the x and y components of $\mathbf{r}_o$, respectively.

If the average height from the ground to the ionosphere is denoted by h, one can calculate the ground magnetic perturbation produced by the ionospheric current explicitly from equation (4.8), i.e.,

$$\mathbf{B}(x_o, y_o) = \frac{\mu_o}{4\pi}\int\int \frac{1}{\left[(x_o - x)^2 + (y_o - y)^2 + h^2\right]^{3/2}}\Big\{I_y h\mathbf{e}_x - I_x h\mathbf{e}_y + \Big[(y_o - y)I_x - (x_o - x)I_y\Big]\mathbf{e}_z\Big\}dxdy \tag{4.9}$$

where I_x, and I_y are the components of $\mathbf{I}_H$.

By solving equations (4.1), (4.4), (4.5), and (4.9), both the ground magnetic perturbation and the ionospheric electric field can be calculated when the ionospheric conductance and the distribution of the field-aligned current are given.

If the field-aligned current sheet has a large longitudinal extent compared with its latitudinal extent, equation (4.9) can be simplified by assuming that the current density is uniform in the longitudinal direction. Then equation (4.9) can be rewritten as

$$\mathbf{B}(x_o) = \frac{\mu_o}{2\pi}\Big(\int \frac{I_H(x)h}{(x_o - x)^2 + h^2}dx\mathbf{e}_x - \int \frac{I_H(x)(x_o - x)}{(x_o - x)^2 + h^2}dx\mathbf{e}_z\Big) \tag{4.10}$$

The positive value of $I_H(x)$ is for eastward flowing current.

4.4. Ground and Ionospheric Signatures of the Multiple Field-Aligned Current Sheets

4.4.1. Ground Magnetic Signatures

To obtain the ground magnetic signature associated with the multiple field-aligned current sheets due to FTEs, we numerically solve equations (4.1), (4.4), (4.5), and (4.9). We assume a Gaussian distribution in space for the field-aligned current density in each current sheet. The longitudinal and latitudinal extents of an individual field-aligned current sheet are adjustable. The former is determined by the width of the localized reconnection site. The latter depends on the convection speed and the duration of the intermittent reconnection on the dayside magnetopause. The uniform ionospheric conductances are assumed to be $\Sigma_P = 6$ mho and $\Sigma_H = 9$ mho, and the ground to ionosphere distance is assumed to be h =100 km in all calculations presented in this paper. The calculation domain consists of a 100 by 100 uniform grid which is confined in a area of 1000 km by 1000 km. We use periodic boundary conditions on the boundaries at $y = 0$ km and $y = 1000$ km. On the boundaries at $x = 0$ km and $x = 1000$ km, the boundary condition, $\partial\Phi/\partial x = 0$ is used to obtain a solution with zero current on the boundary. We also assume that the field-aligned current sheets are aligned along the east-west direction, which is appropriate outside the polar cap. Since the amplitude of most magnetic perturbations from other sources is less than 30 nT, we would say the magnetic signatures produced by multiple current sheets are above

the detectable level if their amplitude is larger than 30 nT.

Figure 4.3 shows the ground magnetic perturbation associated with two-dimensional multiple field-aligned current sheets. The left panel in the top row shows the spatial distribution of current density of multiple field-aligned current sheets. This type of multiple field-aligned current sheets can be produced by the collective contribution of intermittently generated elbow-shaped FTEs. In this case, we only consider the multiple field-aligned current sheets with symmetric intensities, which means the same intensities for both upward and downward $J_{\parallel}$ in each pair. The current density of $J_{\parallel}$ is assumed to be 7 μA/m^2 at the maximum. The longitudinal dimension of individual field-aligned current sheet, which equals the longitudinal size of the FTE footprint in the ionosphere, is set to 300 km, and the latitudinal dimension of individual field-aligned current is set to be 100 km. The latitudinal distance between the ionospheric footprints of different FTEs is set to be 400 km. The remaining panels in Figure 4.3 show the different components of the corresponding ground magnetic perturbations.

From the plots shown in Figure 4.3 we can see that the maximum amplitude of the H component perturbation is greater than 165 nT in this case. Such a perturbation could be easily identified from the magnetometer data. The Z component perturbation is relatively weak compared with the H component perturbation, but is still of detectable level. The magnetic perturbation of the D component associated with the multiple field-aligned current sheets is extremely weak and so will be undetectable. From these plots, we find some interesting characteristics of the magnetic signatures in the different components. The magnetic signature of the D component perturbation exhibits fine structures. Each set of fine structures

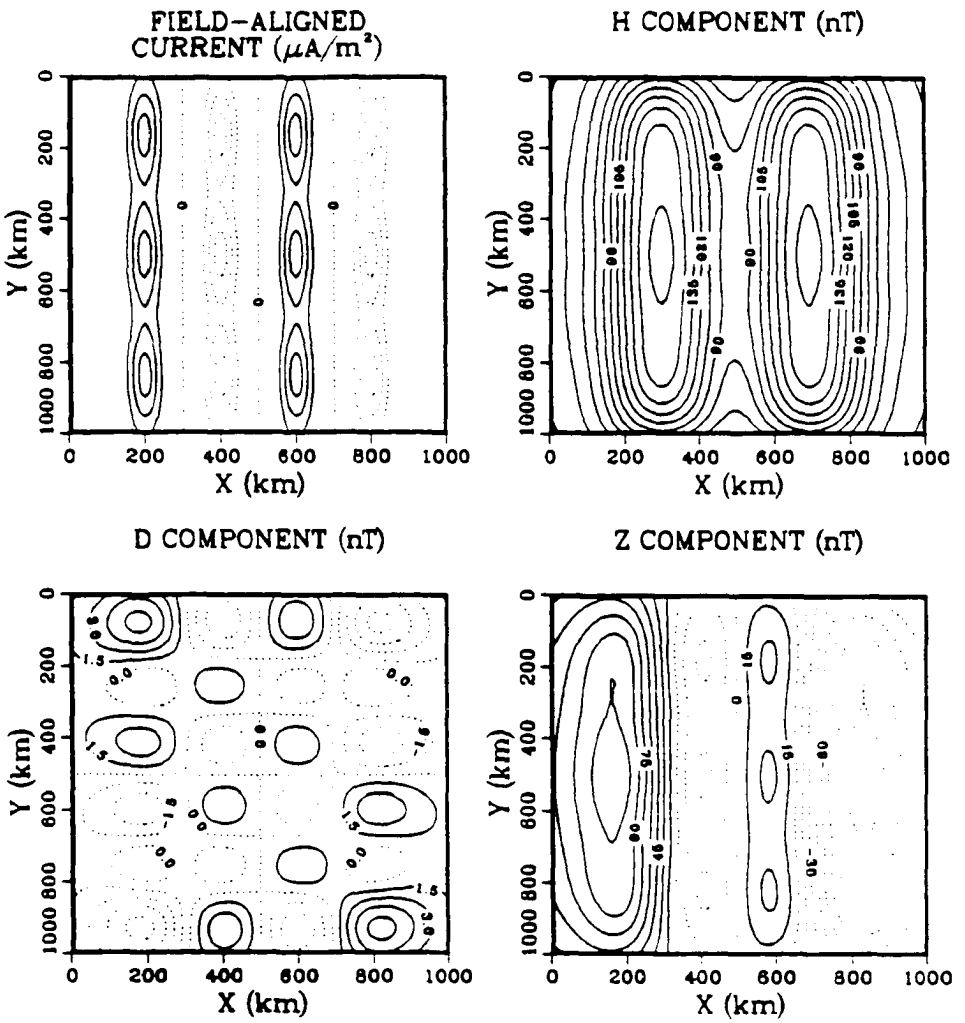

Fig. 4.3. The typical case of multiple field-aligned current sheets and the corresponding ground magnetic perturbations. The contours of $J_{\|}$ are spaced 2 $\mu A/m^2$. Dotted lines mean negative values.

is believed to be connected with a FTE flux tube. The ground signatures associated with different field-aligned current sheets can be easily identified through the pattern of the H component perturbation. But the magnetic perturbation of the H component is highly localized, and is well confined just under the multiple FTE field-aligned current sheets. Fortunately, the Z component spreads over a wider ground area than the H component. This will increase the chance of detecting FTE ground signatures through magnetometer observations.

In the calculations, we find that the intensity of the current in an FTE is an important factor to the detectability of the magnetic perturbations by ground magnetometers. If the maximum $J_{\parallel}$ is reduced to 3 $\mu A/m^2$, not only the D component perturbation but also the Z component perturbation are below the detectable level. If the $J_{\parallel}$ is further reduced to 1.5 $\mu A/m^2$, all three component perturbation are below the detectable level.

Figure 4.4 shows how the longitudinal size of individual current sheets influences the ground magnetic signature. In this case, we keep the same latitudinal distance between the ionospheric footprints of different FTEs ($\sim$400 km) and the same intensities of $J_{\parallel}$ as in the previous case. But the longitudinal size of current sheet in Figure 4.4 is 900 km, while that in Figure 4.3 is 300 km. Note that the amplitude of ground magnetic perturbations in Figure 4.4 is much larger than that in Figure 4.3. This means the longitudinal size of FTEs is also important in determining the characteristics of ground magnetic perturbation. We find if the longitudinal size of the FTE footprint is smaller than 100 km, the amplitude of ground magnetic perturbations will be below the detectable level even if the current density of $J_{\parallel}$ is as high as 7 $\mu A/m^2$. In our calculations, we also checked

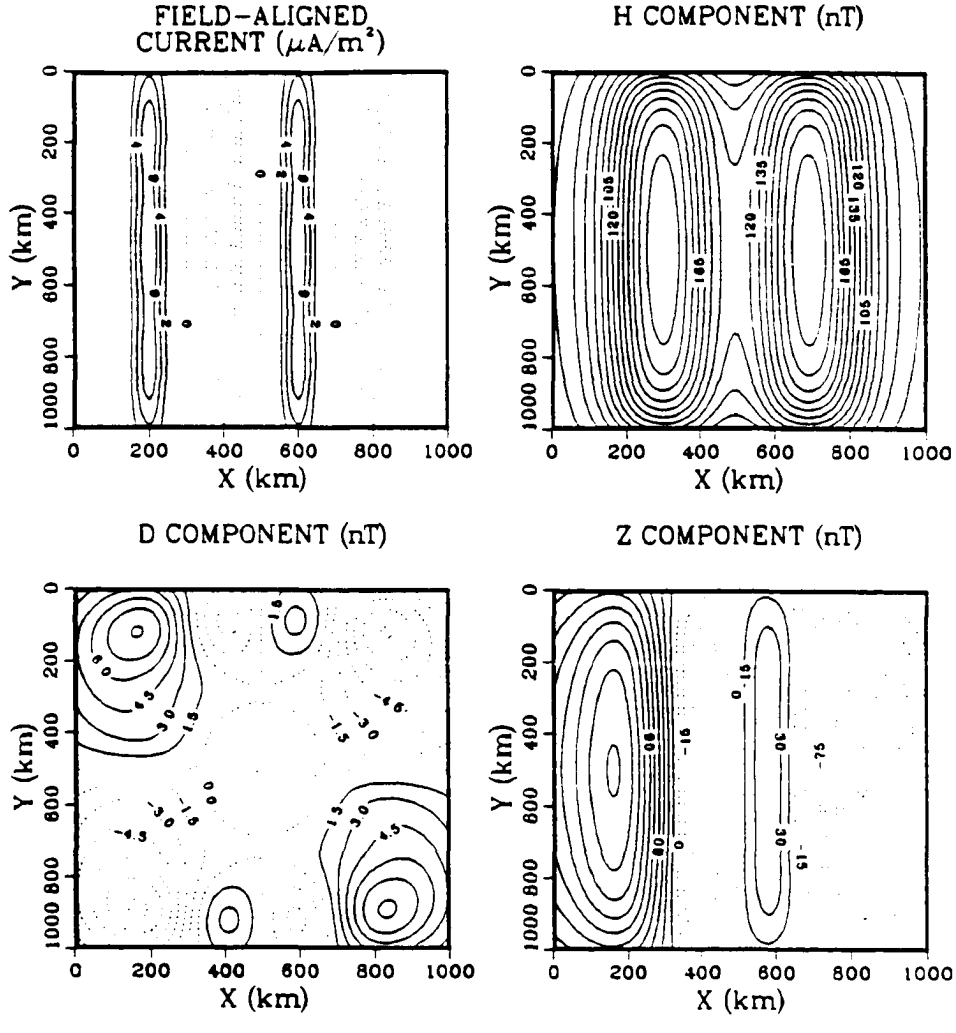

Fig. 4.4. The case showing how the longitudinal size of individual field-aligned current influences the ground magnetic signatures.

how the latitudinal size of individual current sheets influences the ground magnetic signature. We find the latitudinal size is also an important factor. If the latitudinal size of an individual current sheet is smaller than 30 km, the magnetic signature is hard to identify from magnetic records, since the maximum amplitudes of the perturbation of both the H component and the Z component are lower than 30 nT. Thus, we conclude that when the reconnection site has a large width, or when the intermittent reconnection on the dayside magnetopause has a longer duration, there is more chance of detecting the ground magnetic signatures associated with multiple field-aligned current sheets. Figure 4.5 shows the case in which FTEs occur with a small spatial separation in latitudinal direction at the magnetopause. We set the corresponding spatial separation in the ionosphere to be 240 km, but the rest of the parameters are the same as in Figure 4.3. Note that both the H and Z component perturbations are weaker than those in Figure 4.3. This result shows that a smaller spatial separation makes the magnetic perturbations produced by different current sheets cancel each other. This will reduce the chances of being detected by ground magnetometers. Furthermore, the smaller spatial separation between different current sheets makes the magnetic footprint on the ground smaller. This will also reduce the chances of being detected. This suggests that ground magnetometer data might be a good tool for studying the current structure of individual FTE.

The intensity of the upward current need not be equal to that of the downward current in each pair of FTE field-aligned current sheets so that a net field-aligned current can exist to produce helical field lines along an elbow-shaped FTE flux tube. Figure 4.6 shows the case in which the FTE multiple field-aligned current

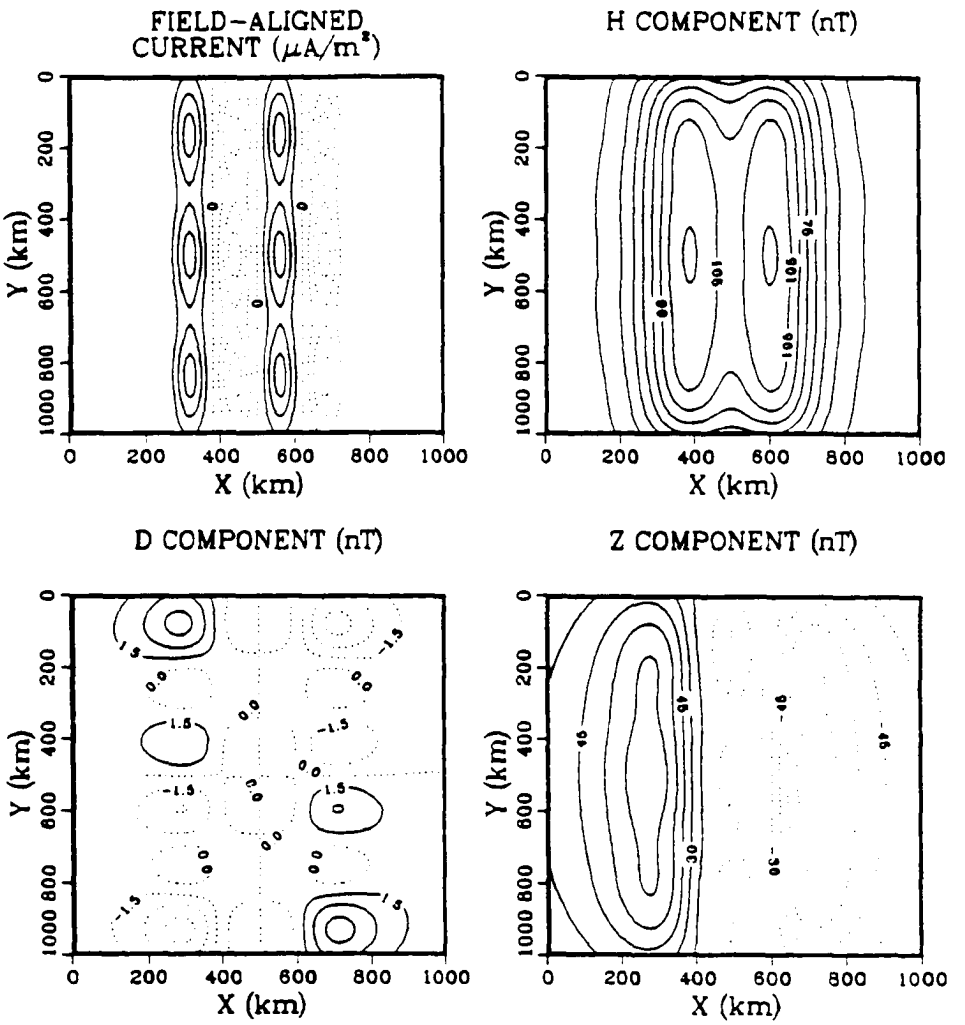

Fig. 4.5. The case in which FTEs occur with a small spatial separation in latitudinal direction at the magnetopause. The contours of $J_{\|}$ are spaced 2 $\mu A/m^2$.

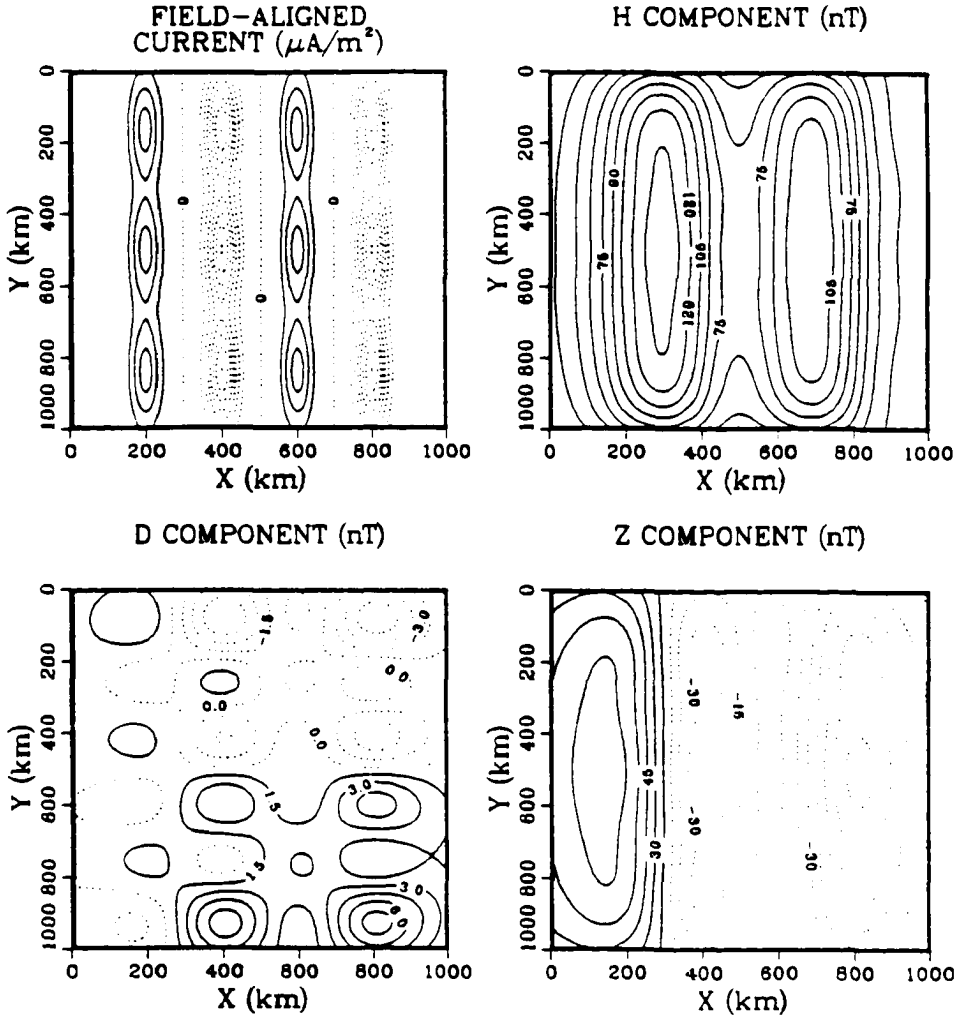

Fig. 4.6. The case in which the multiple FTE field-aligned current sheets have unsymmetric current intensities. The contours of $J_{||}$ are spaced 2 $\mu A/m^2$.

sheets have unsymmetric current intensities. The left panel in the top row shows the distribution of field-aligned current density. In this case, the upward current density is significantly greater than the downward current density. The maximum current density of upward $J_{||}$ is 7 $\mu A/m^2$. The ratio of the current density of upward $J_{||}$ to that of downward $J_{||}$ is 2. Naturally, there are some unsymmetric characteristics in the magnetic signature. We find that when the upward current density is significantly greater than the downward current density in FTE current system, the negative Z component perturbation spreads over a much wider ground area than the positive Z component. On the other hand, when the downward current density is significantly greater than the upward current density in FTE current system, the positive Z component perturbation spreads over a much wider ground area. This is a useful result which can be used as a crude diagnosis to find out the dominant direction of $J_{||}$ in a FTE current system.

4.4.2. Ionospheric Electric Field Signatures

During the calculation of ground magnetic signatures shown in subsection 4.4.1, we can also calculate the ionospheric electric fields associated with multiple field-aligned current sheets. The plots in Figure 4.7 show the profiles of the X (northward) component of ionospheric electric field. The solid curves represent the X components of electric field along the latitudinal cross section where the maximum current densities of field-aligned current sit. The dashed curves represent the fields along the latitudinal cross section where the minimum current densities are located. The curves in Figure 4.7*a* are the corresponding electric

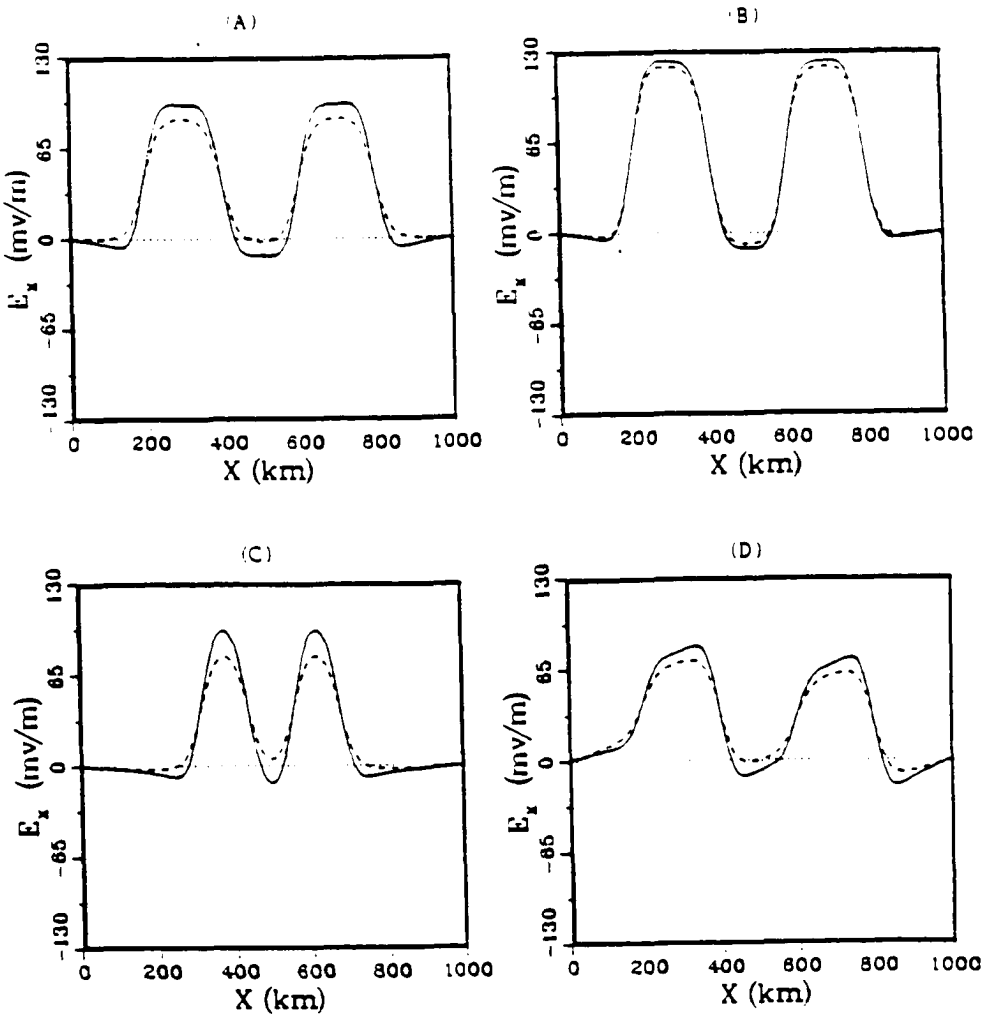

Fig. 4.7. The profiles of the X component of the ionospheric electric field. The solid curves represent the electric fields along the latitudinal cross section where the maximum current densities sit. The dashed curves represent the electric fields along the latitudinal cross section where the minimum current densities sit. Plots (A), (B), (C), and (D) correspond to the cases shown in Figure 4.3, Figure 4.4, Figure 4.5, and Figure 4.6, respectively.

fields to the case shown in Figure 4.3. Figure 4.7*b* corresponds to the case with a larger longitudinal size of the FTE footprints shown in Figure 4.4. Figure 4.7*c* corresponds to the case with a smaller spatial separation between different current sheets which is shown in Figure 4.5. Finally, Figure 4.7*d* corresponds to the case in which the FTE multiple field-aligned currents have unsymmetric current intensities shown in Figure 4.6.

From the plots shown in Figure 4.7, we find a common characteristic: the intensities of the electric fields peak near the center and fall off toward the edge of an FTE tube. This is consistent with the characteristic of spiky electric fields associated with FTEs proposed by *Kan* [1988]. We also find that if the intensity of multiple field-aligned current sheets is fixed, then the FTE tube with a larger size produces a stronger ionospheric electric field. Since the convection electric field is produced by the collective contribution from individual reconnection sites, a strong convection electric field can be expected when the FTE tubes have larger sizes at the magnetopause. The smaller spatial separations between different current sheets do not reduce the intensity of electric field, but do reduce the intensity of ground magnetic perturbation (as shown in section 3.1). The sharp spiky electric fields occur in the case of smaller spatial separations. Because the current density in the case shown in Figure 4.7*d* is unsymmetric, the resulting electric field also exhibits some unsymmetric features. The peaks of electric field intensity shift towards the side of the larger current density instead of sitting at the center of FTE tube. The signatures of ionospheric electric fields shown in Figure 4.7 can be used to make comparison with the electric field data from polar orbiting satellites and offer another tool for testing the proposed FTE theories.

4.4.3. Comparison of Magnetic Signatures Predicted by Various FTE Models

The ground magnetic signatures produced by the multiple field-aligned current sheets in *Kan*'s [1988] FTE model are compared with the coaxial cylindrical FTE current system [*Saunders et al.*, 1984; *Lee*, 1986] and the split cylindrical FTE current system [*Southwood*, 1985, 1987] as shown in Figure 4.8. To facilitate the comparison, the multiple field-aligned current sheets are assumed to be aligned along the north-south direction which is appropriate inside the polar cap. The geometries of these three field-aligned current systems have been shown schematically in Figure 4.2.

The top panels of Figure 4.8 show the ground magnetic signatures produced by multiple FTE field-aligned current sheets proposed by *Kan* [1988]. (The input of field-aligned current sheets is obtained by simply rotating the $J_{\parallel}$ profile in Figure 4.3 by 90°.) The magnetic signatures shown in the middle and the bottom panels are the results presented in *McHenry and Clauer*'s [1987] work. The middle panels show the magnetic signatures produced by the split cylindrical FTE current system. The bottom panels show that produced by the coaxial cylindrical FTE current system. For the purpose of comparison, we take the net upward (or downward) current to be around 2×10^5A for the multiple FTE field-aligned current sheets, which is consistent with the net upward current (2×10^5A) used for the split cylindrical FTE current system and the coaxial cylindrical FTE current system in *McHenry and Clauer*'s [1987] calculations. The B_x components in the middle and the bottom panels correspond to the H component in the top panel

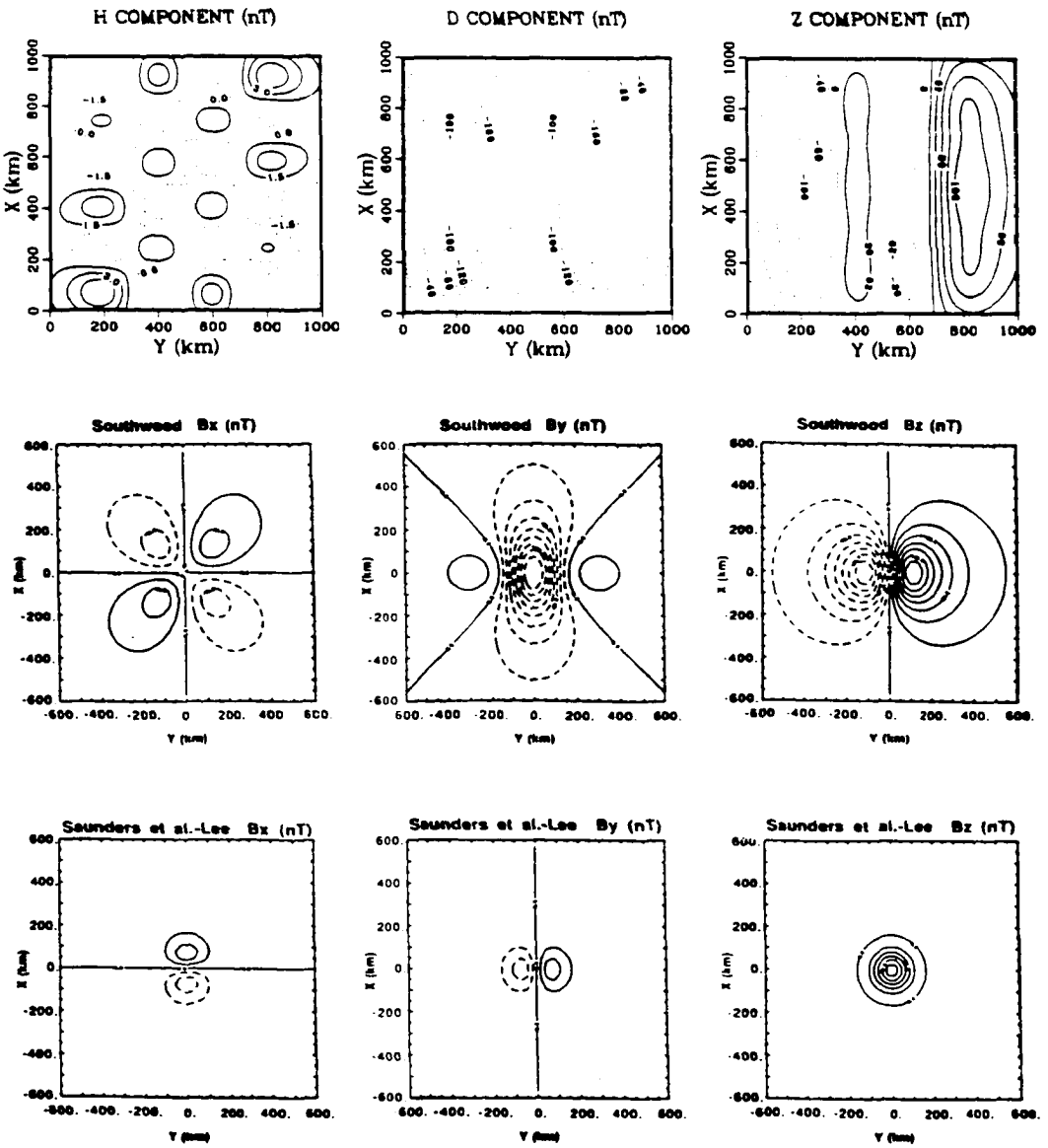

Fig. 4.8. The comparison of ground magnetic signatures produced by three different FTE current systems. (Top) The ground magnetic signatures produced by Kan's FTE model. (Middle) The ground magnetic signatures produced by Southwood's FTE model. (Bottom) The ground magnetic signatures produced by Saunders et al.'s and Lee's FTE models. All contours are spaced 20 nT except the left one in the top panels, which is spaced 1.5nT.

in which the positive value is northward. The B_y component corresponds to the D component in which the positive value is eastward. The positive Z component points to the Earth. The contours of all patterns are spaced at 20 nT intervals except the left pattern in the top row, which is spaced at 1.5 nT intervals.

Obviously, the pattern of magnetic signatures produced by the multiple FTE field-aligned current sheets is characteristically different from those produced by coaxial cylindrical FTE current system and split cylindrical FTE current system. The magnitude of D component perturbation in the top row is slightly larger than the corresponding component perturbation in the middle row but is much larger than that in the bottom row. The magnitudes of Z component perturbations in all three current systems are of the same order of magnitude. Note the H component perturbation produced by the multiple current sheets is much weaker than the corresponding component perturbation produced by the other two current systems, but that it also shows some very fine structures.

From the comparison of the ground magnetic signatures produced by these three different FTE current systems, we find that the coaxial cylindrical FTE current system proposed by *Saunders et al.* [1984] and *Lee* [1986] has the least chance to be identified from the ground magnetic data, since its ground perturbations are weakest and it has the smallest area compared with the other two current systems. The multiple FTE field-aligned current sheets proposed by *Kan* [1988] has the best chance to be identified, since its ground magnetic perturbations are the strongest and have the largest ground areas.

4.5. Summary

The ground magnetic signatures associated with multiple FTE field-aligned current sheets proposed by *Kan* [1988] have been studied under the assumption of uniform ionospheric conductance. The characteristics of the resulting ionospheric electric fields in the model are consistent with that of the spiky electric fields associated with FTEs proposed by *Kan* [1988]. The ground magnetic signatures associated with different multiple field-aligned current sheets, shown in Figures 4.3 to 4.6, can be summarized as follows.

The H component of magnetic perturbation associated with multiple field-aligned current sheets dominates the Z and D component perturbation. The H component perturbation is highly localized and is confined just under the multiple current sheets. The Z component perturbation is weaker and less confined compared with the H component perturbation. The magnetic perturbation of the D component associated with multiple field-aligned current sheets is probably too weak to be detectable, but it has some very fine structure which can reflect the characteristics of individual FTE flux tubes.

If the current density of multiple field-aligned current sheets is greater than 1.5 $\mu A/m^2$ with a longitudinal size of an individual current sheet being larger than 100 km, and a latitudinal width being larger than 30 km, then the ground magnetic signature associated with multiple field-aligned current sheets probably could be identified from ground magnetometer data .

A smaller closer spatial separation between different current sheets makes the magnetic perturbation produced by different current sheets cancel out and leads

to weaker ground magnetic perturbations. Fortunately, even for very small spatial separation, the ground signature produced by different current sheets can still be easily distinguished.

When the upward current density is significantly greater than the downward current density in an FTE current system, the negative Z component perturbation spreads over a much wider ground area than the positive Z component perturbation. Conversely, when the downward current density is significantly greater than the upward current density in an FTE current system, the positive Z component perturbation spreads over a much wider ground area.

In conclusion, the ground magnetic signatures of the FTE model proposed by *Kan* [1988] are shown to be characteristically different from the magnetic signatures of the two previously proposed FTE models [*Saunders et al.*, 1984; *Lee*, 1986; *Southwood*, 1985, 1987] which were modeled by *McHenry and Clauer* [1987]. The current system in *Kan*'s FTE model is more readily detectable by the ground magnetometers, since its ground magnetic perturbations are the strongest and cover the largest area compared with the magnetic perturbations produced by the other two FTE models. The predicted magnetic signatures presented in this work and in *McHenry and Clauer*'s [1987] paper can be used as a diagnostic tool to test the various theories proposed for FTEs.

Chapter 5. Interactions Between Alfvén Waves and Double Layers

5.1. Introduction

The importance of Alfvén waves in the M-I coupling has been shown in previous chapters and by others [*Scholer*, 1970; *Maltsev et al.*,1974; *Mallinchrodt and Carlson*, 1978; *Miura and Sato*, 1980; *Goertz and Boswell*, 1979; *Kan*, 1982; *Lysak and Dum*, 1983; *Kan and Sun*, 1985; *Lysak*, 1986; *Kan*, 1988]. The field-aligned potential drop is an important element on auroral field lines. Therefore, interactions between Alfvén waves and field-aligned potential drops can be of fundamental importance in the M-I coupling processes.

A field-aligned potential drop can be maintained either by the anomalous resistivity process or by the nonresistive double layer process [*Kan*, 1982]. Interactions between Alfvén waves and a resistive potential drop have been analyzed by *Lysak and Dum* [1983] in a local model. Interactions between Alfvén waves and a nonresistive double layer have not been studied in either a local model or as a component in global M-I coupling model. Note that in the M-I coupling model presented in previous chapters, we have included the effects of field-aligned potential drop on the ionization of the ionospheric conductance, but we have not considered the interactions between Alfvén waves and field-aligned potential drops.

Field-aligned potential drops on auroral field lines have been observed to be localized in tens of Debye lengths [*Temerin et al.*, 1982], but have also been observed to be extended to about 1 R_E or more [*Mizera and Fennell*, 1977]. If the auroral potential drop is associated with double layer process, the former can be

called a "localized" double layer, the latter called the an "extended" double layer. In this chapter, we formulate a local model to study the interactions between Alfvén waves and a 1-D localized double layer. The interaction is a two-way process: the transmission and the reflection of Alfvén waves by the double layer depends on the pre-existing double layer potential, and the field-aligned current and the perpendicular electric field of the resulting waves in turn modify the double layer potential. The transmitted waves and the reflected waves which carry the information of the double layer then propagate towards the ionosphere and the magnetosphere respectively, which can produce some features associated with the double layer in the ionosphere and the magnetosphere. The results presented in this chapter can be an useful first step for developing a more realistic model of interaction between Alfvén waves and an extended double layer potential, and for building the interaction between Alfvén waves and field-aligned potential drop into global M-I coupling models.

The chapter is organized in the following way. Section 5.2 presents a brief introduction of the major features of the field-aligned potential drop and the proposed mechanisms for originating and maintaining the field-aligned potential drop. In section 5.3, a local model of the interactions between Alfvén waves and a 1-D localized double layer is presented. The mathematical formulation of the model and the features of the interactions resulting from the numerical calculation will be displayed in this section. Section 5.4 summarizes the major features of the interactions between Alfvén waves and a localized double layer and discusses the implications of the model results.

5.2. Field-Aligned Potential Drop

Discrete aurora are curtain-like forms extending over a few 1000 km in the east-west direction. The precipitating electrons responsible for producing the discrete aurora show a characteristic peak at energies $\sim$ 1 to 10 keV, indicating that the precipitating electrons have been accelerated through a field-aligned potential drop of 1 to 10 kV [*Kan*, 1982].

The perpendicular scale length of the auroral potential drop ranges from $\sim$ 100 m on the arc-element scale [*Davis*, 1978] to $\sim$ 100 km on the inverted V scale [*Frank and Ackerson*, 1971]. Observations indicate that the field-aligned scale length of the auroral potential drop can be around tens of Debye lengths [*Temerin et al.*, 1982] in some cases, but can also be as large as 1 R_E or more [*Mizera and Fennell*, 1977].

Field-aligned potential drops can be forced into existence by the loss-cone constriction effect due to converging geomagnetic field [*Knight*, 1973; *Fridman and Lemaire*, 1980; *Lyons*, 1980]. The loss-cone limits the precipitating electron flux and thereby the field-aligned current to the thermal flux of electrons whose pitch angles fall within the loss-cone. If the field-aligned current required by the ionosphere exceeds the loss-cone thermal flux limit, the requirement can be met by establishing a field-aligned potential drop to accelerate electrons into the loss-cone and thus increase the precipitating electron flux to carry the field-aligned current as required by the ionosphere. Thus, potential drops along converging field lines are required if the upward field-aligned current density is to exceed the loss-cone limit.

Several mechanisms maintaining the field-aligned potential drop have been proposed, namely: (1) the double layer process; (2) the anomalous resistivity process; (3) the electrostatic shock process; and (4) thermoelectric potential process. Only the first two processes are associated with field-aligned current. A double layer is a potential structure, characterized by two layers of space charge, self-consistently supported in a current-carrying plasma. Figure 5.1 is a schematic diagram showing the typical structure of a double layer. Note that the downward return currents are located on both sides of the upward current in this potential drop structure. In the anomalous resistivity process, the field-aligned potential drop is supported by anomalous resistivity, which is a consequence of plasma turbulence in which current carrying electrons are scattered and slowed down by collisions with wave electric fields. Depending on whether or not there is resistivity in the process, a double layer process can lead to a nonresistive field-aligned potential drop and an anomalous resistivity process can lead to a resistive field-aligned potential drop.

5.3. Interactions Between Alfvén waves and a 1-D Localized Double Layer

5.3.1. Basic Model

In this subsection we formulate a model for the interactions between Alfvén waves and a localized double layer based on the MHD equations. To focus on the most fundamental nature of the interaction between an Alfvén wave and the double layer, the following assumptions are introduced:

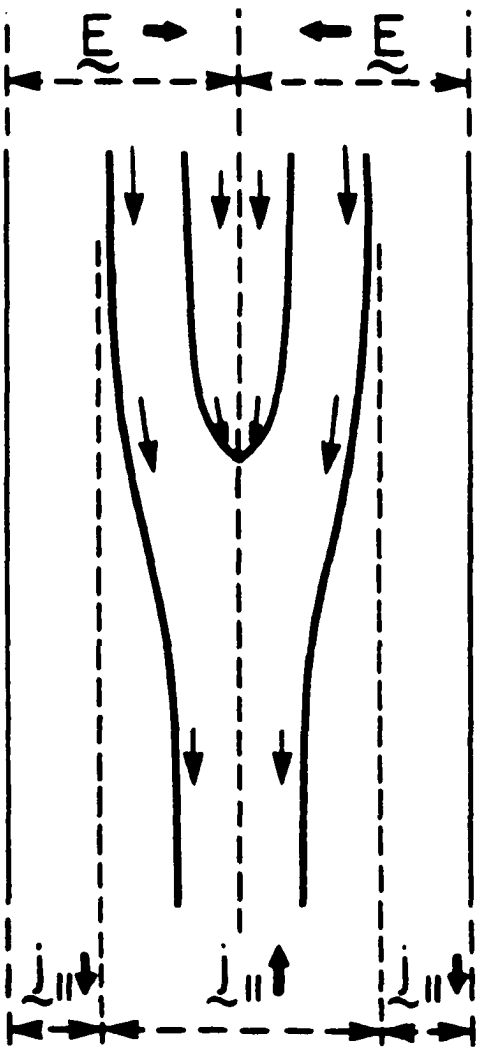

Fig. 5.1. Schematic diagram of the double layer structure.

(a) The medium is assumed to be uniform. This simplifying assumption is introduced to exclude partial reflection of Alfvén waves due to nonuniformity along the field lines. Partial reflections in reality are probably small compared with the reflections from the double layer.

(b) The double layer is assumed to be a thin layer and to obey the current-voltage relationship due to the loss-cone constriction effect [*Knight*, 1973; *Fridman and Lemaire*, 1980; *Lyons*, 1980].

(c) The subsequent reflections from the magnetosphere and the ionosphere are excluded. This assumption allows us to focus on the interactions between an Alfvén wave and the double layer without the involvement of a specific magnetosphere and a specific ionosphere. Due to the assumption, the initial model has to be time-independent, but it does expose the fundamental nature of the interactions.

Potential drop along converging field lines is required to allow the upward field-aligned current density to exceed the loss-cone limit [*Knight*, 1973; *Fridman and Lemaire*, 1980; *Lyons*, 1980]. The resulting current-voltage relationship is nonlinear and depends on the altitude of the potential drop [*Yamamoto and Kan*, 1985]. As a first approximation, the current-voltage relationship of a double layer can be approximated by

$$\begin{aligned} J_{\parallel} &= G_{+}\Phi_{\parallel} \qquad & J_{\parallel} > 0 \\ J_{\parallel} &= G_{-}\Phi_{\parallel} \qquad & J_{\parallel} \leq 0 \end{aligned} \tag{5.1}$$

where $G_{+} = 10^{-8}$ to 10^{-9} mho m^{-2} [*Lyons et al.*, 1979; *Weimer*, 1985] and $G_{-} \gg G_{+}$. The field-aligned current $J_{\parallel} > 0$ is chosen for upward current, flowing

away from the ionosphere; the potential drop $\Phi_{\parallel} > 0$ is chosen for potential rise toward the ionosphere. For $J_{\parallel} < 0$, $\Phi_{\parallel} < 0$ which is of no importance as far as acceleration of auroral electrons are concerned. The absolute value of $\Phi_{\parallel}$ is negligible for $J_{\parallel} < 0$ because $G_{-} \gg G_{+}$. Thus, for all practical purposes we assume $\Phi_{\parallel} \approx 0$ for $J_{\parallel} \leq 0$.

The field-aligned potential drop can be written as

$$\Phi_{\parallel} = \Phi_i - \Phi_m \tag{5.2}$$

where Φ_i and Φ_m are respectively the potentials on the magnetospheric and ionospheric sides of the double layer. Taking gradient of (5.2) perpendicular to the field lines, one obtains

$$\mathbf{E}_m - \mathbf{E}_i = \nabla_{\perp}\Phi_{\parallel} \tag{5.3}$$

where $\mathbf{E}_m$ and $\mathbf{E}_i$ are perpendicular to the ambient magnetic field.

The field-aligned current carried by an Alfvén wave can be written as (refer to chapter 2)

$$J_{\parallel A} = \pm\Sigma_A \nabla_{\perp} \cdot \mathbf{E}_A \tag{5.4}$$

where "$-$" and "$+$" signs are respectively defined for downgoing (toward the ionosphere) and upgoing (away from the ionosphere) Alfvén waves in the northern hemisphere, $\Sigma_A = (\mu_o V_A)^{-1}$, $V_A = B_o/(\mu_o \rho)^{1/2}$ is the Alfvén speed, B_o is the ambient field magnitude, ρ is the mass density and μ_o is the permeability of free space in *MKS* units. For $V_A = 1000$ to 2000 km/sec, $\Sigma_A = 0.5$ to 1 mho.

In the presence of an Alfvén wave, equation (5.1) can be rewritten as

$$\Phi_{\|o} + \Phi'_{\|} = G^{-1}(J_{\|o} + J'_{\|}) \tag{5.5}$$

where $J_{\|o} = G_o \Phi_{\|o}$ is the current-potential relationship prior to the arrival of the Alfvén wave, while $J'_{\|}$ is the net field-aligned current of the wave and $\Phi'_{\|}$ is the potential drop due to the Alfvén wave. Both G_o and G can be spatial functions, whose values are determined by the signs of the field-aligned currents, as defined in equation (5.1). The distribution of G_o is determined by $J_{\|o}$, and the distribution of G is determined by the total current $(J_{\|o} + J'_{\|})$. By using the relationship $J_{\|o} = G_o \Phi_{\|o}$, equation (5.5) can be rewritten as

$$\Phi'_{\|} = J_{\|o}(G^{-1} - {G_o}^{-1}) + G^{-1} J'_{\|} \tag{5.6}$$

In the presence of Alfvén waves, equation (5.3) can be rewritten as

$$\mathbf{E}_{mo} + \mathbf{E}'_m - \mathbf{E}_{io} - \mathbf{E}'_i = \nabla_\perp \Phi_{\|o} + \nabla_\perp \Phi'_{\|} \tag{5.7}$$

Since $\mathbf{E}_{mo} - \mathbf{E}_{io} = \nabla_\perp \Phi_{\|o}$ is for the pre-existing fields and double layer potential, equation (5.7) is reduced to

$$\mathbf{E}'_m - \mathbf{E}'_i = \nabla_\perp \Phi'_{\|} \tag{5.8}$$

where $\mathbf{E}'_m$ and $\mathbf{E}'_i$ are the Alfvén wave electric fields on the magnetospheric and ionospheric sides of the double layer.

After the interaction between the Alfvén wave and the double layer, the current continuity equation in the MHD plasma requires that the field-aligned current of the wave must be equal on the two sides of the double layer, i.e.,

$$J'_{\parallel} = J'_{\parallel m} = J'_{\parallel i} \tag{5.9}$$

where $J'_{\parallel m}$ and $J'_{\parallel i}$ are associated with the Alfvén wave electric fields $\mathbf{E}'_m$ and $\mathbf{E}'_i$ respectively. Equations (5.4), (5.6), (5.8), and (5.9) are the governing equations for the interaction between an Alfvén wave and a nonresistive localized double layer.

Since the subsequent reflections of the Alfvén waves from the magnetosphere and the ionosphere are excluded in the present model, the most interesting situation must be the interaction between a downgoing (or incident) Alfvén wave with a large scale upward field-aligned current and a double layer potential drop. In such a case, we have

$$\begin{aligned} \mathbf{E}'_m &= \mathbf{E}^i + \mathbf{E}^r \\ \mathbf{E}'_i &= \mathbf{E}^t \end{aligned} \tag{5.10}$$

where $\mathbf{E}^i$, $\mathbf{E}^r$ and $\mathbf{E}^t$ are the incident, the reflected and the transmitted wave electric fields respectively. Inserting (5.10) into (5.8) leads to

$$\mathbf{E}^r + \mathbf{E}^i - \mathbf{E}^t = \nabla_\perp \Phi'_{\parallel} \tag{5.11}$$

Equation (5.9) can be rewritten as

$$J'_{\parallel} = J_{\parallel}{}^i + J_{\parallel}{}^r = J_{\parallel}{}^t \tag{5.12}$$

Substituting (5.4) into (5.12) yields

$$J'_{\parallel} = \Sigma_A \nabla \perp \cdot (\mathbf{E}^r - \mathbf{E}^i) = -\Sigma_A \nabla_\perp \cdot \mathbf{E}^t \tag{5.13}$$

Inserting (5.13) into (5.6) yields

$$\Phi'_{\parallel} = J_{\parallel o}(G^{-1} - {G_o}^{-1}) - G^{-1}\Sigma_A \nabla_{\perp} \cdot \mathbf{E}^t \tag{5.14}$$

By eliminating $\mathbf{E}^r$ and $\Phi'_{\parallel}$ from equations (5.11), (5.13) and (5.14) and using (5.4), we obtain

$$G^{-1}\nabla^2 {J_{\parallel}}^t - 2{\Sigma_A}^{-1}{J_{\parallel}}^t = ({G_o}^{-1} - G^{-1})\nabla^2 J_{\parallel o} - 2{\Sigma_A}^{-1}{J_{\parallel}}^i \tag{5.15}$$

Equations (5.4) (5.5) (5.12) and (5.15) form the final working equations for the interaction between an incident Alfvén wave and a localized double layer.

The numerical procedure for solving the above working equations can be summarized as the follows. First of all, equation (5.15) is solved with an arbitrary initial constant G (either G_+ or G_-), where $J_{\parallel o}$ and ${J_{\parallel}}^i$ are given, and G_o is chosen to be consistent with $J_{\parallel o}$. An updated G is then obtained in terms of the calculated total current $(J_{\parallel o} + {J_{\parallel}}^t)$, where the distribution of G is consistent with the distribution of total current. Then (5.15) is solved again with an updated G. This kind of iteration goes on until self-consistent solutions of ${J_{\parallel}}^t$ and G are achieved. With the self-consistent solutions of ${J_{\parallel}}^t$ and G, the field-aligned current carried by the reflected wave can be calculated from (5.12). Then (5.4) is solved to obtain the incident, the reflected and the transmitted wave electric fields. Finally, the modified double layer potential can be obtained from (5.5).

5.3.2. Numerical Results

A cartesian coordinate system is adopted in which the X axis points to the

north, the Y axis points to the east, and the Z axis is downward along magnetic field lines. In the present model, a pre-existing localized double layer is treated as a thin layer with zero thickness in Z direction. The double layer is assumed to be elongated uniformly in the east-west direction with an inverted V-shape variation of potential drop in the north-south direction. An upward field-aligned current flows along the central part of the pre-existing double layer with downward field-aligned currents on both edges. In the most interesting situations, the incident Alfvén wave associated with enhanced convection is assumed to carry large scale upward field-aligned current.

Figure 5.2 shows the case in which an incident Alfvén wave carrying uniform upward field-aligned current interacts with a pre-existing double layer with a maximum field-aligned potential drop of around 1.5 kV. The meanings of different curves are shown by the figure legend.

The bottom panel of Figure 5.2 shows the features of the wave electric fields during the interaction. The result shows that the propagation of an incident Alfvén wave can be partially blocked by a nonresistive double layer potential, and the wave is split into a reflected wave and a transmitted wave. It is found that there is no wave energy absorption during such an interaction process since the double layer under study is nonresistive, which is in contrast with the interactions between an Alfvén wave and an anomalous resistivity potential drop [*Lysak and Dum*, 1983]. One important feature is that the perpendicular electric field of the reflected wave is in the same direction as the incident wave. This feature suggests that during the interactions between Alfvén wave and a double layer, on the magnetospheric side of the double layer, an intensified convection field should

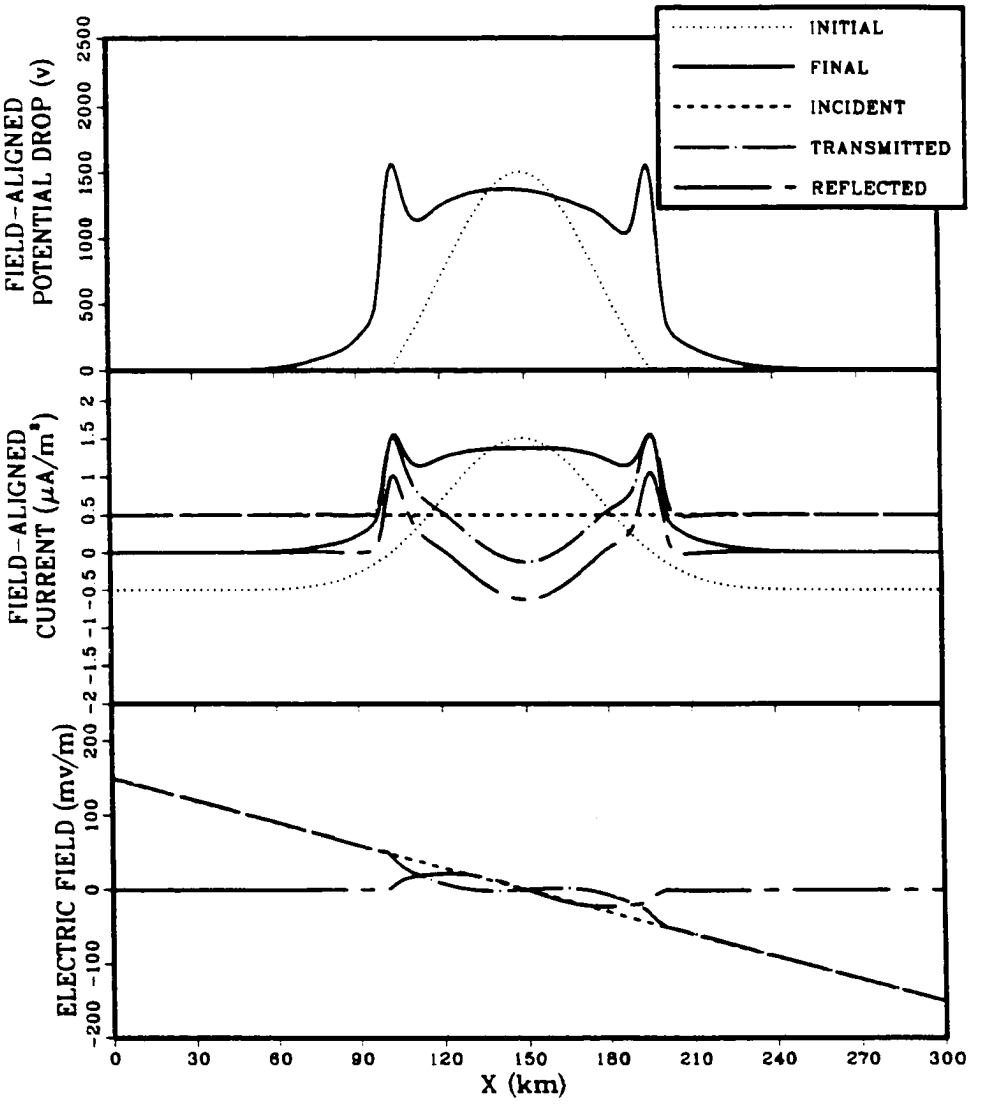

Fig. 5.2. The case in which an incident wave carrying uniform upward field-aligned current interacts with a double layer with a maximum field-aligned potential drop of 1.5 kV.

appear with a relatively weak convection field on the ionospheric side.

The above reflection and transmission characteristics of an Alfvén wave have significant consequences for the magnetosphere-ionosphere coupling processes. As shown by the bottom plot in Figure 5.2, on the field lines without potential drop, an enhanced magnetospheric convection carried by Alfvén waves can propagates to the ionosphere without any reflection and directly drive the ionospheric dynamical processes. Because of the finite ionospheric conductance, the ionosphere in turn drags the enhanced magnetospheric convection and reduces the magnetospheric electric field through the reflected wave field from the ionosphere. But on the field lines with double layers, the situation is totally different. On one hand, the ionosphere can not receive the full information of the enhanced magnetospheric convection because of the strong reflection of Alfvén waves by double layers. On the other hand, the magnetosphere is decoupled from the ionospheric drag by double layers. Such a decoupling can lead to small scale intensified flow in the magnetospheric convection, which has been shown by the resulting electric field feature in which the reflected field and the incident field reinforce with each other. The intensified perpendicular electric field in the magnetosphere were observed by the ISEE 1 [*Cattell et al.*, 1982] and S3-3 satellites [*Mozer et al.*, 1980]. The model result given above could provide a possible explanation for these observed magnetospheric features.

The middle panel of Figure 5.2 shows the features of field-aligned currents during the interactions. The result shows that on the field lines with double layer, the field-aligned currents carried by the reflected wave flow downward in the central part of the double layer while flowing upward on the edges. Since $J_{\parallel}{}^{t} =$

$J_{\parallel}^{i} + J_{\parallel}^{r}$, the field-aligned current associated with the transmitted wave has a similar structure with the field-aligned current associated with the reflected wave. These field-aligned current features can be explained in terms of the relationship between the wave electric field and the associated field-aligned current. Since in the central part of the double layer $J_{\parallel}^{r}$ is downward, the reflected wave field must have a negative slope according to equation (5.4). On the field lines without potential drop, the incident wave field is undisturbed, therefore, the reflected wave field must go back to zero at the edges of the double layer through a positive slope. In terms of equation (5.4), the reflected wave field with a positive slope must then carry an upward field-aligned current. On the field lines without a double layer, reflected wave field is zero, therefore $J_{\parallel}^{r}$ must be zero as shown in the middle panel. The final total field-aligned current is the sum of the pre-existing field-aligned current and the field-aligned current carried by the transmitted wave.

These features show that the downward field-aligned current carried by the reflected wave can suppress the pre-existing upward field-aligned current and flatten the current distribution in the central region of the double layer. On the other hand, the small scale upward field-aligned current also carried by the reflected wave can leads to intensified small scale upward field-aligned current at the edges of modified double layer.

The top panel of Figure 5.2 shows the features of the potential drop during the interactions. The result shows that an incident Alfvén wave can also modify a double layer potential while the wave is partially blocked by the double layer. Due to the characteristics of the field-aligned currents associated with the reflected and the transmitted waves, the central part of the pre-existing double layer potential

is suppressed and flattened, and small scale intensified potential drops appear at the both edges of the double layer. The small scale intensified upward field-aligned currents and potential drop resulting from the interactions between an Alfvén wave and double layer can probably be used to explain the observed thin east-west aligned structures of discrete aurora.

Figure 5.3 shows the case in which an incident Alfvén wave carrying uniform upward field-aligned current interacts with a pre-existing double layer with a maximum field-aligned potential drop of around 1 kV. Comparing Figure 5.3 with Figure 5.2 shows that increasing the strength of a double layer at a fixed scale size leads to stronger reflected wave field and weaker transmitted wave field, which means that a strong decoupling occurs between the magnetosphere and the ionosphere when there is a strong double layer.

The cases shown by Figures 5.4, 5.5 and 5.6 display the effects of the perpendicular size of the double layer during the interactions. Figure 5.4 shows the case in which the ratio between the wave length of the incident Alfvén wave and the perpendicular size of the double layer $\psi = 15$. Figure 5.5 shows the case with $\psi = 8$ and the same of double layer strength as in Figure 5.4, and Figure 5.6 shows the case with $\psi = 4$. From the comparison among these cases, we can see that for a double layer with a given maximum potential drop, a smaller perpendicular size can lead to a much stronger downward field-aligned current carried by reflected wave in the central part of the double layer. This a result can be explained in the following way. As shown in Figure 5.2 and 5.3, for a given incident Alfvén wave, a stronger double layer potential drop leads to a reflected wave with a larger amplitude. Therefore if the incident wave and the strength of a double

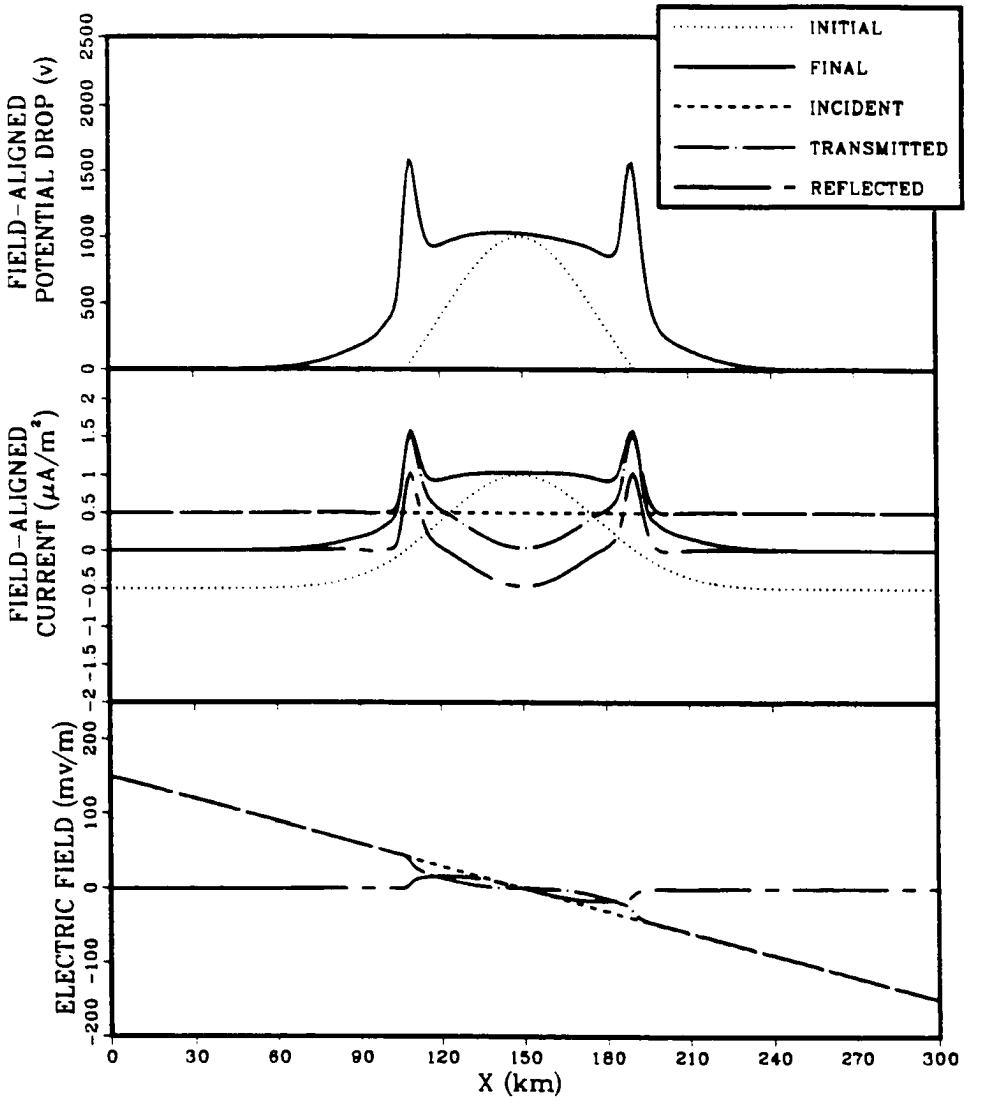

Fig. 5.3. Same as Figure 5.2 except the maximum potential drop of a double layer is 1 kV.

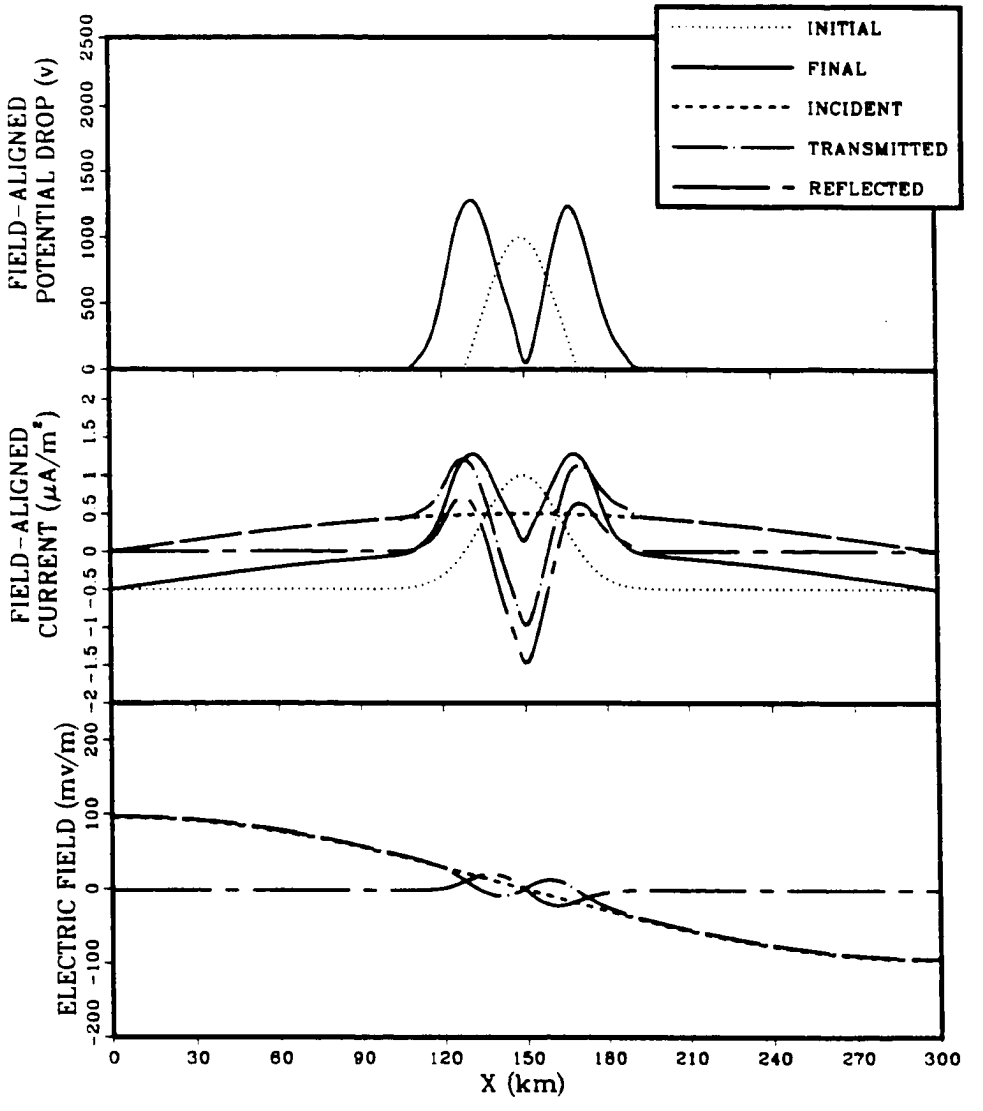

Fig. 5.4. The case for displaying the effects of perpendicular scale size of double layer, in which the ratio between the wave length of the incident Alfvén wave and the perpendicular scale size of double layer $\psi = 15$.

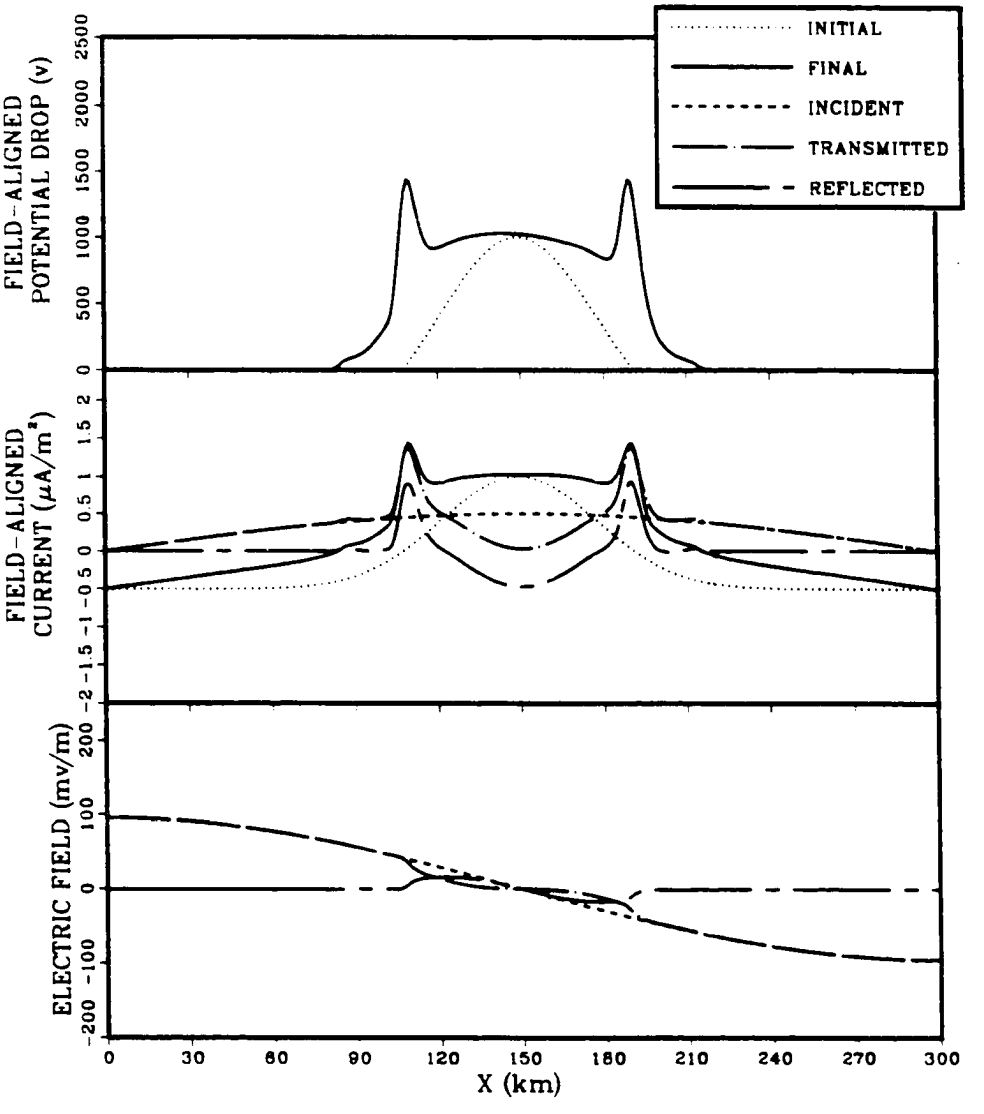

Fig. 5.5. Same as Figure 5.4 except $\psi = 8$.

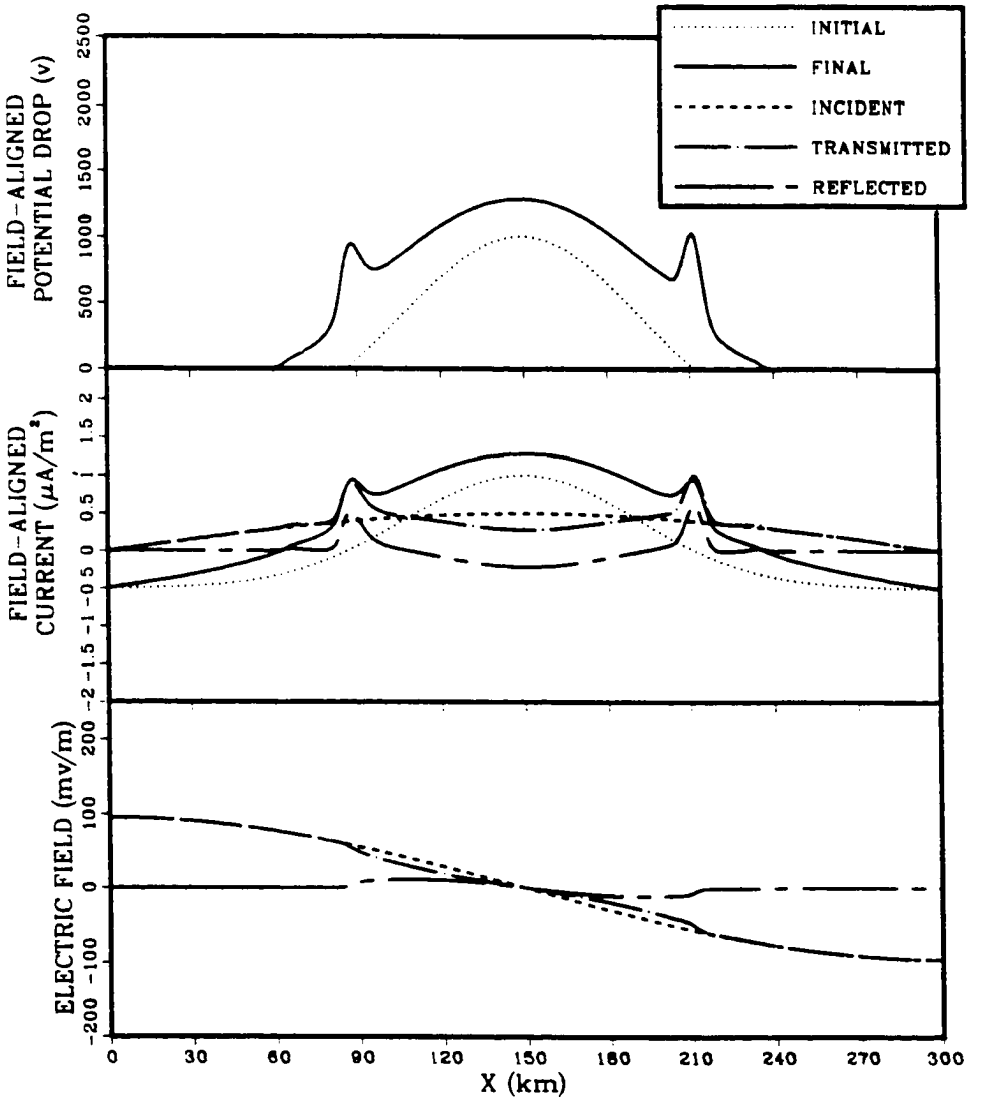

Fig. 5.6. Same as Figure 5.4 except $\psi = 4$.

layer potential drop are fixed, the amplitude of the reflected wave from the double layer should be also fixed. Since the perpendicular sizes of double layers in these cases are different, according to equation (5.4), with the reflected waves of the same amplitude, a double layer with a smaller perpendicular size must have a stronger downward field-aligned current carried by the reflected wave. An especially interesting feature shown in Figure 5.4 is that the downward current in the central part is so strong as to totally split the pre-existing double layer, leading to a twin double layer. In the present model, we have not included the magnetosphere and the ionosphere, therefore the interaction between an Alfvén wave and a double layer can only take place once. With the inclusion of the magnetosphere and the ionosphere, an Alfvén wave can bounce between the magnetosphere and the ionosphere, and so modify a double layer more than once. Then the resultant twin double layer probably can be further split into four or more double layers aligned parallel in north-south direction. Since the ionosphere can damp the reflected Alfvén wave, the twinning process will eventually cease and leave multiple double layers. It is commonly accepted that multiple discrete auroral arcs are caused by some instability along magnetic field lines. But our result suggests that multiple discrete auroral arcs can be due to the multiple interactions between Alfvén waves and a pre-existing single double layer.

5.4. Summary

The interaction between Alfvén waves and a 1-D localized double layer has been studied with the exclusion of the magnetosphere and the ionosphere. A

number of conclusions may be drawn from the numerical results of the model.

(1) The propagation of an incident Alfvén wave can be partially blocked by a nonresistive double layer potential, and splitting the wave into a reflected wave and a transmitted wave. There is no wave energy absorption during this process.

(2) The perpendicular electric field of the reflected wave is in the same direction as that of the incident wave. A direct result is that a double layer can decouple the magnetosphere from the ionospheric drag and lead to small scale intensified flow in the magnetospheric convection. For a given incident wave, increasing the strength of the double layer leads to a stronger reflected wave field and a weaker transmitted wave field, therefore causing a stronger decoupling between the magnetosphere and the ionosphere.

(3) The field-aligned currents carried by the reflected wave flow downward in the central part of a double layer while flowing upward on the edges within a small spatial range. The double layer is thereby suppressed in the central part and is enhanced on the both edges. The enhanced small scale potential drop on the edges of a double layer due to the intensified small scale upward field-aligned current can probably be used to explain the observed thin east-west aligned structures of discrete aurora.

(4) For a small perpendicular size double layer, the downward current carried by the reflected wave is so strong as to totally split the pre-existing double layer, leading to a twin double layer. Once the magnetosphere and the ionosphere are included, the Alfvén wave can be expected to bounce between the magnetosphere and the ionosphere, and modify a double layer more than once. The resulting twin double layer probably can be further split into four or more small scale double

layers. Such a twinning mechanism due to multiple interactions between Alfvén waves and double layers might be used to explain the origination of multiple discrete aurora.

As we said before, the present model is only a first step for studying the interactions between Alfvén waves and double layers. Further work needs to be done before we can obtain a complete physical understanding of this topic, specifically:

(1) Inclusion of the magnetosphere and the ionosphere into the interaction process, and studying the evolutionary behavior of Alfvén waves and a double layer while the Alfvén waves are bouncing around between the magnetosphere and the ionosphere. At this stage, the magnetosphere and the ionosphere are not necessarily involved in the dynamical processes.

(2) Building the interactions between Alfvén waves and a double layer into the global dynamical M-I coupling system, and studying the effects of such an interaction on the whole M-I coupling system.

(3) Using the results of present model as a basis, studying the behavior of the interactions between Alfvén waves and an extended double layer.

Chapter 6. Summary and Conclusions

The final link of the solar-terrestrial chain is the magnetosphere-ionosphere (M-I) coupling, which encompasses a complicated set of interacting physical processes occurring on vastly different temporal and spatial scales and has been a major focus of the space research. The basic idea of the M-I coupling can be traced back to the pioneering work of *Axford and Hines* [1961]. Recent quantitative developments of the M-I coupling model include the Rice convection model [*Harel et al.*, 1981; *Spiro et al.*, 1981; *Wolf et al.*, 1982], the local westward traveling surge (WTS) model [*Rothwell et al*, 1984], the MHD simulation model [*Watanabe et al.*, 1986], and the transient response model on the Alfvén wave traveling time scale [*Kan and Sun*, 1985; *Kan et al.*, 1988]. Due to the complexity of the M-I system, each proposed model can only emphasize certain aspects of the M-I coupling system and display part of the global features of the M-I coupling processes. The M-I coupling system is like a big puzzle, which can only be built up one piece at a time in a self-consistent way. The objective of this thesis is to add a few pieces to the puzzle and to gain a better understanding of the M-I coupling processes through numerical modeling.

A global M-I coupling model of substorms on the ionospheric recombination time scale is presented in chapter 2, which is the extension of the M-I coupling model of substorms on the Alfvén wave traveling time scale [*Kan et al.*, 1988]. The major contribution of the model is the inclusion of the finite ionospheric recombination time scale in the M-I coupling processes. The model results show that highly localized discrete auroral structures align along the poleward boundary

of the diffuse aurora in the evening-midnight sector. Such localized features were observed in the Viking imager data. In the model, the localized bright features of discrete aurora are produced by the positive feedback interactions between the field-aligned currents and the nonuniform and anisotropic ionospheric conductance associated with local recombination time scales. The results also show that the bright discrete auroral arc near midnight suddenly starts moving westward when the auroral brightness increases to a certain level. The moving discrete aurora has an initial velocity of around 2 km s^{-1} but gradually slows down and dims. This feature can be interpreted as the westward traveling surge. Following passage of the surge, several localized auroral arcs remain along the auroral oval, and the most active auroral region shifts from premidnight toward the evening sector. A mechanism is proposed to explain the motion of the westward traveling surge. Another interesting result from the M-I coupling model of substorms is that the polar cap potential Φ_{pc}, in response to the enhanced magnetospheric potential Φ_{mR} imposed by the reconnections on the dayside magnetopause, tends to saturate at large values of Φ_{mR}. The higher the diffuse auroral conductance, the lower the saturation level of the polar cap potential.

In chapter 3, the M-I coupling model presented in chapter 2 is extended to northward IMF conditions to study the effects of M-I coupling on high-latitude convection. Based on the model results, a mechanism for the origination of the distorted two-cell ionospheric convection is presented. We propose that four-cell convection patterns, imposed on the magnetosphere by the solar wind during a northward IMF, can be distorted into wrapped two-cell convection patterns which are similar to the empirical distorted two-cell convection patterns deduced

by Heppner and Maynard [1987]. The convection distortions are caused by the anisotropic reflections of Alfvén waves due to the existence of the anisotropic and nonuniform ionospheric conductance. The model results display the features of the theta aurora when the IMF is nearly northward. It is found that when B_y is positive, the downward region 1 current has an expansion towards the polar cap in the prenoon sector, and when B_y is negative, the upward region 1 current has an expansion towards the polar cap in the premidnight sector. The distributions of the resulting field-aligned currents in the model are consistent with the observed current distributions, including the NBZ currents, during northward IMF.

The role of the dayside dynamics in the global M-I coupling has not been well explored. One of the possible dynamic processes for transferring the energy and momentum of the solar wind to the magnetosphere through day side magnetopause is flux transfer events (FTEs). In chapter 4, the ionospheric and ground signatures of multiple field-aligned current sheets, which originated from dayside FTEs, are modeled in a local frame. The results show that the H component of magnetic perturbation associated with multiple field-aligned current sheets dominates the Z and D components. The H component of the FTE induced perturbation is highly localized and is confined to a region just under the multiple current sheets. The Z component of the perturbation is weaker and less confined compared with the H component. The magnetic perturbation of the D component associated with multiple field-aligned current sheets is probably too weak to be detectable, but it has some very fine structures which can reflect the characteristics of individual FTE flux tubes. The model results also show that when the upward current density is significantly greater than the downward current density in the FTE

current system, the negative Z component perturbation spreads over a much wider area than the positive Z component perturbation. On the other hand, when the downward current density is significantly greater than the upward current density in the FTE current system, the positive Z component perturbation spreads over a much wider ground area than the negative Z component perturbation. It is found that if the current density of multiple field-aligned current sheets is greater than 1.5 $\mu A/m^2$, with a longitudinal size of an individual current sheet being larger than 100 km and a latitudinal width being larger than 30 km, then the ground magnetic signature associated with multiple field-aligned current sheets probably could be identified from magnetometer records.

Finally, a study of the interactions between Alfvén waves and a localized double layer is conducted in chapter 5. The results show that the propagation of an incident Alfvén wave can be partially blocked by a nonresistive double layer potential, with the wave being split into a reflected wave and a transmitted wave. There is no wave energy absorption during such an interaction process. The perpendicular electric field of the reflected wave is in the same direction as the incident wave. A direct result from such a reflection is that double layer can decouple the magnetosphere from the ionospheric drag, and hence lead to small scale intensified flow in the magnetospheric convection pattern. For a given incident wave, increasing the strength of a double layer leading to a stronger reflected wave field and a weaker transmitted wave field, therefore leads to a stronger decoupling between the magnetosphere and the ionosphere. The results also show that the field-aligned currents carried by the reflected wave flow downward in the central part of a double layer while flowing upward on the edges. The double

layer is thereby suppressed in the central part and is enhanced on the edges. The enhanced small scale potential drop on the edges of a double layer due to an intensified small scale upward field-aligned current can probably be used to explain the observed thin east-west aligned structures of discrete aurora. An interesting thing is that for a small perpendicular size double layer, the downward current carried by the reflected wave is so strong as to totally split the pre-existing double layer, leading to a twin double layer. Once the magnetosphere and the ionosphere are included, an Alfvén wave can be expected to bounce between the magnetosphere and the ionosphere, and modify a double layer more than once. The resulting twin double layer probably can be further split into four or more small scale double layers. Such a twinning mechanism of double layers due to multiple interactions between Alfvén waves and double layers might be used to explain the origination of multiple discrete aurora. The work presented in chapter 5 can be used as a basis for building the interaction between Alfvén waves and field-aligned potential drops into a global M-I coupling model.

After decades of space research, it is clear that significant strides have been made in the global quantitative modeling of the magnetosphere-ionosphere coupling. However, due to the complexity of the subject, it is clear that much work remains before a complete understanding is achieved.

Appendix: Computing Code of the M-I Coupling Model of Substorms

```
c       ********************************************************
c         The following is a computing code of the M-I coupling
c       model of substorms on the ionospheric recombination
c       time scale.
c         The present version of the code was produced in June,
c       1989 and was documented in July 1990.
c       ********************************************************
c
c       ********************************************************
c       Computational grids:
c              The code uses polar coordinate to distribute
c              computational grids.  The grids are distributed
c              uniformly both in radial direction and in
c              azimuthal direction.  The radial dimension
c              measures the latitudes represented by variable I,
c              where I starts at 90 degree
c              and ends at 50 degree with total 41 points.
c              The azimuthal dimension measures the magnetic
c              local times represented by variable J, where
c              J starts at noon and increases in the counter-
c              clockwise direction with total 48 points.
c       ********************************************************
c
c       ********************************************************
c       Definitions:
c              SHO:  Background Hall conductance.
c              SPO:  Background Pedersen conductance.
c               SO:  Ionization source term during quiet time.
c              ERO:  Radial component of the electric field
c                    prio to the convection enhancement.
c             EFIO:  Azimuthal component of the electric field
c                    prio to the convection enhancement.
c              FEO:  Field-aligned current distribution prio
c                    to the convection enhancement.
c               FE:  Field-aligned current.
c              FEO:  Field-aligned current due to the
c                    divergence of the Hall currents.
```

```
c              FEP:  Field-aligned currents due to the
c                    divergence  of the Pedersen currents.
c               RI:  Radial component of horizontal currents.
c               FI:  Azimuthal component of horizontal currents.
c              RIH:  Radial component of Hall currents.
c              RIP:  Radial component of Pedersen currents.
c              FIH:  Azimuthal component of Hall currents.
c              FIP:  Azimuthal component of Pedersen currents.
c              AJE:  Joule dissipation rate.
c               ER:  Radial component of electric field.
c              EFI:  Azimuthal component of electric field.
c             DIVE:  Divergence of electric field.
c              PHP:  Electric potential at previous time step.
c              PHT:  Total electric potential.
c              PHI:  Electric potential associated with
c                    downward propagating waves.
c              PHR:  Electric potential associated with
c                    upward propagating waves.
c               SH:  Hall conductance.
c               SP:  Pedersen conductance.
c              DSH:  The change of Hall conductance between
c                    two successive time steps.
c              DSP:  The change of Pedersen conductance between
c                    two successive time steps.
c              SHP:  Hall conductance at previous time step.
c              SPP:  Pedersen conductance at previous time step.
c                R:  Ratio between the Hall conductance and
c                    the Pedersen conductance.
c               DR:  Radial spatial step.
c              DFI:  Azimuthal spatial step.
c               DT:  Time step.
c               LO:  Wave traveling time.
c               NO:  Total time steps in a specific run.
c                M:  Grid numbers in azimuthal direction.
c                N:  Grid numbers in radial direction.
c                H:  Effective height of the ionization due
c                    to the precipitating electrons.
c                E:  Electron charge.
c                B:  Background magnetic field.
c             GAMA:  Recombination coefficient.
c              FET:  Thermal electroc current.
c              FEC:  Equivalent saturation current.
c               QO:  Constant ionization coefficient.
c             PHIR:  Array which contains traveling wave field.
c               RM:  Magnetospheric reflection coefficient.
```

```
c
c       ********************************************************
c       Define the dimensions of all arrays.
c        ********************************************************
        COMMON /PRE/SHO(41,48),SPO(41,48),PHO(41,48),SO(41,48),
     1  ERO(41,48),EFIO(41,48),FEO(41,48)
        COMMON /CURR/FE(41,48),FEH(41,48),FEP(41,48),RI(41,48),
     1  FI(41,48),RIH(41,48),RIP(41,48),FIH(41,48),FIP(41,48),
     1  AJE(41,48),TFE,FEM
        COMMON /FIELD/ER(41,48),EFI(41,48),DIVE(41,48)
        COMMON /PH/PHP(41,48),PHT(41,48),PHI(41,48),PHR(41,48)
        COMMON /COD/SH(41,48),SP(41,48),DSH(41,48),DSP(41,48),
     1  SHP(41,48),SPP(41,48)
        COMMON /PARA/R,DR,DFI,DFI2,DT,LO,NO,M,N,H,E,B,BETA,
     1  CBETA,GAMA,FET,FEC,QO
        COMMON /PARA1/L1,L2,L3,L4,L5,L6,L7,L8,L9
        COMMON /DELA/PHIR(41,48,60),RM(41,48)
c       ********************************************************
c       Specify constant parameters
c       ********************************************************
        M=48
        N=41
        DFI=1.308E-1
        DFI2=DFI*DFI
        DR=1.1311E5
        R=1.5E0
        H=7.E3
        B=0.5E-4
        BETA=0.9E-13
        E=1.6022E-19
        CBETA=(BETA*B)/(E*H)
        GAMA=1.E4
        FET=0.08E-6
        FEC=0.8E-6
        QO=7.E-3
c       ******************************************************
c       Input time step, traveling time and total time steps
c       of the run.
c       ******************************************************
        WRITE(*,11)
11        FORMAT(5X,'PLEASE INPUT DT,LO,NO,N1')
        READ(*,14) DT,LO,NO
c       ******************************************************
c       Input specific times at which you need output.
c       ******************************************************
```

```
      WRITE(*,31)
31      FORMAT(5X,'PLEASE INPUT specific times')
      READ(*,32) L1,L2,L3,L4,L5,L6,L7,L8,L9
32      FORMAT(9I10)
14      FORMAT(F12.5,2I10)
c      ******************************************************
c      Input the initial conditions of the model.
c      ******************************************************
      READ(13,12)((SHO(I,J),J=1,48),I=1,41)
      READ(15,12)((PHO(I,J),J=1,48),I=1,41)
      READ(18,12)((PHI(I,J),J=1,48),I=1,41)
      READ(19,12)((RM(I,J),J=1,48),I=1,41)
12      FORMAT(6E18.5)
13      FORMAT(2E18.5)
15      FORMAT(E18.5)
c      ******************************************************
c      Calculate other quantities from the initials.
c      ******************************************************
      CALL PRE
c      ******************************************************
c      Start to calculate the temporal evolution of the
c      M-I coupling processes
c      ******************************************************
      DO 20 K=1,NO
c      ******************************************************
c      Calculate the wave reflection in the ionosphere.
c      ******************************************************
      CALL IREFLEC(K)
c      ******************************************************
c      calculate the field-aligned current and the
c      horizontal current by using total electric field
c      and the conductance.
c      ******************************************************
      CALL CURR(K)
c      ******************************************************
c      Write the outputs at specific times.
c      ******************************************************
      IF(K.EQ.L1.OR.K.EQ.L2.OR.K.EQ.L3.OR.K.EQ.L4.OR.
     1  K.EQ.L5.OR.K.EQ.L6.OR.K.EQ.L7.OR.K.EQ.L8.OR.K.EQ.L9) THEN
      WRITE(31,12)((PHT(I,J),J=1,48),I=1,41)
      WRITE(41,12)((SH(I,J),J=1,48),I=1,41)
      WRITE(51,12)((FE(I,J),J=1,48),I=1,41)
      WRITE(61,13)((FI(I,J),RI(I,J),I=1,41),J=1,48)
      WRITE(71,12)((AJE(I,J),J=1,48),I=1,41)
      WRITE(81,12)((DIVE(I,J),J=1,48),I=1,41)
```

```
        ELSE
        R=R
        END IF
c        ******************************************************
c        Calculate the enhancement of the ionospheric
c        conductance.
c        ******************************************************
        CALL CONDUC(K)
c        ******************************************************
c        Handle the wave traveling between magnetosphere
c        and the ionosphere.
c        ******************************************************
        CALL DELAY
c        ******************************************************
c        reset the reflected wave.
c        ******************************************************
        DO 21 I=1,N
        DO 21 J=1,M
        PHR(I,J)=0.
21        CONTINUE
20        CONTINUE
        STOP
        END
C
C
C************************************************************
        SUBROUTINE PRE
C************************************************************
c        This subroutine calculate other initial quantities
c        from the given initial conditions.
c        ******************************************************
        COMMON /PRE/SHO(41,48),SPO(41,48),PHO(41,48),SO(41,48),
     1  ERO(41,48),EFIO(41,48),FEO(41,48)
        COMMON /CURR/FE(41,48),FEH(41,48),FEP(41,48),RI(41,48),
     1  FI(41,48),RIH(41,48),RIP(41,48),FIH(41,48),FIP(41,48),
     1  AJE(41,48)
        COMMON /FIELD/ER(41,48),EFI(41,48),DIVE(41,48)
        COMMON /PH/PHP(41,48),PHT(41,48),PHI(41,48),PHR(41,48)
        COMMON /COD/SH(41,48),SP(41,48),DSH(41,48),DSP(41,48),
     1  SHP(41,48),SPP(41,48)
        COMMON /PARA/R,DR,DFI,DFI2,DT,LO,NO,M,N,H,E,B,BETA,
     1  CBETA,GAMA,FET,FEC,QO
        COMMON /DELA/PHIR(41,48,60),RM(41,48)
C        ******************************************************
C        CALCULATE SPO,PHP,SH,SP,DSH,DSP
```

```
c        ************************************************
         DO 101 I=1,N
         DO 101 J=1,M
         SPO(I,J)=SHO(I,J)/R
         PHP(I,J)=PHO(I,J)
         SH(I,J)=SHO(I,J)
         SP(I,J)=SPO(I,J)
         DSH(I,J)=0.
         DSP(I,J)=0.
101         CONTINUE
c        ************************************************
C        CALCULATE ERO,EFIO,SO
c        ************************************************
         DO 102 J=1,M
         J1=J+1
         J2=J-1
         IF(J.EQ.1) J2=M
         IF(J.EQ.M) J1=1
         ERO(1,J)=1000.*(PHO(2,J)-PHO(1,J))/DR
         EFIO(1,J)=0.
         ERO(N,J)=1000.*(PHO(N,J)-PHO(N-1,J))/DR
         EFIO(N,J)=1000.*0.5*(PHO(N,J1)-PHO(N,J2))/(DR*(N-1)*DFI)
         DO 103 I=2,N-1
         U=FLOAT(I-1)
         ERO(I,J)=1000.*0.5*(PHO(I+1,J)-PHO(I-1,J))/DR
         EFIO(I,J)=1000.*0.5*(PHO(I,J1)-PHO(I,J2))/(U*DR*DFI)
         SO(I,J)=(0.5*(SHO(I,J1)-SHO(I,J2))/(U*DR*DFI)*ERO(I,J)
     1   -0.5*(SHO(I+1,J)-SHO(I-1,J))/DR*EFIO(I,J))/B
     1   +CBETA*SHO(I,J)**2
103         CONTINUE
         SO(1,J)=SO(2,J)
         SO(N,J)=SO(N-1,J)
102         CONTINUE
C        ************************************************
C        CALCULATE FEO
c        ************************************************
         DO 104 J=1,M
         J1=J+1
         J2=J-1
         IF(J.EQ.1) J2=M
         IF(J.EQ.M) J1=1
         DO 105 I=2,N-1
         U=FLOAT(I-1)
         U2=U*U
         I1=I+1
```

```
      I2=I-1
      A2=1./R/(2.*DR)*(ERO(I,J)+R*EFIO(I,J))*(SHO(I1,J)-
     1       SHO(I2,J))
      A3=1./R/(2.*DFI*U*DR)*(EFIO(I,J)-R*ERO(I,J))*
     1  (SHO(I,J1)-SHO(I,J2))
      A4=1./R*((ERO(I1,J)-ERO(I2,J))/(2.*DR)+(EFIO(I,J1)
     1  -EFIO(I,J2))/(2.*DFI*U*DR)+ERO(I,J)/(U*DR))*SHO(I,J)
      FEO(I,J)=-(A2+A3+A4)
105      CONTINUE
      FEO(41,J)=FEO(40,J)
      FEO(1,J)=FEO(2,J)
104      CONTINUE
c       ***********************************************
C       GIVE 0.  VALUE TO PHIR,PHR
c       ***********************************************
      DO 106 L=1,LO
      DO 106 I=1,N
      DO 106 J=1,M
      PHIR(I,J,L)=0.
106      CONTINUE
      DO 107 I=1,N
      DO 107 J=1,M
      PHR(I,J)=0.
107      CONTINUE
C
      RETURN
      END
C*************************************************************
      SUBROUTINE IREFLEC(K)
C*************************************************************
c       This subroutine calculate the wave reflection
c       in the ionosphere.
c       ***************************************************
      COMMON /PRE/SHO(41,48),SPO(41,48),PHO(41,48),SO(41,48),
     1  ERO(41,48),EFIO(41,48),FEO(41,48)
      COMMON /CURR/FE(41,48),FEH(41,48),FEP(41,48),RI(41,48),
     1  FI(41,48),RIH(41,48),RIP(41,48),FIH(41,48),FIP(41,48),
     1  AJE(41,48)
      COMMON /FIELD/ER(41,48),EFI(41,48),DIVE(41,48)
      COMMON /PH/PHP(41,48),PHT(41,48),PHI(41,48),PHR(41,48)
      COMMON /COD/SH(41,48),SP(41,48),DSH(41,48),DSP(41,48),
     1  SHP(41,48),SPP(41,48)
      COMMON /PARA/R,DR,DFI,DFI2,DT,LO,NO,M,N,H,E,B,BETA,
     1  CBETA,GAMA,FET,FEC,QO
      COMMON /PARA1/L1,L2,L3,L4,L5,L6,L7,L8,L9
```

```
      COMMON /DELA/PHIR(41,48,60),RM(41,48)
      DIMENSION BO(41,48),B2(41,48),B3(41,48),B5(41,48),
     1  B4(41,48),B6(41,48),PREF(41,48)
      SA=0.5
      ERR=0.1
      DO 102 J=1,M
      J1=J+1
      J2=J-1
      IF(J.EQ.1) J2=M
      IF(J.EQ.M) J1=1
      DO 103 I=2,N-1
      U=FLOAT(I-1)
      U2=U*U
      I1=I+1
      I2=I-1
      BO(I,J)=4.*(DFI2+1./U2)
      B1=2.*DFI2
      B2(I,J)=DFI2/(SA+SP(I,J))*((SA+SP(I,J))/U+(0.5*(SP(I1,J)-
     1  SP(I2,J))-1./U*(SH(I,J1)-SH(I,J2))/DFI*0.5))
      B3(I,J)=DFI/((SA+SP(I,J))*U)*(0.5*(SH(I1,J)-SH(I2,J))+
     1  0.5/(U*DFI)*(SP(I,J1)-SP(I,J2)))
      B4(I,J)=2./U2
      B5(I,J)=-2.*DFI2/(SA+SP(I,J))*((SA-SP(I,J))*(PHI(I1,J)-
     1  2.*PHI(I,J)+PHI(I2,J))
     1  +((SA-SP(I,J))/U-(0.5*(SP(I1,J)-SP(I2,J))-0.5/(U*DFI)*
     1  (SH(I,J1)-SH(I,J2))))*0.5*(PHI(I1,J)-PHI(I2,J))
     1  -1./U*(0.5*(SH(I1,J)-SH(I2,J))+0.5/(U*DFI)*
     1  (SP(I,J1)-SP(I,J2)))*0.5/DFI*(PHI(I,J1)-PHI(I,J2))+
     1  (SA-SP(I,J))/(U2*DFI2)*(PHI(I,J1)-2.*PHI(I,J)+PHI(I,J2)))
      B6(I,J)=-2.*DFI2/(SA+SP(I,J))*((-DSP(I,J))*(PHP(I1,J)-
     1  2.*PHP(I,J)+PHP(I2,J))
     1  +((-DSP(I,J))/U-(0.5*(DSP(I1,J)-DSP(I2,J))-0.5/(U*DFI)*
     1  (DSH(I,J1)-DSH(I,J2))))*0.5*(PHP(I1,J)-PHP(I2,J))
     1  -1./U*(0.5*(DSH(I1,J)-DSH(I2,J))+0.5/(U*DFI)*
     1  (DSP(I,J1)-DSP(I,J2)))*0.5/DFI*(PHP(I,J1)-PHP(I,J2))+
     1  (-DSP(I,J))/(U2*DFI2)*(PHP(I,J1)-2.*PHP(I,J)+PHP(I,J2)))
103      CONTINUE
102      CONTINUE
      DO 101 L=1,2000
      ERR2=0.
      PREFM=0.
      DO 108 J=1,M
      J1=J+1
      J2=J-1
      IF(J.EQ.1) J2=M
```

```
      IF(J.EQ.M) J1=1
      DO 109 I=2,N-1
      I1=I+1
      I2=I-1
      PREF(I,J)=1./BO(I,J)*((B1+B2(I,J))*PHR(I1,J)+
     1 (B1-B2(I,J))*PHR(I2,J)+
     1 (B3(I,J)+B4(I,J))*PHR(I,J1)+(B4(I,J)-B3(I,J))*PHR(I,J2)
     1 +B5(I,J)+B6(I,J))
      ERR1=ABS(PREF(I,J)-PHR(I,J))
      PREFS=ABS(PREF(I,J))
      IF(ERR1.GT.ERR2) ERR2=ERR1
      IF(PREFS.GT.PREFM) THEN
      PREFM=PREFS
      B6M=ABS(B6(I,J)/BO(I,J))
      B5M=ABS(B5(I,J)/BO(I,J))
      ELSE
      R=R
      END IF
      PHR(I,J)=PREF(I,J)
109      CONTINUE
108      CONTINUE
101      IF(ERR2.LE.ERR) GOTO 104
      IF(L.GT.1999) STOP 'SOLUTION DOES NOT CONVERGE'
104   IF(K.EQ.L1.OR.K.EQ.L2.OR.K.EQ.L3.OR.K.EQ.L4.OR.K.EQ.L5.OR.
     1 K.EQ.L6.OR.K.EQ.L7.OR.K.EQ.L8.OR.K.EQ.L9) THEN
      PRINT *,'PREFM=',PREFM,' B6M=',B6M,' B5M=',B5M
      ELSE
      R=R
      END IF
155      DO 105 I=1,N
      DO 105 J=1,M
      PHT(I,J)=PHI(I,J)+PHR(I,J)+PHP(I,J)
      PHP(I,J)=PHT(I,J)
105      CONTINUE
c      ************************************************
c      Calculate electric field
c      ************************************************
      DO 110 J=1,M
      J1=J+1
      J2=J-1
      IF(J.EQ.1) J2=M
      IF(J.EQ.M) J1=1
      ER(1,J)=1000.*(PHT(2,J)-PHT(1,J))/DR
      EFI(1,J)=0.
      ER(N,J)=1000.*(PHT(N,J)-PHT(N-1,J))/DR
```

```
      EFI(N,J)=1000.*0.5*(PHT(N,J1)-PHT(N,J2))/(DR*(N-1)*DFI)
      DO 106 I=2,N-1
      U=FLOAT(I-1)
      ER(I,J)=1000.*0.5*(PHT(I+1,J)-PHT(I-1,J))/DR
      EFI(I,J)=1000.*0.5*(PHT(I,J1)-PHT(I,J2))/(U*DR*DFI)
106      CONTINUE
110      CONTINUE
c        ***********************************************
c        calculate the divergence of electric field
c        ***********************************************
      DO 111 J=1,M
      J1=J+1
      J2=J-1
      IF(J.EQ.1) J2=M
      IF(J.EQ.M) J1=1
      DIVE(1,J)=0.
      DIVE(N,J)=-((ER(N,J)-ER(N-1,J))/DR+ER(N,J)/((N-1)*DR)
     1 +0.5*(EFI(N,J1)-EFI(N,J2))/(DR*(N-1)*DFI))
      DO 107 I=2,N-1
      U=FLOAT(I-1)
      DIVE(I,J)=-(0.5*(ER(I+1,J)-ER(I-1,J))/DR+ER(I,J)/(U*DR)
     1 +0.5*(EFI(I,J1)-EFI(I,J2))/(U*DR*DFI))
107       CONTINUE
111      CONTIHUE
      RETURN
      END
C
C
C*******************************************************
      SUBROUTINE CURR(K)
C*******************************************************
C        This subroutine calculate field-aligned current
c        and the horizontal currents.
c        ***********************************************
      COMMON /PRE/SHO(41,48),SPO(41,48),PHO(41,48),SO(41,48),
     1 ERO(41,48),EFIO(41,48),FEO(41,48)
      COMMON /CURR/FE(41,48),FEH(41,48),FEP(41,48),RI(41,48),
     1 FI(41,48),RIH(41,48),RIP(41,48),FIH(41,48),FIP(41,48),
     1 AJE(41,48),TFE,FEM
      COMMON /FIELD/ER(41,48),EFI(41,48),DIVE(41,48)
      COMMON /PH/PHP(41,48),PHT(41,48),PHI(41,48),PHR(41,48)
      COMMON /COD/SH(41,48),SP(41,48),DSH(41,48),DSP(41,48),
     1 SHP(41,48),SPP(41,48)
      COMMOH /PARA/R,DR,DFI,DFI2,DT,LO,NO,M,N,H,E,B,BETA,
     1 CBETA,GAMA,FET,FEC,QO
```

```
      COMMON /DELA/PHIR(41,48,60),RM(41,48)
      DO 201 J=1,M
      J1=J+1
      J2=J-1
      IF(J.EQ.1) J2=M
      IF(J.EQ.M) J1=1
      DO 202 I=2,N-1
      U=FLOAT(I-1)
      U2=U*U
      I1=I+1
      I2=I-1
      A2=1./R/(2.*DR)*(ER(I,J)+R*EFI(I,J))*(SH(I1,J)-
     1       SH(I2,J))
      A3=1./R/(2.*DFI*U*DR)*(EFI(I,J)-R*ER(I,J))*
     1 (SH(I,J1)-SH(I,J2))
      A4=1./R*((ER(I1,J)-ER(I2,J))/(2.*DR)+(EFI(I,J1)
     1 -EFI(I,J2))/(2.*DFI*U*DR)+ER(I,J)/(U*DR))*SH(I,J)
      FE(I,J)=-(A2+A3+A4)
      A2H=EFI(I,J)*(SH(I1,J)-SH(I2,J))/(2.*DR)
      A3H=-ER(I,J)*(SH(I,J1)-SH(I,J2))/(2.*DFI*U*DR)
      FEH(I,J)=-(A2H+A3H)
      FEP(I,J)=FE(I,J)-FEH(I,J)
202      CONTINUE
      FE(41,J)=FE(40,J)
      FE(1,J)=FE(2,J)
      FEH(41,J)=FEH(40,J)
      FEH(1,J)=FEH(2,J)
      FEP(41,J)=FEP(40,J)
      FEP(1,J)=FEP(2,J)
201      CONTINUE
c      ***********************************************
c      Calculate horizontal current and Joule
c      dissipation rate.
c      ***********************************************
      DO 203 J=1,M
      DO 203 I=1,N
C      RI(I,J)=SH(I,J)*(ER(I,J)/R+EFI(I,J))
C      FI(I,J)=SH(I,J)*(EFI(I,J)/R-ER(I,J))
      RIP(I,J)=SH(I,J)*ER(I,J)/R
      RIH(I,J)=SH(I,J)*EFI(I,J)
      RI(I,J)=RIH(I,J)+RIP(I,J)
      FIP(I,J)=SH(I,J)*EFI(I,J)/R
      FIH(I,J)=-SH(I,J)*ER(I,J)
      FI(I,J)=FIP(I,J)+FIH(I,J)
      AJE(I,J)=RI(I,J)*ER(I,J)+FI(I,J)*EFI(I,J)
```

```
203        CONTINUE
        TFE=0.
        DO 204 I=1,N
        DO 204 J=1,M
        IF (FE(I,J).LT.0..AND.J.LE.30
     1  .AND.I.LE.26.AND.I.GT.8) THEN
        TFE=TFE+ABS(FE(I,J))*FLOAT(I-1)*DR*DFI*DR
        ELSE
        R=R
        END IF
204        CONTINUE
        FEM=0.
        DO 205 I=1,N
        DO 205 J=1,M
        IF (FE(I,J).LT.0.)  THEN
        IF (ABS(FE(I,J)).GT.FEM) THEN
        FEM=ABS(FE(I,J))
        ELSE
        FEM=FEM
        END IF
        ELSE
        R=R
        END IF
205        CONTINUE
        RETURN
        END
C
C*********************************************************
        SUBROUTINE CONDUC(K)
C*********************************************************
C        This subroutine calculate the conductance
        enhancement in the ionosphere.
c        ************************************************
        COMMON /PRE/SHO(41,48),SPO(41,48),PHO(41,48),SO(41,48),
     1  ERO(41,48),EFIO(41,48),FEO(41,48)
        COMMON /CURR/FE(41,48),FEH(41,48),FEP(41,48),RI(41,48),
     1  FI(41,48),RIH(41,48),RIP(41,48),FIH(41,48),FIP(41,48),
     1  AJE(41,48)
        COMMON /FIELD/ER(41,48),EFI(41,48),DIVE(41,48)
        COMMON /PH/PHP(41,48),PHT(41,48),PHI(41,48),PHR(41,48)
        COMMON /COD/SH(41,48),SP(41,48),DSH(41,48),DSP(41,48),
     1  SHP(41,48),SPP(41,48)
        COMMON /PARA/R,DR,DFI,DFI2,DT,LO,NO,M,N,H,E,B,BETA,
     1  CBETA,GAMA,FET,FEC,QO
        COMMON /PARA1/L1,L2,L3,L4,L5,L6,L7,L8,L9
```

```
      COMMON /DELA/PHIR(41,48,60),RM(41,48)
      DIMENSION D1(41,48),D2(41,48),D3(41,48),D4(41,48)
      DO 401 I=1,N
      DO 401 J=1,M
      SHP(I,J)=SH(I,J)
      SPP(I,J)=SP(I,J)
401      CONTINUE
      DO 402 J=1,M
      J1=J+1
      J2=J-1
      IF(J.EQ.1) J2=M
      IF(J.EQ.M) J1=1
      DO 403 I=2,N-1
      U=FLOAT(I-1)
      U2=U*U
      I1=I+1
      I2=I-1
       FETN=-FET
      IF(FE(I,J).GT.FETN) THEN
      Q=0.
      ELSE
      IF(I.LE.15) THEN
      Q=0.3E4*ABS(FE(I,J))
      ELSE
      IF(DIVE(I,J).GE.0.)  THEN
      Q=QO
      ELSE
      AFE=ABS(FE(I,J))
      IF(AFE.GE.FEC) THEN
      Q=GAMA*(FEC-FET)
      ELSE
      Q=GAMA*(ABS(FE(I,J))-FET)
      END IF
      END IF
      END IF
      END IF
      CQ=Q*H/B
      D1(I,J)=CQ*ABS(FE(I,J))
           D2(I,J)=SO(I,J)
      D3(I,J)=-CBETA*SHP(I,J)**2
           D4(I,J)=-(0.5*(SHP(I,J1)-SHP(I,J2))/(U*DR*DFI)*ER(I,J)
     1  -0.5*(SHP(I+1,J)-SHP(I-1,J))/DR*EFI(I,J))/B
      SH(I,J)=SHP(I,J)
     1  +DT*(D1(I,J)+D2(I,J)+D3(I,J)+D4(I,J))
 403      CONTINUE
```

```
      SH(N,J)=SH(N-1,J)
      SH(1,J)=SH(2,J)
      D1(1,J)=D1(2,J)
      D2(1,J)=D2(2,J)
      D3(1,J)=D3(2,J)
      D4(1,J)=D4(2,J)
402      CONTINUE
      SHM=0.
      DSHM=0.
      KI=0
      KJ=0
c      ********************************************
c      Calculate the change of conductance between
c      two time steps.
c      ********************************************
      DO 404 I=1,N
      DO 404 J=1,M
      SP(I,J)=SH(I,J)/R
      DSH(I,J)=SH(I,J)-SHP(I,J)
      DSP(I,J)=SP(I,J)-SPP(I,J)
      DSHS=ABS(DSH(I,J))
      IF(SH(I,J).GT.SHM) SHM=SH(I,J)
      IF(DSHS.GT.DSHM) THEN
      DSHM=DSH(I,J)
      D1M=D1(I,J)
      D2M=D2(I,J)
      D3M=D3(I,J)
      D4M=D4(I,J)
      KI=I
      KJ=J
      ELSE
      R=R
      END IF
404      CONTINUE
      IF(K.EQ.L1.OR.K.EQ.L2.OR.K.EQ.L3.OR.K.EQ.L4.OR.K.EQ.L5.OR.
     1  K.EQ.L6.OR.K.EQ.L7.OR.K.EQ.L8.OR.K.EQ.L9) THEN
      PRINT *,'SHM=',SHM,'DSHM=',DSHM,'I=',KI,'J=',KJ
      PRINT *,'D1M=',D1M,' D2M=',D2M,' D3M=',D3M,' D4M=',D4M
      PRINT *,'    '
      ELSE
      R=R
      END IF
455      RETURN
      END
C
```

```
C
C*************************************************
      SUBROUTINE DELAY(K)
C*************************************************
c       This subroutine handle the wave traveling
c       between the magnetosphere and the ionosphere.
c       ******************************************
      COMMON /PRE/SHO(41,48),SPO(41,48),PHO(41,48),SO(41,48),
     1 ERO(41,48),EFIO(41,48),FEO(41,48)
      COMMON /CURR/FE(41,48),FEH(41,48),FEP(41,48),RI(41,48),
     1 FI(41,48),RIH(41,48),RIP(41,48),FIH(41,48),FIP(41,48),
     1 AJE(41,48)
      COMMON /FIELD/ER(41,48),EFI(41,48),DIVE(41,48)
      COMMON /PH/PHP(41,48),PHT(41,48),PHI(41,48),PHR(41,48)
      COMMON /COD/SH(41,48),SP(41,48),DSH(41,48),DSP(41,48),
     1 SHP(41,48),SPP(41,48)
      COMMON /PARA/R,DR,DFI,DFI2,DT,LO,NO,M,N,H,E,B,BETA,
     1 CBETA,GAMA,FET,FEC,QO
      COMMON /DELA/PHIR(41,48,60),RM(41,48)
      DO 501 I=1,N
      DO 501 J=1,M
      PHIR(I,J,LO+1)=PHR(I,J)*RM(I,J)
501       CONTINUE
      DO 502 L=1,LO
      DO 502 I=1,N
      DO 502 J=1,M
      PHIR(I,J,L)=PHIR(I,J,L+1)
502      CONTINUE
      DO 503 I=1,N
      DO 503 J=1,M
      PHI(I,J)=PHIR(I,J,1)
503      CONTINUE
      RETURN
      END
C
C
c       All quantities in this code are in MKS unit.
```

References

Ahn, B.-H., S.-I. Akasofu, Y. Kamide, and J. H. King, Cross-polar cap potential drop and the energy coupling function, *J. Geophys. Res.*, *89*, 11,028, 1984.

Akasofu, S.-I., The development of the auroral substorm, *Planet. Space Sci.*, *12*, 273, 1964.

Akasofu, S.-I., *Polar and Magnetospheric Substorms*, D. Reidel, Hingham, Mass., 1968.

Atkinson, G., An approximate flow equation for magnetic flux tubes and its application to polar substorms. *J. Geophys. Res.*, *72*, 5373, 1967.

Anger, C. D., S. K. Babey, A. L. Broadfoot, R. G. Brown, L. L. Cogger, R. Gattinger, J. W. Haslett, R. A. King, D. J. McEwen, J. S. Murphree, E. H. Richardson, B. R. Sandel, K. Smith, and A. Vallance Jones, An ultraviolet auroral imager for the Viking spacecraft, *Geophys. Res. Lett.*, *14*, 387, 1987.

Axford, W. I., and C. O. Hines, A unifying theory of high-latitude geophysical phenomena and geomagnetic storms, *Can. J. Phys.*, *39*, 1433, 1961.

Axford, W. I., Magnetospheric convection, *Rev. Geophys.*, *7*, 421, 1969.

Baker, D. N., S.-I. Akasofu, W. Baumjohann, J. W. Bieber, D. H. Fairfield, E. W. Jr. Hones, B. Mauk, R. L. McPherron, and T. E. Moore, Substorms in the magnetosphere, in*Solar Terrestrial Physics: Present and Future*, edited by D. M. Butler and K. Papadopoulos, NASA reference publication 1120, 1984.

Baker, D. N., R. C. Anderson, R. D. Zwickl, and J. A. Slavin, Average plasma and magnetic field variations in the distant magnetotail associated with near-Earth substorm effects, *J. Geophys. Res.*, *92*, 71, 1987.

Baumjohann, W., The plasma sheet boundary layer and magnetospheric substorms, *J. Geomagn. Geoelec.*, *40*, 157, 1988.

Baumjohann, W., G. Paschmann, and C. A. Cattell, Average plasma properties in the central plasma sheet, *J. Geophys. Res.*, *94*, 6597, 1989.

Burch, J. L., P. H. Reiff, J. D. Menietti, R. A. Heelis, W. B. Hanson, S. D. Shawhan, E. G. Shelley, M. Sugiura, D. R. Weimer, and J. D. Winningham, IMF B_y-dependent plasma flow and Birkeland currents in the dayside magnetosphere, 1, Dynamics Explorer observations, *J. Geophys. Res.*, *90*, 1577, 1985.

Burke, W. J., M. C. Kelley, R. C. Sagalyn, M. Smiddy, and S. T. Lai, Polar cap electric field structures with a northward interplanetary magnetic field, *Geophys. Res. Lett.*, *6*, 21, 1979.

Campbell, W. H., Electrical properties of the earth's mantle, Birkhauser, Basel, Boston, 1987.

Cattell, C. A., M. Kim, R. P. Lin, and F. S. Mozer, Observations of large electric fields near the plasma sheet boundary by ISEE 1, *Geophys. Res. Lett.*, *5*, 539, 1982.

Chapman, S., The solar and lunar diurnal variations of terrestrial magnetism, Phil. Trans. R. Soc., 1, 218A, 1919.

Chiu, Y. T., R. Anderson, J. Fennell, L. Frank, R. Hoffman, M. Hudson, L. Lyons, P. Palmadesso, E. Ungstrup, R. Vondrak, D. Williams, and R. Wolf, Connection between the magnetosphere and ionosphere, in*Solar Terrestrial Physics: Present and Future*, edited by D. M. Butler and K. Papadopoulos, NASA reference publication 1120, 1984.

Coroniti, F. V., and C. F. Kennel, Can the ionosphere regulate magnetospheric convection?, *J. Geophys. Res.*, *78*, 2837, 1973.

Crooker, N. U., Mapping the merging potential from the magnetopause to the ionosphere through the dayside cusp, *J. Geophys. Res.*, *93*, 7338, 1988.

Craven, J. D., L. A. Frank, and S.-I. Akasofu, Propagation of a westward traveling surge and the development of persistent auroral features, *J. Geophys. Res.*, *94*, 6961, 1989.

Cummings, W. D., and P. J. Coleman, Jr., Simultaneous magnetic field variations

at the earth's surface and at synchronous, equatorial distance, 1, Bay associated events, *Radio Sci., 3,* 758, 1968.

Davis, T. N., Observed characteristics of auroral form, *Space Sci. Rev., 22,* 77, 1978.

Deforest, S. E., and C. E. McIlwain, Plasma clouds in the magnetosphere, *J. Geophys. Res., 76,* 3587, 1971.

Doyle, M. A., and W. J. Burke, S3-2 measurements of the polar cap potential, *J. Geophys. Res., 88,* 9125, 1983.

Frank, L. A., and K. L. Ackerson, Observations of charged particle precipitation into the auroral zone, *J. Geophys. Res., 76,* 3612, 1971.

Fridman, M., and J. Lemaire, Relationship between auroral electron fluxes and field-aligned electric potential difference, *J. Geophys. Res., 85,* 664, 1980.

Fukushima, N., Equivalence in ground geomagnetic effect of Chapman-Vestine's and Birkland-Alfven's electric current-systems for polar magnetic storms, *Rep. Ionos. Space Res. Jpn., 23(3),* 1969.

Goertz, C. K., and R. W. Boswell, Magnetosphere-ionosphere coupling, *J. Geophys. Res., 84,* 7239, 1979.

Goertz, C. K., E. Nielsen, A. Korth, K. H. Glassmeier, C. Haldoupis, P. Hoeg, and D. Hayward, Observations of a possible ground signature of flux transfer events, *J. Geophys. Res., 90,* 4069, 1985.

Goertz, C. K., and R. A. Smith, Thermal catastrophe model of substorms, *J. Geophys. Res., 94,* 6581, 1989.

Harel, M., R. A. Wolf, P. H. Reiff, R. W. Spiro, W. J. Burke, F. J. Rich, and M. Smiddy, Quantitative simulation of a magnetospheric substorm, 1, Model logic and overview, *J. Geophys. Res., 86,* 2217, 1981.

Heppner, J. P., Electric field variations during substorms: OGO-6 measurements, *Planet. Space Sci., 20,* 1475, 1972.

Heppner, J. P., Empirical models of high latitude electric field, *J. Geophys. Res.,*

82, 1115, 1977.

Heppner, J. P. and N. C. Maynard, Empirical high-latitude electric field models, *J. Geophys. Res.*, *92*, 4467, 1987.

Hones, E. W. Jr., The magnetotail: its generation and dissipation, in *Physics of Solar Planetary Environments*, Vol. 2, edited by D. J. Williams, pp.558-571, AGU, Washington, D. C., 1976.

Hones, E. W. Jr., Transient phenomena in the magnetotail and their relation to substorms, *Space Sci. Rev.*, *23*, 393, 1979.

Hones, E. W. Jr., Plasma flow in the magnetotail and its implications for substorm theories, in *Dynamics of the Magnetosphere*, (S.-I. Akasofu, ed.) p. 545, 1980.

Hones, E. W. Jr., Plasma sheet behavior during substorms, in Magnetic Reconnection in Space and Laboratory Plasmas, edited by E. W. Hones, Jr., *Geophys. Monog.*, 30, AGU, 1984.

Huang, C. Y., and L. A. Frank, A statistical study of the central plasma sheet: implications for substorm models, *Geophys. Res. Lett.*, *13*, 652, 1986.

Iijima, T. and T. A. Potemra, Large-scale characteristics of field-aligned currents associated with substorms, *J. Geophys. Res.*, *81*, 3999, 1976.

Iijima, T., T. A. Potemra, L. J. Zanetti, and P. F. Bythrow, Large-scale birkeland currents in the dayside polar region during strongly northward IMF: A new birkeland current system, *J. Geophys. Res.*, *89*, 7441, 1984.

Kamide, Y., and G. Rostoker, The spatial relationship of field-aligned currents and auroral electrojets to the distribution of nightside aurora, *J. Geophys. Res.*, *82*, 5589, 1977.

Kan, J. R., Towards a unified theory of discrete aurora, *Space Sci. Rev.*, *31*, 71, 1982.

Kan, J. R., and W. J. Burke, A theoretical model of polar cap auroral arcs, *J. Geophys. Res.*, *90*, 4171, 1985.

Kan, J. R., and Y. Kamide, Electrodynamics of the westward traveling surge, *J.*

Geophys. Res., 90, 7615, 1985.

Kan, J. R., and W. Sun, Simulation of the westward traveling surge and Pi2 pulsations during substorms, *J. Geophys. Res., 90*, 10,911, 1985.

Kan, J. R., A theory of patchy and intermittent reconnections for magnetospheric flux transfer events, *J. Geophys. Res.*, 93, 5613, 1988.

Kan, J. R., L. Zhu, and S.-I. Akasofu, A theory of substorms: Onset and subsidence, *J. Geophys. Res., 93*, 5624, 1988.

Kan, J. R., Developing a global model of magnetospheric substorms, preprint, 1989.

Kennel, C. F., Consequences of a magnetospheric plasma, *Rev. Geophys., 7*, 379, 1969.

Kisabeth, J. L., and G. Rostoker, Modeling of three dimensional current system associated with magnetospheric substorms, Geophys. J. R. Astron. Soc., 49, 655, 1977.

Knight, S., Parallel electric fields, *Planet. Space Sci., 21*, 741, 1973.

Lanzerotti, L. J., L. C. Lee, C. G. Maclennan, A. Wolfe, and L. V. Medford, Possible evidence of flux transfer events in the polar ionosphere, *Geophys. Res. Lett., 13*, 1089, 1986.

Lee, L. C., Magnetic flux transfer at the Earth's magnetopause, *Solar Wind -Magnetosphere Coupling*, edited by Y. Kamide and J. Slavin, Terra, Tokyo, 1986.

Lui, A. T. Y., E. W. Hones Jr., F. Yasuhara, S.-I. Akasofu, and S. J. Bame, Magnetotail plasma flow during plasma sheet expansions: Vela 5, 6, and Imp-6 observations, *J. Geophys. Res., 82*, 1235, 1977.

Lyons, L. R., D. S. Evans, and R. Lundin, An observed relation between magnetic field-aligned electric fields and downward electron energy fluxes in the vicinity of auroral forms, *J. Geophys. Res., 84*, 457, 1979.

Lyons, L. R., Generations of large-scale regions of auroral currents, electric po-

tentials and precipitation by the divergence of the convection electric field, *J. Geophys. Res.*, *85*, 17, 1980.

Lyons, L. R., and A. Nishida, Description of substorms in the tail incorporating boundary layer and neutral line effects,*Geophys. Res. Lett.*, *15*, 1337, 1988.

Lysak, R. L., and C. T. Dum, Dynamics of magnetosphere-ionosphere coupling including turbulent transport, *J. Geophys. Res.*, *88*, 365, 1983.

Lysak, R. L., Coupling of the dynamic ionosphere to auroral flux tubes, *J. Geophys. Res.*, *91*, 7047, 1986.

Maezawa, K., Magnetic convection induced by the positive and negative z components of the interplanetary magnetic field: Quantitative analysis using polar cap magnetic records, *J. Geophys. Res.*, *81*, 2289, 1976.

Mallinchrodt, A. J., and C. W. Carlson, Relations between transverse electric fields and field-aligned currents, *J. Geophys. Res.*, *83*, 1426, 1978.

Maltsev, Y. P., S. V. Leontyev, and W. B. Lyatsky, Pi-2 pulsations as a result of evolution of an Alfvén impulse originating in the ionosphere during a brightening of aurora, *Planet. Space Sci.*, *22*, 1519, 1974.

Marklund, G. T., L. G. Blomberg, T. A. Potemra, J. S. Murphree, F. J. Rich, and K. Stasiewicz, A new method to derive "instantaneous" high-latitude potential distributions from satellite measurements including auroral imager data, *Geophys. Res. Lett.*, *14*, 439, 1987.

McHenry, M. A. and C. R. Clauer, Modeled ground magnetic signatures of flux transfer events, *J. Geophys. Res.*, *92*, 11,231, 1987.

McIlwain, C. E., Substorm injection boundaries, in Magnetospheric Physics, Ed. B. M. McCormac, p. 143, D. Reidel Publ. Co., Dordrecht-Holland, 1974.

McPherron, R. L., C. T. Russell, and M. P. Aubry, Satellites studies of magnetospheric substorms on August 15, 1968, 9, Phenomenological model for substorms, *J. Geophys. Res.*, *78*, 3131, 1973.

Miura, A., and T. Sato, Numerical simulation of global formation of auroral arcs,

J. Geophys. Res., 85, 73, 1980.

Mizera, P. F., and J. F. Fennell, Signatures of electric fields from high and low altitude particle distributions, *Geophys. Res. Lett., 4*, 311, 1977.

Mozer, F. S., C. A. Cattell, M. K. Hudson, R. L. Lysak, M. Temerin, and R. B. Torbert, Satellite measurements and theories of auroral particle acceleration, *Space Sci. Rev., 27*, 155, 1980.

Nishida, A., and E. W. Hones, Jr., Association of plasma sheet thinning with neutral line formation in the magnetotail, *J. Geophys. Res., 79*, 535, 1974.

Nishida, A., S. J. Bame, D. N. Baker, G. Gloeckler, M. Scholer, E. J. Smith, T. Terasawa, and B. Tsurutani, Assessment of the boundary layer model of the magnetospheric substorm, *J. Geophys. Res., 93*, 5579, 1988.

Opgenoorth, H. J., R. J. Pellinen, W. Baumjohann, E. Nielsen, G. Marklund, and L. Eliasson, Three-dimensional current flow and particle precipitation in a westward traveling surge (observed during the barium-GEOS rocket experiment), *J. Geophys. Res., 88*, 3138, 1983.

Paschmann, G., G. Haerendel, I. Papamastorakis, N. Sckopke, S. J. Bame, J. T. Gosling, and C. T. Russell, Plasma and magnetic field characteristics of magnetic flux transfer events, *J. Geophys. Res., 87*, 2159, 1982.

Rees, M. H., Auroral ionization and excitation by incident energetic electrons, *Planet. Space Sci., 11*, 1209, 1963.

Reiff, P. H., and J. G. Luhmann, Solar wind control of the polar cap voltage, in Solar Wind-Magnetosphere Coupling, edited by Y. Kamide and J. A. Slavin, 453, Terra Scientific Publishing Co., Tokyo, Japan, 1986.

Rijnbeek, R. P., S. W. H. Cowley, D. J. Southwood, and C. T. Russell, Observations of "reverse polarity" flux transfer events at the Earth's dayside magnetopause, *Nature, 300*, 23, 1982.

Robinson, R. M., D. S. Evans, T. A. Potemra, and J. D. Kelly, Radar and satellite measurements of an F-region ionization enhancement in the post-noon sector,

Geophys. Res. Lett., 11, 899, 1984.

Rostoker, G., S.-I. Akasofu, J. Foster, R. A. Greenwald, Y. Kamide, K. Kawasaki, A. T. Y. Lui, R. L. McPherron, and C. T. Russell, Magnetospheric substorms; definition and signatures, *J. Geophys. Res., 85*, 1663, 1980.

Rostoker, G., and T. Eastman, A boundary layer model for magnetospheric substorms, *J. Geophys. Res., 92*, 12,187, 1987.

Rostoker, G., A. Vallance Jones, R. L. Gattinger, C. D. Anger, and J. S. Murphree, The development of the substorm expansive phase: The "eye" of the substorm, *Geophys. Res. Lett., 14*, 399, 1987.

Rothwell, P. L., M. B. Silevitch, and L. P. Block, A model for the propagation of the westward traveling surge, *J. Geophys. Res., 89*, 8941, 1984.

Rothwell, P. L., M. B. Silevitch, L. P. Block, and P. Tanskanen, A model of the westward traveling surge and the generation of Pi 2 pulsations, *J. Geophys. Res., 93*, 8613, 1988.

Russell, C. T., The configuration of the magnetosphere, in *Critical Problems of Magnetospheric Physics*, edited by E. R. Dyer, pp1-16, IUCSTP, National Academy of Sciences, Washington, D. C., 1972.

Russell, C. T., and R. L. Mcpherron, The magnetotail and substorms, *Space Sci. Rev., 15*, 205, 1973.

Russell, C. T., and R. C. Elphic, Initial ISEE magnetometer results: Magnetopause observations, *Space Sci. Rev., 22*, 681, 1978.

Russell, C. T., and R. C. Elphic, ISEE observations of flux transfer events at the dayside magnetopause, *Geophys. Res. Lett., 6*, 33,1979.

Sato, T, T. Shimada, M. Tanaka, T. Hayashi, and K. Watanabe, Formation of field-twisting flux tubes on the magnetopause and solar wind particle entry into the magnetosphere, *Geophys. Res. Lett., 13*, 801, 1986.

Saunders, M. A., C. T. Russell, and N. Sckopke, Flux transfer events: Scale size and interior structure, *Geophys. Res. Lett., 11*, 131, 1984.

Schindler, K., A theory of the substorm mechanism, *J. Geophys. Res.*, *79*, 2803, 1974.

Scholer, M., On the motion of artificial ion clouds in the magnetosphere, *Planet. Space Sci.*, *18*, 977, 1970.

Shepherd, G. G., C. D. Anger, J. S. Murphree, and A. Vallance Jones, Auroral intensifications in the evening sector observed by the Viking ultra violet imager, *Geophys. Res. Lett.*, *14*, 395, 1987.

Siscoe, G. L., Energy coupling between regions 1 and 2 Birkland current systems, *J. Geophys. Res.*, *87*, 5124, 1982.

Smith, R. A., C. K. Goertz, and W. Grossmann, Thermal catastrophe in the plasma sheet boundary layer, *Geophys. Res. Lett.*, *13*, 1380, 1986.

Sonnerup, B. U. O., G. Paschmann, I. Papamastorakis, N. Sckopke, G. Haerendel, S. J. Bame, J. R. Asbridge, J. T. Gosling, and C. T. Russell, Evidence for magnetic field reconnection at the Earth's magnetopause, *J. Geophys. Res.*, *86*, 10,049, 1981.

Southwood, D. J., Theoretical aspects of ionospheric-magnetosphere-solar wind coupling, *Adv. Space Res.*, *5*, 7, 1985.

Southwood, D. J., The ionospheric signature of flux transfer events, *J. Geophys. Res.*, *92*, 3207, 1987.

Spiro, R. W., M. Harel, R. A. Wolf, and P. H. Reiff, Quantitative simulation of a magnetospheric substorm, 3, Plasmaspheric electric fields and evolution of the plasmapause, *J. Geophys. Res.*, *86*, 2261, 1981.

Sugiura, M., A fundamental magnetosphere-ionosphere coupling mode involving field-aligned currents as deduced from DE-2 observations, *Geophys. Res. Lett.*, *1*, 877, 1984.

Temerin, M., K. Cerny, W. Lotko, and F. S. Mozer, Observations of double layer and solitary waves in the auroral plasma, *Phys. Rev. Lett.*, *48*, 1175, 1982.

Vasyliunas, V. M., Mathematical models of magnetospheric convection and its

coupling to the ionosphere, in *Particles and Fields in the Magnetosphere*, ed. by B. McCormac, p. 60, D. Reidel, Dordrecht-Holland, 1970.

Walls, F. L., and G. H. Dunn, Measurement of total cross-section for electron recombination with NO^+ and O_2^- using ion storage technology, *J. Geophys. Res.*, *79*, 1911, 1974.

Watanabe, K., M. Ashour-Abdalla, and T. Sato, A numerical model of magnetosphere-ionosphere coupling: Preliminary results, *J. Geophys. Res.*, *91*, 6973, 1986.

Weimer, D. R., C. K. Goertz, D. A. Gurnett, N. C. Maynard, and J. L. Burch, Auroral zone electric fields from DE 1 and 2 at magnetic conjunctions, *J. Geophys. Res.*, *90*, 7479, 1985.

Weimer, D. R., L. A. Reinleitner, J. R. Kan, L. Zhu, and S.-I. Akasofu, Saturation of the auroral electrojet current and the polar cap potential, *J. Geophys. Res.*, in press, 1990.

Wolf, R. A., M. Harel, R. W. Spiro, G. H. Voigt, P. H. Reiff, and C.-K. Chen, Computer simulation of inner magnetospheric dynamics for the magnetic storm of July 29, 1977, *J. Geophys. Res.*, *87*, 5949, 1982.

Yamamoto, T., and J. R. Kan, The field-aligned scale length of one-dimensional double layers, *J. Geophys. Res.*, *90*, 1553, 1985.

Zhu, L., and J. R. Kan, Effects of ionospheric recombination time scale on the auroral signature of substorms, *J. Geophys. Res.*, in press, 1990.